ENGINEERING EARTH-ABUNDANT COLLOIDAL PLASMONIC AND SEMICONDUCTOR NANOMATERIALS FOR SOLAR ENERGY HARVESTING AND DETECTION APPLICATIONS

by

Yan Cheng

A dissertation submitted to The Johns Hopkins University in conformity with the requirements for the degree of Doctor of Philosophy

Baltimore, Maryland

March, 2020

Abstract

Colloidal nanomaterials have shown intriguing optical and electronic properties, making them important building blocks for a variety of applications, including photocatalysis, photovoltaics, and photodetectors. Their morphology and composition are effective tuning knobs for achieving desirable spectral characteristics for specific applications. In addition, they can be synthesized using solution-processed methods which possess the advantages of low cost, facile fabrication, and compatibility with building flexible devices. There is an ongoing quest for better colloidal materials with superior properties and high natural abundance for commercial viability. This thesis focuses on three such materials classes and applications: 1) studying the photophysical properties of earth-abundant plasmonic alumionum nanoparticles, 2) tailoring the optical profiles of semiconductor quantum dot solar cells with near-infrared sensitivity, and 3) using one-dimensional nanostructures for photodetector applications. A variety of analytical techniques and simulations are employed for characterization of both the morphology and optical properties of the nanostructures and for evaluating the performance of nanomaterial-based optoelectronic devices.

The first experimental section of this thesis consists of a systematic study of electron relaxation dynamics in solution-processed large aluminum nanocrystals.

Transient absorption measurement are used to obtain the important characteristic relaxation timescales for each thermalization process. We show that several of the relevant timescales in aluminum differ from those in analogous noble metal nanoparticles and proposed that surface modification could be a useful tool for tuning heat transfer rates between the nanostructures and solvent. Further systematic studies on the relaxation dynamics in aluminum nanoparticles with tunable sizes show size-dependent phonon vibrational and damping characteristics that are influenced by size polydispersity, surface oxidation, and the presence of organic capping layers on the particles. These studies are significant first steps in demonstrating the feasibility of using aluminum nanomaterials for efficient photocatalysis.

The next section summarizes studies on the design and fabrication of multicolored PbS-based quantum dot solar cells. Specifically, thin film interference effects and multi-objective optimization methods are used to generate cell designs with controlled reflection and transmission spectra resulting in programmable device colors or visible transparency. Detailed investigations into the trade-off between the attainable color or transparency and photocurrent are discussed. The results of this study could be used to enable solar cell window-coatings and other controlled-color optoelectronic devices.

The last experimental section of thesis describes work on using 1D antimony selenide nanowires for flexible photodetector applications. A one-pot solution-based synthetic method is developed for producing a molecular ink which allows fabrication of devices on flexible substrates. Thorough characterization of the nanowire composition and morphology are performed. Flexible, broadband antimony selenide nanowire photodetectors are fabricated and show fast response and good mechanical stability. With further tuning of the nanowire size, spectral selectivity should be achievable. The excellent performance of the nanowire photodetectors is promising for the broad implementation of semiconductor inks in flexible photodetectors and photoelectronic switches.

Primary Reader and Advisor: Susanna M. Thon

Secondary Reader: Amy C. Foster

Thesis Committee

Primary Readers

Susanna M. Thon (Primary Advisor)
Assistant Professor
Department of Electrical and Computer Engineering
Johns Hopkins Whiting School of Engineering

Jin U. Kang
Professor
Department of Electrical and Computer Engineering
Johns Hopkins Whiting School of Engineering

Amy C. Foster
Associate Professor
Department of Electrical and Computer Engineering
Johns Hopkins Whiting School of Engineering

Acknowledgements

First and foremost, I would like to express my sincere gratitude for my advisor, Professor Susanna Thon, who offered me the opportunity to join the nanoenergy lab. She is a great mentor and always supportive of my PhD research with continuous guidance, patience, and encouragement. I am very grateful for all the insightful discussions and suggestions she has provided on my research, and I am also inspired by her enthusiasm and passionate attitude.

I would also like to thank our collaborator, Professor Art Bragg, who is being so resourceful and offered stimulating advice on our project. Thank you to professor Jacob Khurgin who taught me all the excellent courses and used his humor to make it an interesting learning process. Also thank you for both professor Amy Foster and Jin Kang for the valuable suggestions on my thesis and being part of my committee and thesis readers.

The group members here have always given me good advice and collaborations. I am grateful for Ebuka Arinze and Botong Qiu who are early members of the group and have taken a lot of lab responsibilities, Yida Lin who is a very knowledgeable person for all the useful discussions, Lulin Li who is being so friendly and has always been enthusiastic and helpful in research, and Arlene Chiu for all the support and encouragement. I would also like to thank my other past and present labmates that include Sreyas Chintapalli, Chengchangfeng Lu, Eric Rong, Mansi Gao, Tina Gao, Nicole Kim, Nathan Palmquist, and Garrett Ung for making my experience exciting. I would also like to acknowledge Ken Smith, who has been really responsive and helpful through our collaboration.

I would like to thank my friends at JHU, Xingang Zhao, Luoluo Liu, Tengfei Li, Hongfu Ting, Ruidong Xue, Kangmei Li, Xinting Yu, Xu Yang, Chi Yan and Jessica Ma, who have given me so much support through this wonderful time. I am also grateful for my friends in China, particularly Youzheng Qi, Zhiguo Yu and Wei Lin, who are so helpful in many ways.

Nobody has been more important to me in this journey than the members of my family. I am deeply thankful to my parents for their constant love, support, sacrifice, and devotion, who always believing in me and giving me courage.

Table of Contents

List of Tables

List of Figures

Chapter 1

Introduction and Motivation

Global demand for energy, driven by the electricity, manufacturing, and transportation sectors, is accelerating at increasingly to grow with a fast pace, and meeting this demand is one of the primary challenges of in the 21st century. Figure 1.1. [1] shows the energy consumption from of different sources over a 15 year period, and it is clear that with fossil fuels remaining to be the dominant part source. What's worse, this is a problem because fossil fuels usage leads to carbon dioxide (CO_2) emissions which comprises 74% of the gases that is causing a global greenhouse effect. CO_2 emission from coal, oil, and natural gas is still continuing to grow and remains high (Figure. 1.2) [2]. In the meantime, toxic contaminants are produced and discharged into the environment during manufacturing fossil fuel burning. As a result, we are facing the dual issues of global climate change and degradation of environmental pollution in our air and water streams due to contaminants is challenging [3]. Therefore, it is extremely important to develop new and sustainable energy sources, as well as solving serious environmental issues.

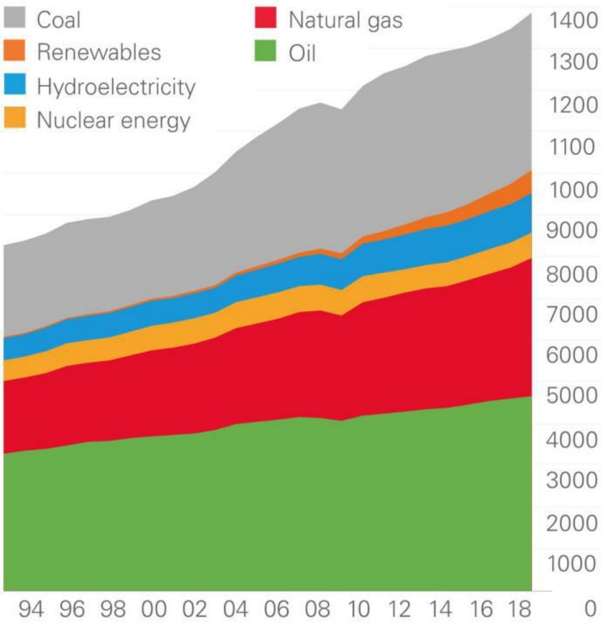

Figure 1.1 World consumption of primary energy sources, 1993-2018 [1].

Among the many renewable energy sources, solar energy is considered to be a promising alternative means to deal with the energy crisis and avoid CO_2 emission, leading to a sustainable future [4]. It is practically unlimited and the most abundant of the renewable sources; the power flux which reaches earth from the sun is thousands of times of the current world power consumption. Furthermore, it is also among the cleanest sources; solar technology does not produce any hazardous emissions. Solar power can be produced in the form of both electric (solar cells, known as photovoltaics) and thermal (solar thermal) energy. To date, the worldwide installed capacity of solar harvesting devices is 505 GW and is still rapidly increasing annually [5].

However, there are still many issues with commercial photovoltaics that needs to be addressed before it can fully replace conventional sources of energy. One major hurdle currently is the low photovoltaic conversion efficiency of commercial solar modules which is only around 20%. Generally, cells with higher efficiencies also have higher manufacturing costs [6,7]. Therefore, new materials and new engineering strategies are the main topics for improving the conversion efficiency and reducing the fabrication costs of solar cells [8].

Semiconductor colloidal quantum dots are a type of novel nanomaterial with tunable bandgaps and absorption profiles that can be tailored to match the solar spectrum with advanced synthesis techniques. These materials are solution-processed and, in addition to their optical properties, are also attractive for producing lightweight and flexible devices [9,10].

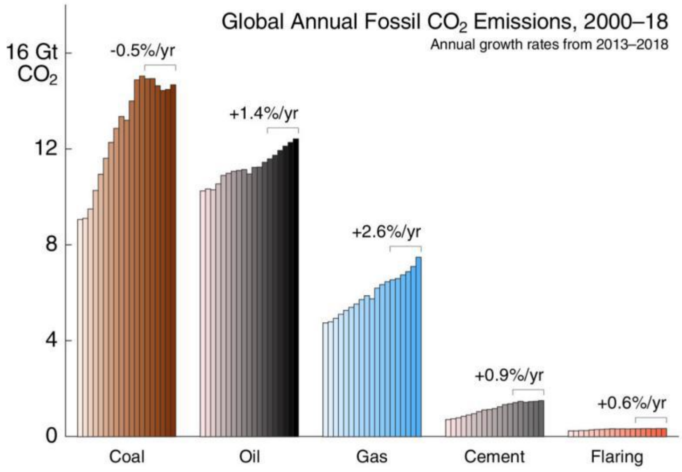

Figure 1.2 Annual CO_2 emission from different fossil fuel sources, 2000-2018 [2].

For the past few decades, the technology of photocatalysis has drawn a great deal of attention and been extensively studied due to its advantages of utilizing solar radiation as a clean energy input and catalyzing reduction-oxidation reactions without producing chemical waste [11]. Therefore, it is a promising route for resolving the environmental pollution issues, and can be used for applications such as water splitting for hydrogen production, air and water purification, and self-cleaning surfaces [12,13]. A variety of semiconductors have been explored for their potential as photocatalysts, but most exhibit low conversion efficiency. One of the limiting factor in the best photocatalysts such as TiO_2 is low absorption in the visible wavelengths range which limits the use of sunlight as a photocatalytic light source [14].

It is therefore crucially important to develop efficient light management strategies in photocatalytic materials. One route involves finding or engineering superior materials to overcome the low conversion efficiencies while maintaining low costs. Surface plasmonics is an emerging field with broad applicability for enhancing light-matter interactions [15]. By including metal nanostructures in various optoelectronic devices, better performance can be achieved with optimized design of the specific architectures and optical properties of the structures involved. In particular, plasmonic metal nanostructures can be used for improving catalytic activity by generating hot charge carriers that can be transferred to a catalyst or directly used in redox reactions.

Even with the tremendous potential of new nanomaterials for solar energy harvesting, significant investigations are still needed to further fundamental understanding and improve robustness of the materials and devices. Specifically, extensive exploration is needed to identify plasmonic materials with excellent absorption but also high natural abundance for cost-effectiveness. In addition, studies of the photophysical properties of plasmonically-enhanced photocatalysts can serve as guidance for designing effective architectures of plasmonic-semiconductor systems.

In this thesis, systematic studies on the plasmonic properties of earth-abundant metal nanomaterials in the solution phase will be discussed. This work is important for practical applications and should pave the way for the development of plasmonically-enhanced photocatalytic systems. In addition, multi-colored and semi-transparent PbS-based solar cells have been studied and fabricated using multilayer interference effect and particle swarm optimization. New method of synthesis of Sb_2Se_3 inks in the solution phase is discussed and its application in broadband flexible photodetectors have been demonstrated.

References

[1] BP Statistical Review of World Energy, 2019, 68th edition, https://www.bp.com/content/dam/bp/business-sites/en/global/corporate/pdfs/energy-economics/statistical-review/bp-stats-review-2019-full-report.pdf

[2] Jackson, R. B., P. Friedlingstein, R. M. Andrew, J. G. Canadell, C. Le Quéré, and G. P. Peters. "Persistent fossil fuel growth threatens the Paris Agreement and planetary health." Environmental Research Letters 14, no. 12 (2019): 121001.

[3] Lipczynska-Kochany, Ewa. "Effect of climate change on humic substances and associated impacts on the quality of surface water and groundwater: a review." Science of the Total Environment 640 (2018): 1548-1565.

[4] Poudyal, Ramhari, Pavel Loskot, Rabindra Nepal, Ranjan Parajuli, and Shree Krishna Khadka. "Mitigating the current energy crisis in Nepal with renewable energy sources." Renewable and Sustainable Energy Reviews 116 (2019): 109388.

[5] Renewables 2019 Global Status Report, REN21Community, https://www.ren21.net/wp-content/uploads/2019/05/gsr_2019_full_report_en.pdf

[6] Green, Martin A. "Commercial progress and challenges for photovoltaics." Nature Energy 1, no. 1 (2016): 1-4.

[7] Lee, Taesoo D., and Abasifreke U. Ebong. "A review of thin film solar cell technologies and challenges." Renewable and Sustainable Energy Reviews 70 (2017): 1286-1297.

[8] Sun, Chenkai, Fei Pan, Haijun Bin, Jianqi Zhang, Lingwei Xue, Beibei Qiu, Zhixiang Wei, Zhi-Guo Zhang, and Yongfang Li. "A low cost and high performance

polymer donor material for polymer solar cells." Nature communications 9, no. 1 (2018): 1-10.

[9] Yuan, Mingjian, Mengxia Liu, and Edward H. Sargent. "Colloidal quantum dot solids for solution-processed solar cells." Nature Energy 1, no. 3 (2016): 1-9.

[10] Carey, Graham H., Ahmed L. Abdelhady, Zhijun Ning, Susanna M. Thon, Osman M. Bakr, and Edward H. Sargent. "Colloidal quantum dot solar cells." Chemical reviews 115, no. 23 (2015): 12732-12763.

[11] Martin, David James. Investigation into high efficiency visible light photocatalysts for water reduction and oxidation. Springer, 2015.

[12] Kamegawa, Takashi, Koichi Irikawa, and Hiromi Yamashita. "Multifunctional surface designed by nanocomposite coating of polytetrafluoroethylene and TiO_2 photocatalyst: Self-cleaning and superhydrophobicity." Scientific reports 7, no. 1 (2017): 1-8.

[13] Hisatomi, Takashi, and Kazunari Domen. "Reaction systems for solar hydrogen production via water splitting with particulate semiconductor photocatalysts." Nature Catalysis 2, no. 5 (2019): 387-399.

[14] Yang, Yucheng, Ting Zhang, Ling Le, Xuefeng Ruan, Pengfei Fang, Chunxu Pan, Rui Xiong, Jing Shi, and Jianhong Wei. "Quick and facile preparation of visible light-driven TiO_2 photocatalyst with high absorption and photocatalytic activity." Scientific reports 4 (2014): 7045.

[15] Yu, Huakang, Yusi Peng, Yong Yang, and Zhi-Yuan Li. "Plasmon-enhanced light–matter interactions and applications." npj Computational Materials 5, no. 1 (2019): 1-14.

Chapter 2

Optical Nanomaterials Engineering: Properties and Synthetic Routes

For the past few decades, researchers have put tremendous effort into investigating light-matter interactions at the nanoscale. Metal nanostructures have shown superior optical properties of large scattering and absorption cross sections, strong near-field enhancement, and confining light to small volumes [1-3]. These studies are realized by the development of synthesis and fabrication technology which provides the possibility to obtain nanomaterials of controlled dimensions, sophisticated shapes and compositions [4-6]. By utilizing their unique properties, plasmonic nanomaterials have been widely investigated in a large number of diverse applications including photovoltaics, photocatalysis, photothermal therapy, and structural coloring [7-10].

Colloidal quantum dots, semiconductor nanocrystals functionalized by surfactants, are a related material. With sizes in the range of a few nanometers, they exhibit the quantum confinement effect which endows them with tunable bandgaps, and therefore tailored optoelectronic characteristics [11-14]. They can be synthesized using solution-processed methods and processed into thin films. The film phase is prepared by low temperature techniques which are much quicker and easier than the vacuum deposition methods commonly used for conventional thin film growth.

The physical mechanisms and synthetic strategies of these two important types of nanomaterials will be discussed in detail in this chapter.

2.1 Plasmonic Metal Nanoparticles

2.1.1 Mechanism of Localized Surface Plasmon Resonance

Over 150 years ago, Michael Faraday first synthesized gold colloids which displayed a ruby color when light was directed through the liquid [15], though the particles were too small to be individually observed at that time. Since then, this effect has been systematically investigated and attributed to a localized surface plasmon resonance (LSPR) of the gold particles, which is induced by the collective oscillation of electrons in the conduction band of metal nanoparticles (NPs) in response to incident electromagnetic radiation. Figure 2.1 shows a diagram of surface charge oscillations in a single metal NP with dimensions smaller than the light wavelength. This leads to important characteristics including strong scattering and absorption, and near-field enhancement in metal NPs, making them part of a potential strategy for overcoming the diffraction limit in imaging systems [16,17].

Due to these attractive features, metal NPs have been extensively investigated in a variety of applications. For example, they can be incorporated into solar cells and photovoltaics as light scatterers and sensitizers [18,19]. They are also widely used in a sensing technique where a wavelength shift of the LSPR peak position is caused by a dielectric constant change in the surrounding environment [20,21]. When used in Raman scattering, the signal is greatly enhanced by the presence of plasmonic NPs due to their near field properties [22].

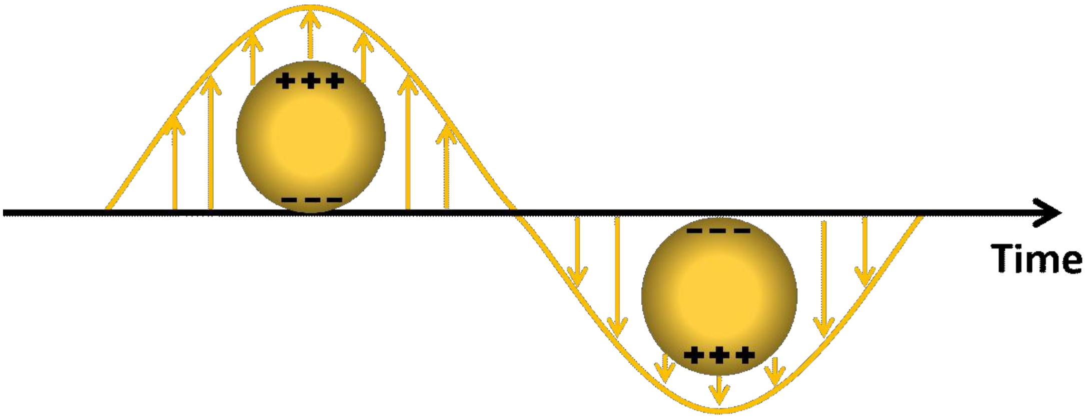

Figure. 2.1 Schematic diagram of the LSPR in a spherical metal nanoparticle.

Using electrostatic theory and by solving Laplace's equation, the polarizability of a spherical NP can be expressed as given in Equation 2.1. [23], where ε and ε_m are the dielectric function of the metal NP and medium, respectively.

$$\alpha = 4\pi a^3 \frac{\varepsilon - \varepsilon_m}{\varepsilon + 2\varepsilon_m} \tag{2.1}$$

From this equation, it is apparent that the resonant condition (the Fröhlich condition) is met when the real part of the metal's dielectric constant equals $2\varepsilon_m$. Therefore, the LSPR frequency is calculated as in Equation 2.2 [23], using the Drude model for the metal's dielectric function. Here ω_p is the metal's bulk plasma frequency.

$$\omega = \omega_p / \sqrt{3} \tag{2.2}$$

As NP diameter approaches 100 nm, Mie theory is used to describe the scattering and absorption of large homogeneous spherical particles [24,25,26]. Scattering (C_{sca}), absorption (C_{abs}), and extinction (C_{ext}) cross sections are obtained according to Equations 2.3-2.5. In these equations, l is the scattering mode order, a_l and b_l are from Bessel function coefficients, and k is the wave vector.

$$C_{sca} = \frac{2\pi}{k^2}\sum_{l=1}^{\infty}(2l+1)\left(|a_l|^2 + |b_l|^2\right) \tag{2.3}$$

$$C_{ext} = \frac{2\pi}{k^2}\sum_{l=1}^{\infty}(2l+1)\,\mathrm{Re}(a_n^2 + b_n) \tag{2.4}$$

$$C_{abs} = C_{ext} - C_{sca} \tag{2.5}$$

For more rigorous calculations for nanostructures of arbitrary shape and size, the finite-difference time-domain (FDTD) technique for solving Maxwell's equations has been extensively used to simulate nanoparticle optical response [27,28].

The frequency of the resonance is not only sensitive to the plasmonic material type, but is also dependent on the morphology and composition of the specific NP. Polarization changes with variations in all of the above parameters. Figure 2.2 (a)-(d) show the results for LSPRs with wide tunability in wavelength as the size, shape, composition, and dielectric constant of the medium are varied by tuning synthetic parameters [29-31].

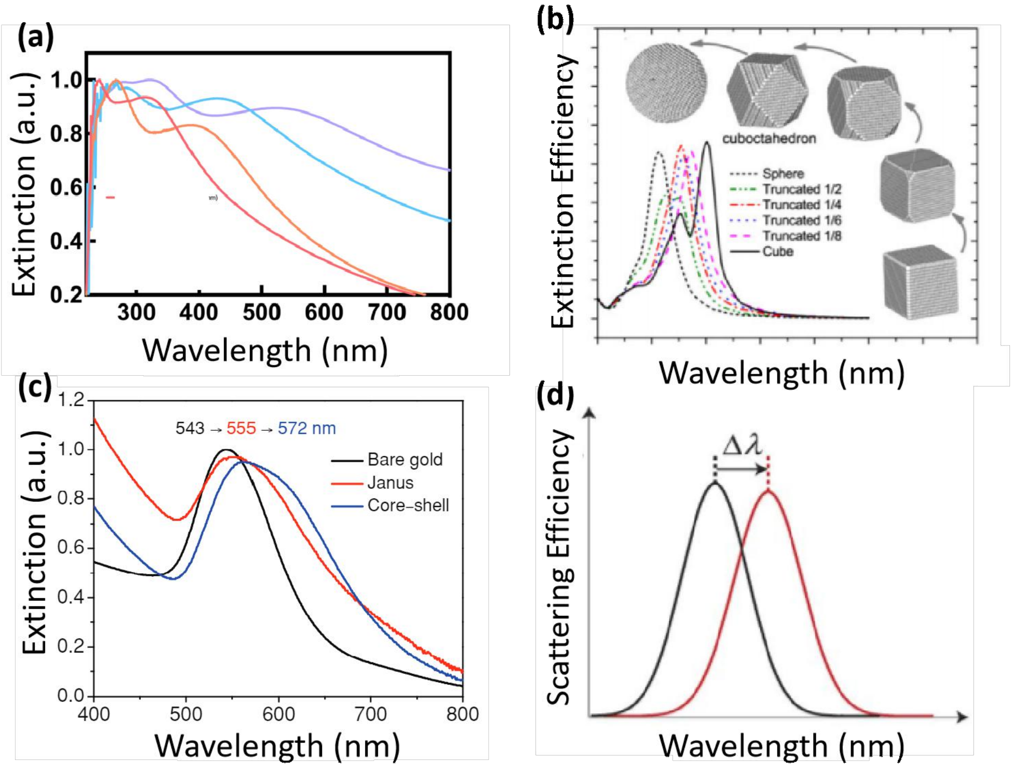

Figure 2.2 (a) UV-Vis-NIR extinction spectra for Al NPs with icosahedral shapes synthesized in our lab with tunable diameters from 65-130 nm. (b) Calculated extinction spectra for Ag NPs with shapes evolving from spheres to cubes [29]. (c) Measured LSPR spectra for multicomponent structures of both Janus and core-shell Au-TiO_2 NPs compared to bare Au NPs [30]. (d) Illustration of the effect of changing the dielectric constant of the surrounding environment of a plasmonic NP due to hydrogen adsorption [31].

To date, precious metals have been the most intensively studied materials for surface plamsonics, with plasmon resonances mainly in the visible and near infrared wavelength range. Gold (Au) is more stable while silver (Ag) exhibits stronger plasmonic peak intensities with lower resistive losses [32,33]. There is increasing demand for new alternative plasmonic materials that are more economical and have good plasmonic properties [34-36]. From a sustainability perspective, aluminum is drawing increasing interest due to several advantages. Aluminum (Al) is the most abundant metallic element in the earth’s crust. Compared to Au and Ag, it has much lower cost and low toxicity [37,38]. As is shown in Figure 2.3 [37], it exhibits a wider tuning range for plasmon resonances, which are based in the ultraviolet (UV) region, but can be shifted to the visible using different tuning mechanisms. Due to the above reasons, Al has been gaining traction as a plasmonic material, and it has been applied in applications such as surface-enhanced Raman spectroscopy, displays, and plasmonic photocatalysis [39,40].

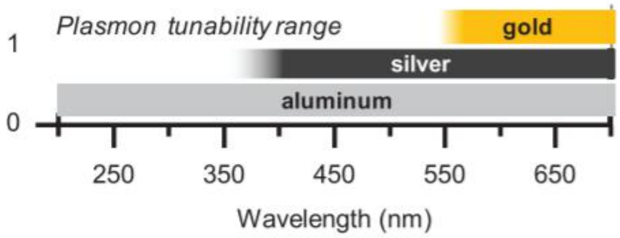

Figure 2.3 Comparison of the LSPR wavelength tuning range of Au, Ag, and Al [37].

2.1.2 Synthetic Methods

There are various synthetic methods to grow metal NPs with versatile morphology. One approach is one-pot synthesis during which a metal precursor is first reduced into metal nuclei and seeds followed by nucleation and growth on the seeds [41]. Seed-mediated growth is another method that is beneficial for generating desirable particle shapes by providing seeds with crystallinity and population control for subsequent metal growth [42]. Electrochemical synthesis is an option that works by reducing a metal salt precusor at a cathode in a nonaqueous environment [43].

To tailor the spectral properties of the LSPR, it is important to achieve size-tuning and size dispersity control during synthesis. This requires fine-tuning of reaction parameters, including concentration of precursors, reaction time and temperature. Choosing suitable ligands can facilitate control over the size and shape and help maintain colloidal stability of the NPs in the solution phase. Citrate is commonly used to stabilize Au and Ag NPs, but often results in particles with broad size distribution and poor stability [44]. Poly(vinylpyrrolidone) is used as a capping agent in polyol reduction synthesis which is a favorable method for producing controlled morphology and desirable plasmonic properties by adjusting the amount of ligands and reaction temperature [45].

Unlike precious metals, Al NPs are synthesized using decomposition of a precursor with the aid of a transition metal catalyst such as titanium isoproproxide [46]. Figure 2.4 shows an Al NP solution during different NP growth stages.

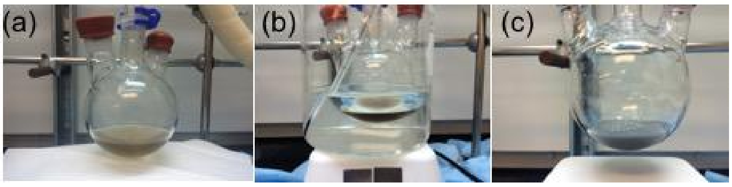

Figure 2.4 Al NP synthesis: the solution color changes from light brown to black and finally to grey during different growth stages.

The stability of the Ti−Al−H clusters in the solvent determines the number of seeds produced. Varying the solvent type used for the reaction can be used to control the NP. Oleic acid and cumyldithiobenzoate-terminated polystyrene have been used to maintain the stability of Al NPs in 2-propanol and water [46,47]. Fig. 2.5 shows transmission electron microscopy (TEM) images of Al NPs with icosahedral shapes and tunable diameters from 65 nm to 130 nm by varying the addition time of oleic acid capping ligands.

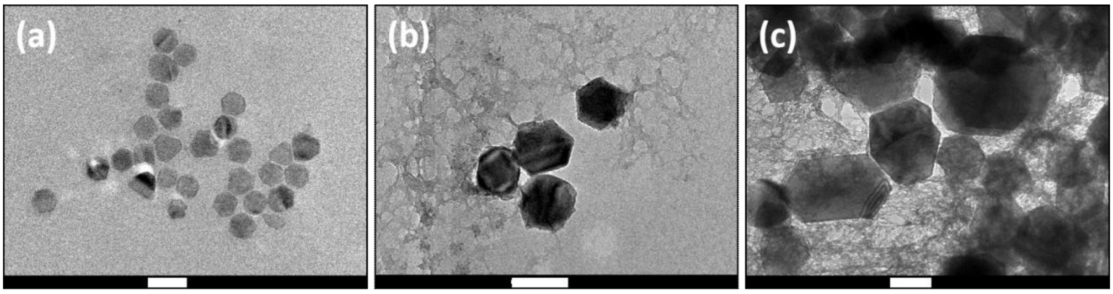

Figure 2.5 TEM images of Al NPs with mean diameters of approximately (a) 65 nm, (b) 100 nm, and (c)130 nm. Scale bar is 100 nm.

For noble metal NPs, the shapes are determined by the initial seeds of single-crystal, singly twinned, or multiply twinned structures which further grow into different shapes. Figure 2.6 demonstrates the single crystal seed evolution into polyhedra, cubes, or bars, and single- and multi-twinned seed growth into beams, rods, and icosahedra [48]. Plates with stacking faults can be used to produce hexagonal or triangular plates. In addition, ligands are employed to change the surface free energy via selectively binding to particular facets and playing a dominant role in the final shapes. Examples of capping agents that are frequently used are cetyltrimethylammonium bromide, polyvinylpyrrolidone, and sodium citrate [49-51].

Shape control for anisotropic Al nanocrystal growth is limited due to the reaction of the ligands with the Al precursor. One study synthesized a mixture of Al nanorods and NPs by thermal decomposition of triisobutyl aluminum which exhibits different decomposition rates with respect to different facets [52]. Al nanocubes with {100} facets were synthesized by using Tebby's catalyst ($C_{13}H_{18}AlClTi$) [53]. In this reaction, Al-C bonds lead to unknown species which preferentially bind to {100} planes.

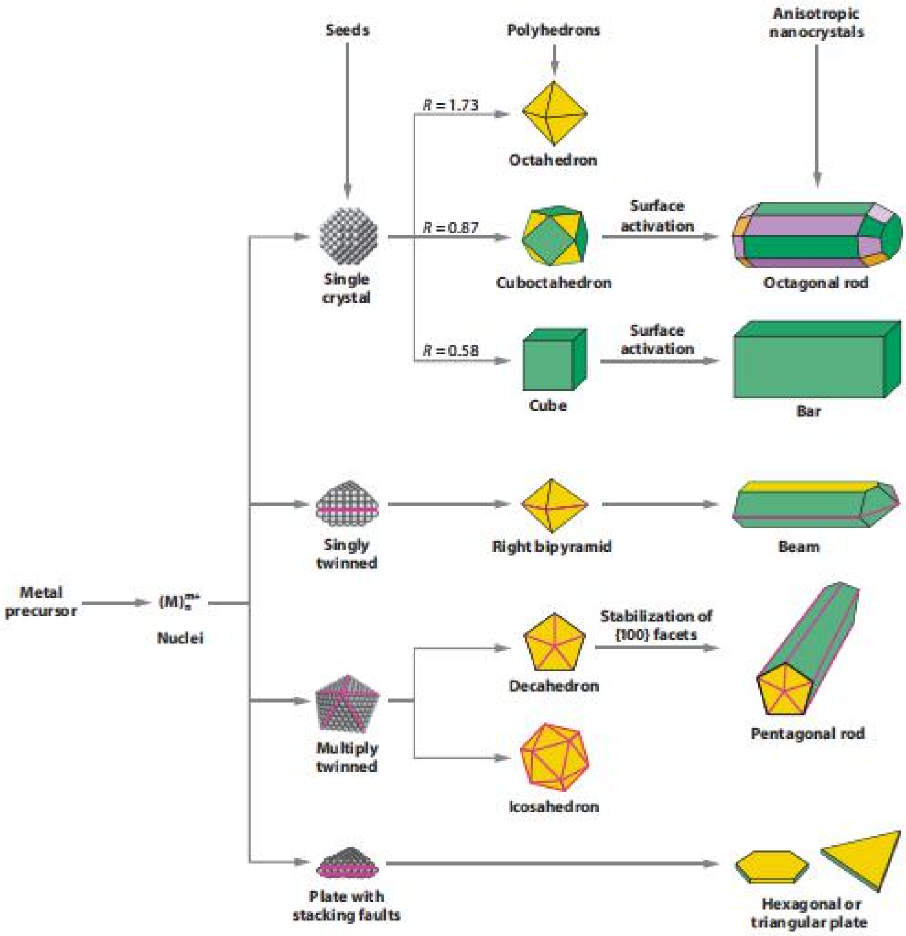

Figure 2.6 Schematic diagram illustrates the reactions that lead to different nucleation conditions and different final shapes for noble metal NPs [48].

Compositional control is based on synthesizing a seed material and epitaxially growing materials with other compositions onto the seed crystal in a heterogeneous nucleation growth process. Core-shell and Janus structures can be synthesized depending on similarities in the crystal structure and the lattice matching of the seed and overcoating materials [54,55]. Galvanic replacement and ion exchange reactions use differences in the reduction potentials for different materials or direct replacement of the original atoms, and are particularly effective in producing porous and more complex structures [56,57]. Biomolecules can act as linkers to achieve self-assembled multicomponent nanostructures [58].

2.1.3 Energy Relaxation and Transient Absorption Measurements

Plasmon excitations decay through different pathways which determine their resonance broadening. Radiation damping is the process of dipole energy loss through coherent scattering and is the main damping route for particles with large dimensions. Plasmons can also decay via nonradiative damping, known as Landau damping, during which process electron and hole pairs are generated. Hot carriers will then undergo subsequent thermal relaxation processes with characteristic timescales, including electron-electron scattering (~100's of fs), electron-phonon scattering (~100's of fs to 1 ps), and phonon-phonon scattering (~100's of ps to ns) [59,60]. Acoustic phonon vibrations are also present on the hundreds-of-picoseconds timescale. Figure 2.7 [60] shows the Fermi distribution at different stages of the relaxation process, which changes from a nonthermal to a thermal distribution, with the system ultimately reaching thermal equilibrium with the surrounding environment.

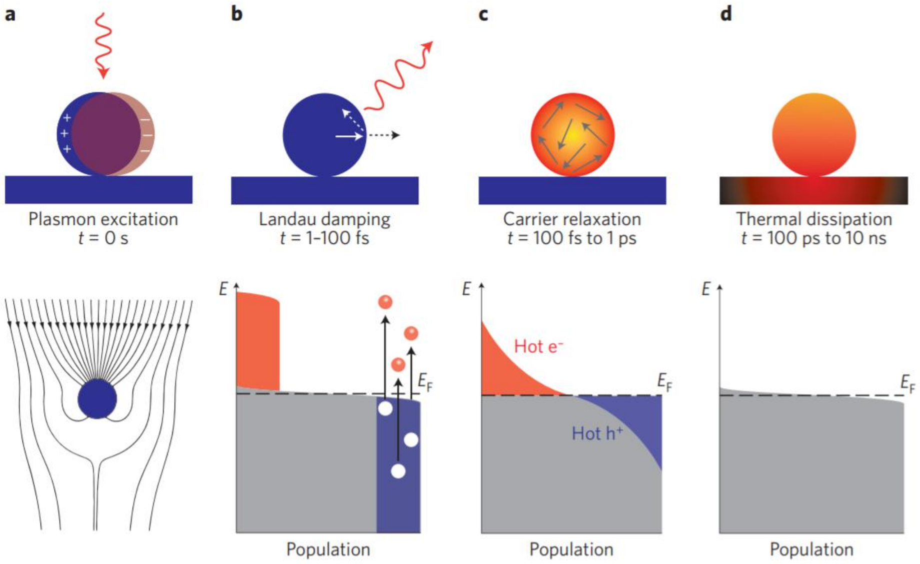

Figure 2.7 Illustration of energy relaxation processes and the population of excited charge carriers in a metal NP after laser excitation [60].

Ultrafast femtosecond transient absorption spectroscopy (TAS), also called pump-probe spectroscopy, is a useful tool that is frequently used to study the electron relaxation dynamics in metal NPs. In a typical measurement, a laser pulse is first generated to pump the electrons to the excited states in the sample, and another laser pulse is then used to probe the relaxation of electrons with femto-to-picosecond timescales at different time delays [61]. Figure 2.8 [62] contains a schematic diagram of the basic setup in a transient measurement. Time-dependent changes of the transmission or absorption are obtained which probe changes in the dielectric function of the materials as a result of optical excitation. In metal NPs, the nonlinear optical response is affected by both intra- and interband transitions that are determined by their unique band structures.

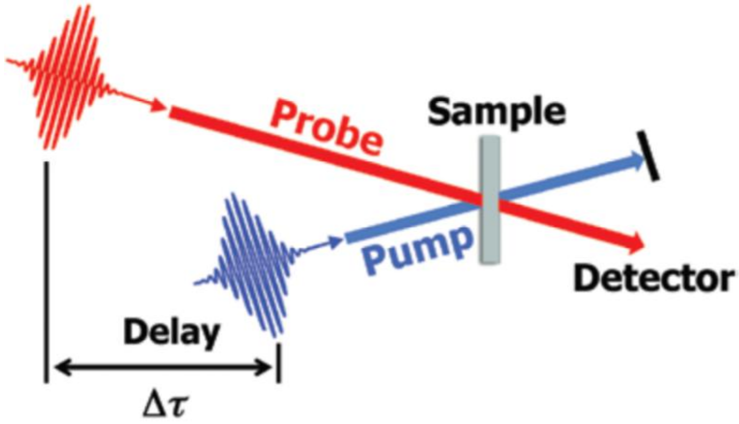

Figure 2.8 Schematic diagram showing the TAS measurement setup, in which a pump pulse excites the carriers and a probe pulse is used to observe changes in the sample as a function of delay time between the pump and probe [62].

2.2 Colloidal Semiconductor Quantum Dots

This section is adapted (in part) from Reference [63]. Reprinted with permission from Nanophotonics, Volume 5, Issue 1, Pages 31-54, "Advancing colloidal quantum dot photovoltaic technology," by Y. Cheng, E. S. Arinze, N. Palmquist and S. M. Thon, copyright © 2016.

2.2.1 Tunable Bandgaps and Spectral Sensitivity

Colloidal quantum dots (CQDs) are semiconductor nanoparticles which are functionalized with surfactants and stabilized in solution. Their dimension generally range from a few nanometers to 20 nm. One important physical property, and also the motivation for developing CQDs for optoelectronic applications such as photovoltaics and photodetectors, is due to the quantum confinement effect [64]. The strength of this effect in a CQD can be determined by comparing the actual size of the CQD and its exciton Bohr radius which is defined in Equation 2.6. a_0, ε, and m^* are the hydrogen atom Bohr radius, semiconductor dielectric constant and carrier effective mass, respectively.

$$a_B = \varepsilon \frac{m_0}{m^*} a_0 \tag{2.6}$$

Compared to their bulk counterparts, the size of the CQD has a direct impact on its bandgap, with smaller quantum dots exhibiting higher excitation energies. Therefore, the optoelectronic properties of CQDs can be easily tuned through controlling their size, shape, and composition. Figure. 2.9 shows absorption spectra tuned through size dependence effects for PbS CQDs.

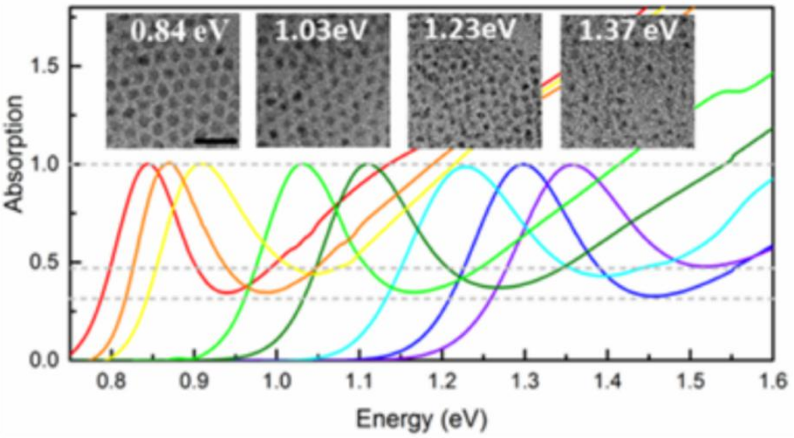

Figure 2.9 Optical absorption spectra of PbS CQD solutions with tunable wavelength response for varying particle size [65].

The bandgap tunability in quantum dots is quantitatively described by the Brus equation (Equation 2.7) [66]. Here, E^* is the apparent band gap, E_g is the bulk band gap, m_e and m_h are the effective electron and hole masses, respectively, ε_p is the dielectric constant of the nanoparticle and R is the nanoparticle radius.

$$E^* = E_g + \frac{h^2\pi}{2R^2}\left[\frac{1}{m_e} + \frac{1}{m_h}\right] - \frac{1.8e^2}{\varepsilon_o \varepsilon_p R} \tag{2.7}$$

This formula includes the additive component of quantum confinement of the exciton as well as the subtractive component of the electron-hole repulsion. In terms of elemental composition, CQDs can be made from group IV, group II-VI, IV-VI, III-V binary, and perovskite semiconductors with emission peaks spanning the visible to the mid-infrared spectral wavelengths (Figure 2.10) [67].

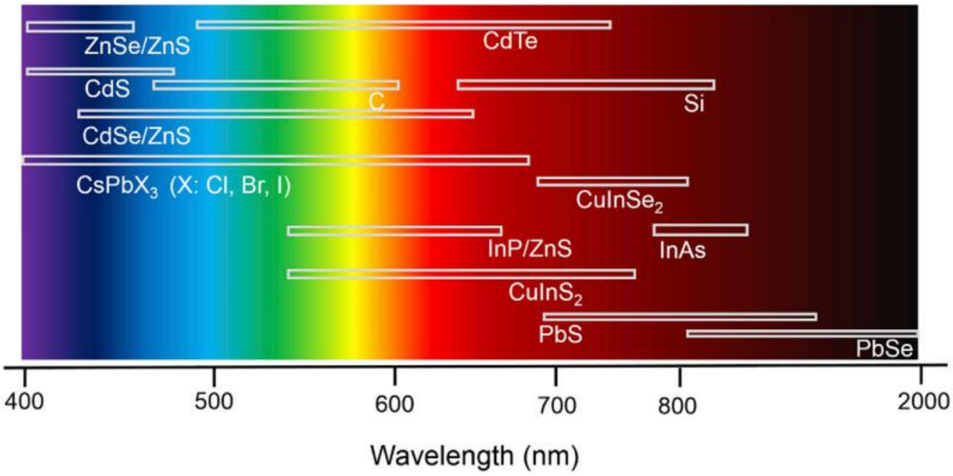

Figure 2.10 Emission wavelength range for semiconductor CQDs of different materials in the solution phase [67].

For PbS CQDs, a prevalent material for solar cells due to the optimal band gap tuning range, Moreels et al. showed that the following empirical equation is a good approximation of the relationship between the effective band gap, E^* (in eV) of the CQD and its diameter, d (in nm) [68]:

$$E^* = 0.41 + \left(0.0252d^2 + 0.283d\right)^{-1} \tag{2.8}$$

The ambient stability of PbS CQDs has also been demonstrated to be dependent on the nanoparticle size. The excitonic wavelength of larger CQDs (diameter >4 nm) experiences a blue shift when stored in air, as the un-passivated (100) surface becomes oxidized and the effective optical particle diameter decreases. It was also shown that the molar extinction coefficient increases with the CQD volume as d^3 (where d is particle diameter) at higher energies, but only increases as $d^{1.3}$ near the band gap [68].

Electroluminescence efficiency is viewed as a good indirect measure of the open-circuit voltage of a solar cell; thus, achieving large luminescence yields is a requirement in photovoltaic materials. At open-circuit, high luminescence efficiency implies the absence of nonradiative sources of recombination in a solar cell [69]. Typical as-synthesized CQD solutions possess photoluminescence quantum efficiencies (PLQE) around 50%, and treatments such as a cadmium chloride ($CdCl_2$) metal-halide passivation strategy have been shown to help CQD solutions maintain these efficiencies even after the washing steps necessary to prepare the CQDs for film deposition [70]. Film phase PLQEs are much lower, substantiating the view that CQD film transport is limited by nonradiative recombination processes induced by the large electronic trap state densities.

Additionally, emission in CQDs is red-shifted with respect to the first (1S) excitonic absorption peak [71]. This difference between the luminescence energy and the absorption energy is referred to as the Stokes shift, and it decreases with increasing quantum dot size. The relatively large Stokes shifts observed in CQDs have been partially attributed to the surface properties of the nanoparticles.

2.2.2 Quantum Dot Synthesis Strategies

The most common types of CQD materials used in solar cell applications are lead sulfide (PbS), lead selenide (PbSe), cadmium sulfide (CdS) and cadmium selenide (CdSe). PbS and PbSe possess small bulk band gaps, 0.41 and 0.27 eV, respectively, making them ideal candidates for tuning the absorption spectra throughout the near-IR portion of the sun’s spectrum [72,73]. CdS and CdSe, with larger bulk band gaps of 2.42 and 1.74 eV, respectively, have found use in sensitized solar cell (SSC) architectures, and are of more interest for visible-wavelength applications. They have good absorption in the visible and UV spectrum, larger obtainable open-circuit voltage (V_{OC}) limits and have band edges well suited for coupling with many organic polymers.

A critical factor for most CQD device applications is the synthesis of highly monodisperse quantum dots. CQD size is controlled during synthesis by a number of factors, including temperature, precursor concentration and rate of conversion and degree of saturation. The synthesis of CQDs typically involves precursor decomposition forming monomers that undergo rapid nucleation followed by a slow growth phase [74,75]. The synthesis reaction is initiated at a particular temperature, when the room temperature precursor is injected into a hot noncoordinating solvent (called the hot injection method). The nucleation and growth processes are influenced by a number of factors including monomer concentration and reactivity, solution viscosity and reaction temperature.

By varying the injection temperature, the size of the quantum dots can be tuned over a relatively large range. Figure 2.11 (A) shows absorption spectra for several PbS CQD solutions synthesized via the hot injection method with excitonic peaks in the range of 880 – 1600 nm, corresponding to CQD diameters of ~3-6.5 nm [76]. An alternative synthesis method, known as the “heating-up” method, involves mixing all precursors, reagents and solvent together at a low temperature and heating the mixture to a specific temperature. This method yields similar size dispersity as the hot injection method, but may offer greater scalability potential due to its simplicity. Single-shot synthesis yields of up to 40g of nanocrystals have been reported using this method; typical syntheses utilizing the “hot injection” method yield about 0.5 g of nanocrystal material [77]. The most common precursors used for PbS and PbSe syntheses are lead oxide (PbO), oleic acid and bis(trimethylsilyl)sulfide ($(TMS)_2S$) or bis(trimethylsilyl)selenide ((TMS)$_2$Se) [78]. However, (TMS)$_2$S and (TMS)$_2$Se are flammable and toxic, and they readily hydrolyze with water to form toxic H2S and H_2Se. This has led to the development of methods based on alternative precursors, including lead(II) chloride instead of PbO as the lead precursor to improve the surface passivation of the resulting CQDs [79], and elemental sulfur instead of (TMS)$_2$S. Additional novel growth methods have been proposed, including the synthesis of PbSe in a phosphate glass host. The advantage of crystallizing QDs from the porous glass is that more homogeneous, larger crystal sizes exhibiting quantum confinement effects could be achieved versus those achieved in the conventional colloidal growth methods [80].

There are many other colloidal nanocrystal materials that have been synthesized using variations of these methods, including single element materials, such as graphene [81], silicon and germanium, and compound materials. These compounds include binary, mostly III - V and II - VI semiconductors such as metal chalcogenides [82], as well as ternary and quaternary compounds [83].

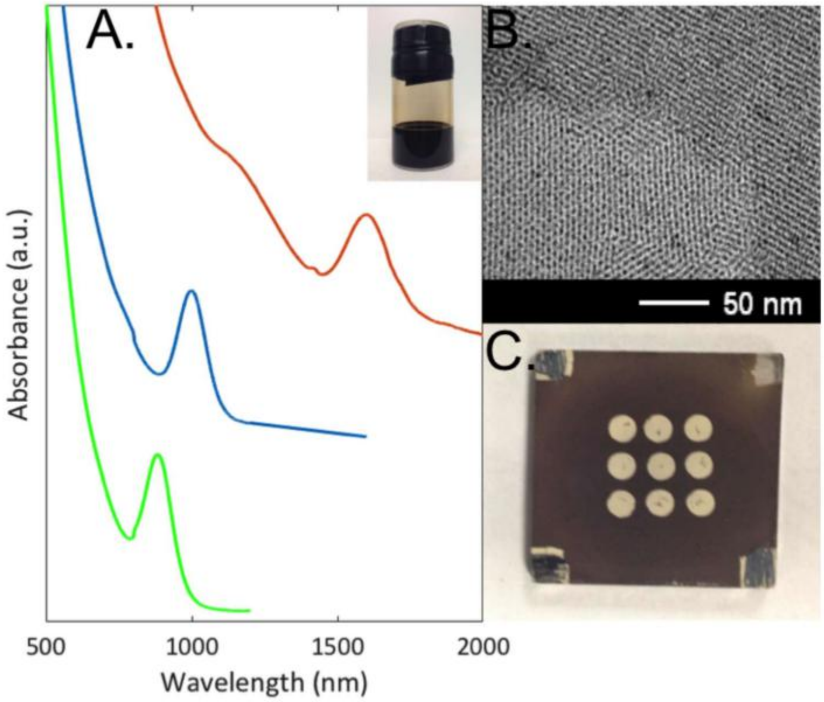

Figure 2.11 (A) Solution-phase absorption spectra of PbS CQDs with excitonic peaks at wavelengths of 880, 1000 and 1600 nm. Spectra are offset for clarity. Inset: photograph of as-synthesized PbS CQD solution with excitonic peak at 955 nm. (B) Transmission electron microscope image of a large ensemble of PbS CQDs with excitonic peak wavelength of 950 nm. (C) Top-view photograph of a 3 × 3 array of PbS CQD photovoltaic cells (full substrate is 1 inch × 1 inch).

2.2.3 Ligands: Stability and Physical Effects

Ligands play an important role in CQD synthesis and electronic film properties [84]. Their main function is to maintain colloidal stability in the solution phase and prevent CQDs from aggregating during the nucleation stage of synthesis. Pb- and Cd-chalcogenide CQDs as-synthesized typically have Pb- and Cd-rich surfaces [85]. There, the ligands also play an important role in passivating electronic trap states that are otherwise present due to the presence of undercoordinated surface atoms. Additionally, ligands help to protect CQDs from oxidative degradation, and can facilitate electronic coupling between neighboring CQDs in the film phase. Long organic ligands, however, can act as electronic tunneling barriers, where the rate of charge transport through the barrier decreases exponentially with the barrier width and the square root of the barrier height [86,87].

Ligand selection can therefore have a large impact on CQD solar cell performance, and much effort has been directed in the field toward engineering ligands for better device operation. Popular ligands for CQD electronic film applications include alkane and aromatic thiols, amines and carboxylic acids [88-91], metal chalcogenide complexes [92] and halogen atoms [93]. Most organic ligands consist of three parts: an inner anchor to the quantum dot, a middle hydrophilic segment and an outer functional group. The freedom in choosing a functional group gives ligated CQD materials versatility for different applications.

Metal halide ligands are well suited for trap state passivation, as their small size allows them to access and passivate exposed surface sites inaccessible to longer organic ligands. Studies have shown that device air stability and efficiency are greatly increased when the CQD active material is treated with Cl-containing ligands [94]. Several specific methods have been developed that take advantage of the properties of halogen ligands. These include a PbS CQD treatment procedure that deployed iodine-based materials to create an air-stable ink [95], and a PbS/CdS coreshell CQD synthesis method that used chlorine-based ligands to achieve a VOC of 0.66 V through the large band gap of CdS and the passivating effects of the Cl. The high performing CQD solar cells today incorporate some halide-based ligands into their CQD films.

Ligands play an important role in the optical properties of CQDs. Better passivated surfaces can increase radiative recombination efficiency, leading to higher photoluminescence quantum yields. Ligands can also facilitate coupling between quantum dots, which can have the effect of red-shifting the absorption and emission spectra and increasing exciton dissociation rates, thereby lowering radiative recombination rates. One study showed that photoluminescence quantum yields could be increased by a factor of 2 when using glutathione (GSH) over tiopronin ligands due to the presence of an inner thiol group in the GSH ligand [96]. Silva et al. later showed that the partial hydrolysis of GSH caused some of the sulfur to react with the CdTe to create a CdS shell that provided better surface passivation. Another study found that when comparing bifunctional carboxylic acid molecules, the more acidic and shorter chains performed the best optically, leading to an excitonic absorption peak red shift due to greater electronic coupling between neighboring dots [97]. This electronic coupling, also seen in the study of 1,3-benzenedithiol (1,3-BDT), ethanedithiol (EDT), mercaptopropionic acid (MPA) and ammonium sulfide, was attributed to the extension of the electron wave function outside the individual CQDs. This resulted in a reduction of the quantum confinement of the particles, decreasing the apparent band gap of the CQDs.

2.2.4 Film Deposition Techniques

One method of forming CQD films for solar cell applications involves layer-by-layer deposition. This process can be carried out under inert or ambient conditions and involves several deposition iterations, as the name implies. One processing step typically includes deposition of the CQDs, followed by a solid-state ligand exchange that densifies the film rendering it insoluble, and several washes with an organic solvent to remove the exchanged ligands [98,99]. The ligand exchange process is vital to improve the overall conductivity of the thin film, as it replaces the long aliphatic synthesis ligands with shorter, often bifunctional, linkers [100].

Methods for depositing the CQDs vary, and include spin-casting [101], dip-coating [102,103], dropcasting, spray-coating and doctorblading. Figure 2.11 (c) shows a CQD solar cell array in which the PbS CQD film was spin-cast using a layer-by-layer deposition process to build up a thick film. One drawback of the layer-by-layer process is the inefficient use of materials inherent in spin-casting, dipcoating and spray-coating processes. Several methods have been proposed to address this limitation, such as developing nanoparticle inks using solution-phase exchanges to shorter ligands [104]. This process allows deposition to occur in a single step that utilizes nearly 100% of the CQD starting solution, and offers distinct material and scalability advantages over the layer-by-layer method. Figure 2.12 shows a comparison between layer-by-layer and single layer deposition techniques [104].

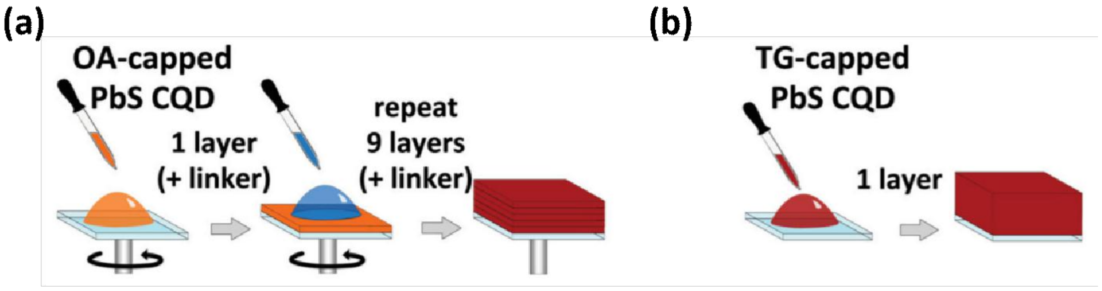

Figure 2.12 Schematic illustration of layer-by-layer deposition (a) and single layer deposition (b) of PbS CQDs from the solution-phase to form films [104].

2.3 Semiconductor Nanowires Synthesis

Semiconductor nanowires are an attractive type of one dimensional nanomaterials for a wide variety of applications, including lasers, photovotaics, photodetection, displays, and biological imaging [105-107]. Due to the quantum confinement effect, their bandgaps and optoelectronic properties can be tuned through size, shape, and composition.

Compared to the physical methods, chemical method provide more versatile approaches for morphology control. One extensively used method to grow semiconductor nanowires is in the vapor phase and generally include vapor-solid and vapor-solid-liquid processes. For the former method, vapor is produced by evaporation or chemical reactions which then convert into solid through condensation [108]. No catalyst is employed and the nanowires are controlled using parameters of temperature, reaction time, and supersaturation ratio. Anisotropy is determined by crystal growth, minimization of the free energy and types of crystal planes. In comparison, the latter process involves catalysts deposition on the substrate which then form droplets via thermal annealing process [109]. Liquid alloy is then formed, nucleation will be initiated once there is supersaturation, and nanowires are obtained through axial growth. Figure 2.13 shows the schematic diagram of the growing process [110]. Silicon, germanium, III-V, and II-VI group semiconductor nanowires have been shown to be successfully grown using vapor growth methods [111].

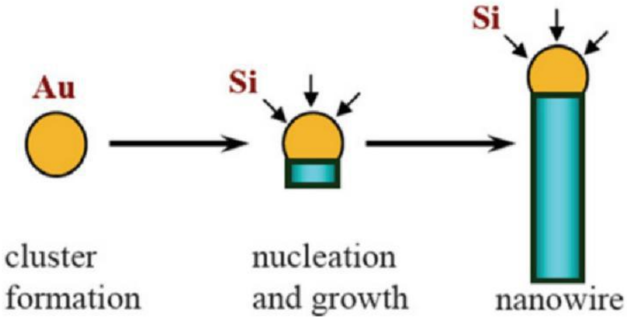

Figure 2.13 Schematic diagram of silicon nanowires growth using vapor-solid-liquid method [110].

Solution processed methods are another type of strategy to obtain nanowires and anisotropic growth is realized by decomposition of precursors in which monomers will form under high temperature. Similarly, supersaturation is required for nucleation. As is shown in Figure 2.14 [112], by using the property of the binding selectivity of ligands towards different facets, growth rate varies with respect to different directions, leading to one dimensional nanowire growth. Examples of semiconductor nanowires synthesized using this method are ZnSe, ZnTe, Bi2S3 NR and CuInS2/ZnS core/shell nanowires [113].

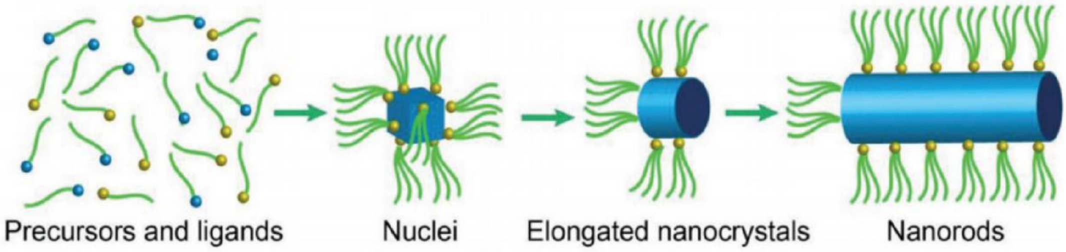

Figure 2.14 Schematic diagram of semiconductor nanowires growth using solution-processed methods via ligands [112].

References

[1] Fan, Xiaofeng, Weitao Zheng, and David J. Singh. "Light scattering and surface plasmons on small spherical particles." Light: Science & Applications 3, no. 6 (2014): e179-e179.

[2] Huang, Yu, Lingwei Ma, Mengjing Hou, Jianghao Li, Zheng Xie, and Zhengjun Zhang. "Hybridized plasmon modes and near-field enhancement of metallic nanoparticle-dimer on a mirror." Scientific reports 6, no. 1 (2016): 1-9.

[3] Yardimci, Nezih Tolga, Semih Cakmakyapan, Soroosh Hemmati, and Mona Jarrahi. "A high-power broadband terahertz source enabled by three-dimensional light confinement in a plasmonic nanocavity." Scientific reports 7, no. 1 (2017): 1-8.

[4] Ohno, Takazumi, Carl Wadell, Satoshi Inagaki, Ji Shi, Yoshio Nakamura, Sachiko Matsushita, and Takumi Sannomiya. "Hole-size tuning and sensing performance of hexagonal plasmonic nanohole arrays." Optical Materials Express 6, no. 5 (2016): 1594-1603.

[5] Genç, Aziz, Javier Patarroyo, Jordi Sancho-Parramon, Raul Arenal, Martial Duchamp, Edgar E. Gonzalez, Luc Henrard et al. "Tuning the plasmonic response up: hollow cuboid metal nanostructures." ACS photonics 3, no. 5 (2016): 770-779.

[6] Valenti, Marco, Anirudh Venugopal, Daniel Tordera, Magnus P. Jonsson, George Biskos, Andreas Schmidt-Ott, and Wilson A. Smith. "Hot carrier generation and extraction of plasmonic alloy nanoparticles." ACS photonics 4, no. 5 (2017): 1146-1152.

[7] Zhang, Hui, Mariia Kramarenko, Johann Osmond, Johann Toudert, and Jordi Martorell. "Natural random nanotexturing of the Au interface for light backscattering enhanced performance in perovskite solar cells." ACS Photonics 5, no. 6 (2018): 2243-2250.

[8] Liu, Zuwei, Wenbo Hou, Prathamesh Pavaskar, Mehmet Aykol, and Stephen B. Cronin. "Plasmon resonant enhancement of photocatalytic water splitting under visible illumination." Nano letters 11, no. 3 (2011): 1111-1116.

[9] Ding, Xianguang, Chi Hao Liow, Mengxin Zhang, Renjun Huang, Chunyan Li, He Shen, Mengya Liu et al. "Surface plasmon resonance enhanced light absorption and photothermal therapy in the second near-infrared window." Journal of the American Chemical Society 136, no. 44 (2014): 15684-15693.

[10] Yu, Renwen, Prantik Mazumder, Nick F. Borrelli, Albert Carrilero, Dhriti S. Ghosh, Rinu A. Maniyara, David Baker, F. Javier Garcia de Abajo, and Valerio Pruneri. "Structural coloring of glass using dewetted nanoparticles and ultrathin films of metals." ACS Photonics 3, no. 7 (2016): 1194-1201.

[11] Kagan, Cherie R., Efrat Lifshitz, Edward H. Sargent, and Dmitri V. Talapin. "Building devices from colloidal quantum dots." Science 353, no. 6302 (2016): aac5523.

[12] De Iacovo, Andrea, Carlo Venettacci, Lorenzo Colace, Leonardo Scopa, and Sabrina Foglia. "PbS Colloidal Quantum Dot Photodetectors operating in the near infrared." Scientific reports 6, no. 1 (2016): 1-9.

[13] Zhao, Haiguang, Jiabin Liu, François Vidal, Alberto Vomiero, and Federico Rosei. "Tailoring the interfacial structure of colloidal “giant” quantum dots for optoelectronic applications." Nanoscale 10, no. 36 (2018): 17189-17197.

[14] Zhao, Yong-Biao, Mengxia Liu, Oleksandr Voznyy, Bin Sun, Pei-Cheng Li, Haoting Kung, Olivier Ouellette et al. "Accelerated solution-phase exchanges minimize defects in colloidal quantum dot solids." Nano Energy 63 (2019): 103876.

[15] “Heritage: Faraday page,” the Royal Institution of Great Britain, http://www.rigb.org/ rimain/heritage/faradaypage.jsp (accessed March 2005).

[16] Chew, Soo Hoon. "Photoemission electron microscopy for nanoscale imaging and attosecond control of light-matter interaction at metal surfaces." PhD diss., lmu, 2018.

[17] Kawata, Satoshi, Yasushi Inouye, and Prabhat Verma. "Plasmonics for near-field nano-imaging and superlensing." Nature photonics 3, no. 7 (2009): 388.

[18] Atwater, Harry A., and Albert Polman. "Plasmonics for improved photovoltaic devices." In Materials For Sustainable Energy: A Collection of Peer-Reviewed Research and Review Articles from Nature Publishing Group, pp. 1-11. 2011.

[19] Jang, Yoon Hee, Yu Jin Jang, Seokhyoung Kim, Li Na Quan, Kyungwha Chung, and Dong Ha Kim. "Plasmonic solar cells: from rational design to mechanism overview." Chemical reviews 116, no. 24 (2016): 14982-15034.

[20] Mahmoud, Mahmoud A., Maysamreza Chamanzar, Ali Adibi, and Mostafa A. El-Sayed. "Effect of the dielectric constant of the surrounding medium and the substrate on the surface plasmon resonance spectrum and sensitivity factors of highly symmetric systems: silver nanocubes." Journal of the American Chemical Society 134, no. 14 (2012): 6434-6442.

[21] Zhao, Jing, Xiaoyu Zhang, Chanda Ranjit Yonzon, Amanda J. Haes, and Richard P. Van Duyne. "Localized surface plasmon resonance biosensors." (2006): 219-228.

[22] Zhang, Renhe, Yao Zhang, Z. C. Dong, S. Jiang, C. Zhang, L. G. Chen, L. Zhang et al. "Chemical mapping of a single molecule by plasmon-enhanced Raman scattering." Nature 498, no. 7452 (2013): 82-86.

[23] Musa, Sarhan M., ed. Computational nanophotonics: modeling and applications. CRC Press, 2013.

[24] U. Kreibig and M. Vollmer, Optical Properties of Metal Clusters (Springer, New York, 1995).

[25] Xu, Hongxing, and Mikael Käll. "Surface-plasmon-enhanced optical forces in silver nanoaggregates." Physical review letters 89, no. 24 (2002): 246802.

[26] Wriedt, Thomas. "Mie theory: a review." In The Mie Theory, pp. 53-71. Springer, Berlin, Heidelberg, 2012.

[27] Saj, W. M. "FDTD simulations of 2D plasmon waveguide on silver nanorods in hexagonal lattice." Optics Express 13, no. 13 (2005): 4818-4827.

[28] Jiang, Ruibin, Huanjun Chen, Lei Shao, Qian Li, and Jianfang Wang. "Unraveling the evolution and nature of the plasmons in (Au core) – (Ag shell) nanorods." Advanced Materials 24, no. 35 (2012): OP200-OP207.

[29] Zhang, An-Qi, Dong-Jin Qian, and Meng Chen. "Simulated optical properties of noble metallic nanopolyhedra with different shapes and structures." The European Physical Journal D 67, no. 11 (2013): 231.

[30] Seh, Zhi Wei, Shuhua Liu, Michelle Low, Shuang - Yuan Zhang, Zhaolin Liu, Adnen Mlayah, and Ming - Yong Han. "Janus Au - TiO2 photocatalysts with strong

localization of plasmonic near‐fields for efficient visible‐light hydrogen generation." Advanced Materials 24, no. 17 (2012): 2310-2314.

[31] Liu, Na, Ming L. Tang, Mario Hentschel, Harald Giessen, and A. Paul Alivisatos. "Nanoantenna-enhanced gas sensing in a single tailored nanofocus." Nature materials 10, no. 8 (2011): 631-636.

[32] Link, Stephan, and Mostafa A. El-Sayed. "Size and temperature dependence of the plasmon absorption of colloidal gold nanoparticles." The Journal of Physical Chemistry B 103, no. 21 (1999): 4212-4217.

[33] Sherry, Leif J., Shih-Hui Chang, George C. Schatz, Richard P. Van Duyne, Benjamin J. Wiley, and Younan Xia. "Localized surface plasmon resonance spectroscopy of single silver nanocubes." Nano letters 5, no. 10 (2005): 2034-2038.

[34] Naik, Gururaj V., Vladimir M. Shalaev, and Alexandra Boltasseva. "Alternative plasmonic materials: beyond gold and silver." Advanced Materials 25, no. 24 (2013): 3264-3294.

[35] Naik, Gururaj V., Jongbum Kim, and Alexandra Boltasseva. "Oxides and nitrides as alternative plasmonic materials in the optical range." Optical Materials Express 1, no. 6 (2011): 1090-1099.

[36] Wang, Yu, Antonio Capretti, and Luca Dal Negro. "Wide tuning of the optical and structural properties of alternative plasmonic materials." Optical Materials Express 5, no. 11 (2015): 2415-2430.

[37] Knight, Mark W., Nicholas S. King, Lifei Liu, Henry O. Everitt, Peter Nordlander, and Naomi J. Halas. "Aluminum for plasmonics." ACS nano 8, no. 1 (2014): 834-840.

[38] Liu, Hsuan-Wei, Fan-Cheng Lin, Shi-Wei Lin, Jau-Yang Wu, Bo-Tsun Chou, Kuang-Jen Lai, Sheng-Di Lin, and Jer-Shing Huang. "Single-crystalline aluminum nanostructures on a semiconducting GaAs substrate for ultraviolet to near-infrared plasmonics." ACS nano 9, no. 4 (2015): 3875-3886.

[39] Olson, Jana, Alejandro Manjavacas, Lifei Liu, Wei-Shun Chang, Benjamin Foerster, Nicholas S. King, Mark W. Knight, Peter Nordlander, Naomi J. Halas, and Stephan Link. "Vivid, full-color aluminum plasmonic pixels." Proceedings of the national academy of sciences 111, no. 40 (2014): 14348-14353.

[40] Jha, Shankar K., Zeeshan Ahmed, Mario Agio, Yasin Ekinci, and Jörg F. Löffler. "Deep-UV surface-enhanced resonance Raman scattering of adenine on

aluminum nanoparticle arrays." Journal of the American Chemical Society 134, no. 4 (2012): 1966-1969.

[41] Al-Ghamdi, Haifa S., and Waleed E. Mahmoud. "One pot synthesis of multi-plasmonic shapes of silver nanoparticles." Materials Letters 105 (2013): 62-64.

[42] Zhang, Qiang, Weiyang Li, Christine Moran, Jie Zeng, Jingyi Chen, Long-Ping Wen, and Younan Xia. "Seed-mediated synthesis of Ag nanocubes with controllable edge lengths in the range of 30 − 200 nm and comparison of their optical properties." Journal of the American Chemical Society 132, no. 32 (2010): 11372-11378.

[43] Nazemi, Mohammadreza, and Mostafa A. El-Sayed. "Electrochemical synthesis of ammonia from N2 and H2O under ambient conditions using pore-size-controlled hollow gold nanocatalysts with tunable plasmonic properties." The journal of physical chemistry letters 9, no. 17 (2018): 5160-5166.

[44] Bastús, Neus G., Joan Comenge, and Víctor Puntes. "Kinetically controlled seeded growth synthesis of citrate-stabilized gold nanoparticles of up to 200 nm: size focusing versus Ostwald ripening." Langmuir 27, no. 17 (2011): 11098-11105.

[45] Preciado-Flores, Sandra, Danchen Wang, Damon A. Wheeler, Rebecca Newhouse, Jennifer K. Hensel, Adam Schwartzberg, Lihua Wang, Junjie Zhu, Marcelino Barboza-Flores, and Jin Z. Zhang. "Highly reproducible synthesis of hollow gold nanospheres with near infrared surface plasmon absorption using PVP as stabilizing agent." Journal of Materials Chemistry 21, no. 7 (2011): 2344-2350.

[46] McClain, Michael J., Andrea E. Schlather, Emilie Ringe, Nicholas S. King, Lifei Liu, Alejandro Manjavacas, Mark W. Knight et al. "Aluminum nanocrystals." Nano letters 15, no. 4 (2015): 2751-2755.

[47] Lu, Shaoyong, Hua Yu, Samuel Gottheim, Huimin Gao, Christopher J. DeSantis, Benjamin D. Clark, Jian Yang et al. "Polymer-Directed Growth of Plasmonic Aluminum Nanocrystals." Journal of the American Chemical Society 140, no. 45 (2018): 15412-15418.

[48] Xiong, Yujie, and Younan Xia. "Shape‐controlled synthesis of metal nanostructures: the case of palladium." Advanced Materials 19, no. 20 (2007): 3385-3391.

[49] Lu, Jun, Yi-Xin Chang, Ning-Ning Zhang, Ying Wei, Ai-Ju Li, Jia Tai, Yao Xue et al. "Chiral plasmonic nanochains via the self-assembly of gold nanorods and helical

glutathione oligomers facilitated by cetyltrimethylammonium bromide micelles." ACS nano 11, no. 4 (2017): 3463-3475.

[50] Cobley, Claire M., Sara E. Skrabalak, Dean J. Campbell, and Younan Xia. "Shape-controlled synthesis of silver nanoparticles for plasmonic and sensing applications." Plasmonics 4, no. 2 (2009): 171-179.

[51] Jin, Rongchao, Y. Charles Cao, Encai Hao, Gabriella S. Métraux, George C. Schatz, and Chad A. Mirkin. "Controlling anisotropic nanoparticle growth through plasmon excitation." Nature 425, no. 6957 (2003): 487-490.

[52] Clark, Benjamin D., Christian R. Jacobson, Minhan Lou, Jian Yang, Linan Zhou, Sam Gottheim, Christopher J. DeSantis, Peter Nordlander, and Naomi J. Halas. "Aluminum nanorods." Nano letters 18, no. 2 (2018): 1234-1240.

[53] Clark, Benjamin D., Christian R. Jacobson, Minhan Lou, David Renard, Gang Wu, Luca Bursi, Arzeena S. Ali et al. "Aluminum nanocubes have sharp corners." ACS nano 13, no. 8 (2019): 9682-9691.

[54] Baek, Se-Woong, Garam Park, Jonghyeon Noh, Changsoon Cho, Chun-Ho Lee, Min-Kyo Seo, Hyunjoon Song, and Jung-Yong Lee. "Au@ Ag core – shell nanocubes for efficient plasmonic light scattering effect in low bandgap organic solar cells." Acs Nano 8, no. 4 (2014): 3302-3312.

[55] Liu, Fei, Shailja Goyal, Michael Forrester, Tao Ma, Kyle Miller, Yasmeen Mansoorieh, John Henjum, Lin Zhou, Eric Cochran, and Shan Jiang. "Self-assembly of Janus dumbbell nanocrystals and their enhanced surface plasmon resonance." Nano letters 19, no. 3 (2018): 1587-1594.

[56] Choi, Yoonjung, Soonchang Hong, Lichun Liu, Seong Kyu Kim, and Sungho Park. "Galvanically replaced hollow Au – Ag nanospheres: Study of their surface plasmon resonance." Langmuir 28, no. 16 (2012): 6670-6676.

[57] Zhou, Xuemei, Gang Liu, Jiaguo Yu, and Wenhong Fan. "Surface plasmon resonance-mediated photocatalysis by noble metal-based composites under visible light." Journal of Materials Chemistry 22, no. 40 (2012): 21337-21354.

[58] Tan, Shawn J., Michael J. Campolongo, Dan Luo, and Wenlong Cheng. "Building plasmonic nanostructures with DNA." Nature nanotechnology 6, no. 5 (2011): 268.

[59] Groeneveld, Rogier HM, Rudolf Sprik, and Ad Lagendijk. "Femtosecond spectroscopy of electron-electron and electron-phonon energy relaxation in Ag and Au." Physical Review B 51, no. 17 (1995): 11433.

[60] Brongersma, Mark L., Naomi J. Halas, and Peter Nordlander. "Plasmon-induced hot carrier science and technology." Nature nanotechnology 10, no. 1 (2015): 25.

[61] Wu, Kaifeng, Jinquan Chen, James R. McBride, and Tianquan Lian. "Efficient hot-electron transfer by a plasmon-induced interfacial charge-transfer transition." Science 349, no. 6248 (2015): 632-635.

[62] Lauth, Jannika, Sachin Kinge, and Laurens DA Siebbeles. "Ultrafast Transient Absorption and Terahertz Spectroscopy as Tools to Probe Photoexcited States and Dynamics in Colloidal 2D Nanostructures." Zeitschrift für Physikalische Chemie 231, no. 1 (2017): 107-119.

[63] Cheng, Yan, Ebuka S. Arinze, Nathan Palmquist, and Susanna M. Thon. "Advancing colloidal quantum dot photovoltaic technology." Nanophotonics 5, no. 1 (2016): 31-54.

[64] Hou, Bo, Yuljae Cho, Byung Sung Kim, John Hong, Jong Bae Park, Se Jin Ahn, Jung Inn Sohn, SeungNam Cha, and Jong Min Kim. "Highly monodispersed PbS quantum dots for outstanding cascaded-junction solar cells." ACS energy letters 1, no. 4 (2016): 834-839.

[65] Hou, Bo, Yuljae Cho, Byung Sung Kim, John Hong, Jong Bae Park, Se Jin Ahn, Jung Inn Sohn, SeungNam Cha, and Jong Min Kim. "Highly monodispersed PbS quantum dots for outstanding cascaded-junction solar cells." ACS energy letters 1, no. 4 (2016): 834-839.

[66] Brus L. Electronic wave functions in semiconductor clusters: experiment and theory. J Phys Chem 1986, 90, 2555 – 60.

[67] Zhao, Haiguang, and Federico Rosei. "Colloidal quantum dots for solar technologies." Chem 3, no. 2 (2017): 229-258.

[68] Moreels I, Lambert K, Smeets D, et al. Size-Dependent Optical Properties of Colloidal PbS Quantum Dots. ACS Nano 2009, 3, 3023 – 30.

[69] Miller OD, Yablonovitch E, Kurtz SR. Strong Internal and External Luminescence as Solar Cells Approach the Shockley #x2013;Queisser Limit. IEEE J Photovolt 2012, 2, 303 – 11.

[70] Ip AH, Thon SM, Hoogland S, et al. Hybrid passivated colloidal quantum dot solids. Nat Nanotechnol 2012, 7, 577 – 82

[71] Klimov VI, Mikhailovsky AA, Xu S, et al. Optical Gain and Stimulated Emission in Nanocrystal Quantum Dots. Science 2000, 290, 314 – 7.

[72] McDonald SA, Konstantatos G, Shiguo Zhang, et al. Solutionprocessed PbS quantum dot infrared photodetectors and photovoltaics. Nat Mater 2005, 4, 138 – 42.

[73] Ekuma CE, Singh DJ, Moreno J, Jarrell M. Optical properties of PbTe and PbSe. Phys Rev B 2012, 85, 085205.

[74] Hines MA, Scholes GD. Colloidal PbS Nanocrystals with Size-Tunable Near-Infrared Emission: Observation of PostSynthesis Self-Narrowing of the Particle Size Distribution. Adv Mater 2003, 15, 1844 – 9.

[75] Park J, Joo J, Kwon SG, Jang Y, Hyeon T. Synthesis of Monodisperse Spherical Nanocrystals. Angew Chem Int Ed 2007, 46, 4630 – 60.

[76] Moreels I, Justo Y, De Geyter B, Haustraete K, Martins JC, Hens Z. Size-Tunable, Bright, and Stable PbS Quantum Dots: A Surface Chemistry Study. ACS Nano 2011, 5, 2004 – 12.

[77] Park J, An K, Hwang Y, et al. Ultra-large-scale syntheses of monodisperse nanocrystals. Nat Mater 2004, 3, 891 – 5.

[78] Ma W, Swisher SL, Ewers T, et al. Photovoltaic Performance of Ultrasmall PbSe Quantum Dots. ACS Nano 2011, 5, 8140 – 7.

[79] Zhang J, Gao J, Miller EM, Luther JM, Beard MC. DiffusionControlled Synthesis of PbS and PbSe Quantum Dots with in Situ Halide Passivation for Quantum Dot Solar Cells. ACS Nano 2014, 8, 614 – 22.

[80] Borrelli NF, Smith DW. Quantum confinement of PbS microcrystals in glass. J Non-Cryst Solids 1994, 180, 25 – 31.

[81] Yan X, Cui X, Li L. Synthesis of Large, Stable Colloidal Graphene Quantum Dots with Tunable Size. J Am Chem Soc 2010, 132, 5944 – 5.

[82] Guzelian AA, Banin U, Kadavanich AV, Peng X, Alivisatos AP. Colloidal chemical synthesis and characterization of InAs nanocrystal quantum dots. Appl Phys Lett 1996, 69, 1432 – 4.

[83] Nose K, Omata T, Otsuka-Yao-Matsuo S. Colloidal Synthesis of Ternary Copper Indium Diselenide Quantum Dots and Their Optical Properties. J Phys Chem C 2009, 113, 3455 – 60.

[84] Green M. The nature of quantum dot capping ligands. J Mater Chem 2010, 20, 5797 – 809.

[85] Taylor J, Kippeny T, Rosenthal SJ. Surface Stoichiometry of CdSe Nanocrystals Determined by Rutherford Backscattering Spectroscopy. J Clust Sci 2001, 12, 571 – 82.

[86] Talapin DV, Lee J-S, Kovalenko MV, Shevchenko EV. Prospects of Colloidal Nanocrystals for Electronic and Optoelectronic Applications. Chem Rev 2010, 110, 389 – 458.

[87] Kovalenko MV, Scheele M, Talapin DV. Colloidal Nanocrystals with Molecular Metal Chalcogenide Surface Ligands. Science 2009, 324, 1417 – 20.

[88] Uyeda HT, Medintz IL, Jaiswal JK, Simon SM, Mattoussi H. Synthesis of Compact Multidentate Ligands to Prepare Stable Hydrophilic Quantum Dot Fluorophores. J Am Chem Soc 2005, 127, 3870 – 8.

[89] Klem EJD, Shukla H, Hinds S, MacNeil DD, Levina L, Sargent EH. Impact of dithiol treatment and air annealing on the conductivity, mobility, and hole density in PbS colloidal quantum dot solids. Appl Phys Lett 2008, 92, 212105.

[90] Giansante C, Carbone L, Giannini C, et al. Colloidal Arenethiolate-Capped PbS Quantum Dots: Optoelectronic Properties, Self-Assembly, and Application in Solution-Cast Photovoltaics. J Phys Chem C 2013, 117, 13305 – 17.

[91] Barkhouse DAR, Pattantyus-Abraham AG, Levina L, Sargent EH. Thiols Passivate Recombination Centers in Colloidal Quantum Dots Leading to Enhanced Photovoltaic Device Eflciency. ACS Nano 2008, 2, 2356 – 62.

[92] Kovalenko MV, Scheele M, Talapin DV. Colloidal Nanocrystals with Molecular Metal Chalcogenide Surface Ligands. Science 2009, 324, 1417 – 20.

[93] Greaney MJ, Couderc E, Zhao J, et al. Controlling the Trap State Landscape of Colloidal CdSe Nanocrystals with Cadmium Halide Ligands. Chem Mater 2015, 27, 744 – 56.

[94] Zhang J, Gao J, Miller EM, Luther JM, Beard MC. DiffusionControlled Synthesis of PbS and PbSe Quantum Dots with in Situ Halide Passivation for Quantum Dot Solar Cells. ACS Nano 2014, 8, 614 – 22.

[95] Ning Z, Dong H, Zhang Q, Voznyy O, Sargent EH. Solar Cells Based on Inks of n-Type Colloidal Quantum Dots. ACS Nano 2014, 8, 10321 – 7

[96] Liu Y-F, Yu J-S. Selective synthesis of CdTe and high luminescence CdTe/CdS quantum dots: The effect of ligands. J Colloid Interface Sci 2009, 333, 690 – 8.

[97] Smith AR, Yoon W, Heuer WB, et al. Effect of Ligand Structure on the Optical and Electronic Properties of Nanocrystalline PbSe Films. J Phys Chem C 2012, 116, 6031 – 7.

[98] Kirmani AR, Carey GH, Abdelsamie M, et al. Effect of Solvent Environment on Colloidal-Quantum-Dot Solar-Cell Manufacturability and Performance. Adv Mater 2014, 26, 4717 – 23.

[99] Cassagneau T, Mallouk TE, Fendler JH. Layer-by-Layer Assembly of Thin Film Zener Diodes from Conducting Polymers and CdSe Nanoparticles. J Am Chem Soc 1998, 120, 7848 – 59.

[100] Liu Y, Gibbs M, Puthussery J, et al. Dependence of Carrier Mobility on Nanocrystal Size and Ligand Length in PbSe Nanocrystal Solids. Nano Lett 2010, 10, 1960 – 9.

[101] Konstantatos G, Howard I, Fischer A, et al. Ultrasensitive solution-cast quantum dot photodetectors. Nature 2006, 442, 180 – 3.

[102] Lee J-W, Son D-Y, Ahn TK, et al. Quantum-Dot-Sensitized Solar Cell with Unprecedentedly High Photocurrent. Sci Rep 2013, 3.

[103] Luther JM, Law M, Beard MC, et al. Schottky Solar Cells Based on Colloidal Nanocrystal Films. Nano Lett 2008, 8, 3488 – 92.

[104] Fischer A, Rollny L, Pan J, et al. Directly Deposited Quantum Dot Solids Using a Colloidally Stable Nanoparticle Ink. Adv Mater 2013, 25, 5742 – 9.

Chapter 3

Optoelectronic Devices for Energy Conversion

3.1 Photocatalysis

3.1.1 Motivation and Challenges

Increasing energy consumption due to the growing population and pollution of water and air have become serious worldwide challenges. Photocatalysis is considered as an alternative route to conventional organic synthesis. It utilizes sun energy which is abundant and clean to drive chemical reactions and produced no chemical waste [1]. The most widely used photocatalyst is TiO_2 which has a high surface density of states, high reactivity, and is chemically stable. It has been applied in important energy-relevant reactions, including water splitting and CO_2 reduction [2]. Other semiconductors used as photocatalysts include ZnO, Fe_2O_3, ZnS, and CdS [3-5]. However, despite many successful demonstrations, the photocatalytic efficiency of TiO_2 remains low due to several reasons. TiO_2 is a wide bandgap (3.2 eV) semiconductor which only absorbs UV illumination while solar radiation is mainly in the visible and near infrared, leading to low conversion efficiency. Furthermore, it has an indirect bandgap and high density of mid-gap electronic trap states. The photoexcited electron-hole pairs will recombine through nonradiative pathways on a short timescale (picoseconds to milliseconds) instead of participating in redox reactions [6]. The specific recombination rate is influenced by parameters such as light intensity and temperature. Generally, anatase TiO_2 has longer carrier lifetimes than rutile TiO_2 and therefore serves as a better choice for efficient photocatalysis. Low selectivity towards a desirable product is also a limiting factor for effective TiO_2 catalysis.

3.3.2 Conventional Photocatalysts

Fig. 3.1 shows the basic mechanism for photocatalytic reactions. Upon light illumination, photons with energies equal to or greater than the bandgap of the semiconductor photocatalyst will be able to excite electrons to the conduction band. A portion of the generated carriers will be separated, recombine and finally release energy in the form of heat or reemission of photons in the bulk or on the surface, leading to a low quantum efficiency.

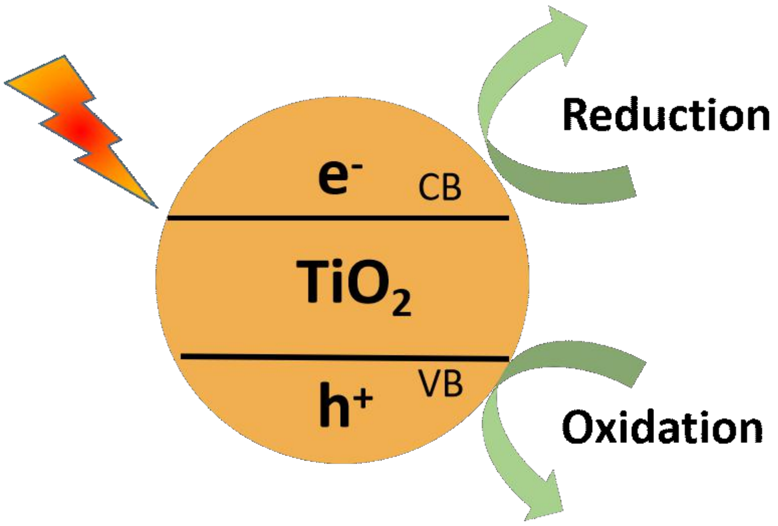

Figure 3.1 The general process of direct photocatalysis within a semiconductor material is depicted.

Some electrons and holes will successfully transit to the surface to catalyze oxidation and reduction reactions depending on the relative energy levels of the semiconductor and the redox levels of the reactants. As is shown in Figure 3.2 [7], when the redox level of the reactant molecules is higher than the valence band or lower than the conduction band of the semiconductor, oxidation or reduction will take place.

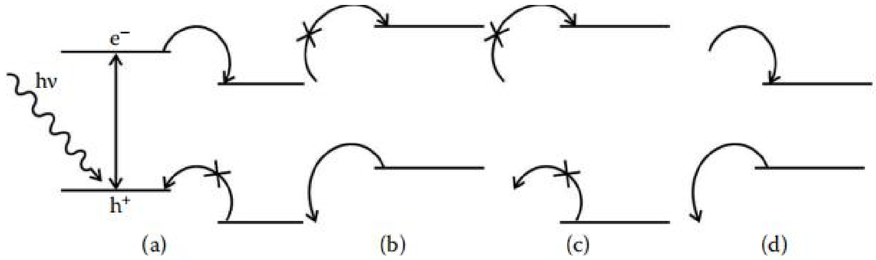

Figure 3.2 Different energy level alignments between semiconductor photocatalysts and reactant molecules leads to (a) reduction, (b) oxidation, (c) no reaction, (d) redox reaction [7].

3.3.3 Surface Plasmon-Sensitized Photocatalysis

Plasmonic nanostructures have been used as visible light sensitizers for enhancing the low absorption in semiconductor photocatalysts [8]. Figure 3.3 shows the typical processes that would occur in plasmonic NP/semiconductor systems and is explained as follows.

(1) Localized surface plasmons are excited within the metal nanostructures which quickly dephases and decay into energetic hot carriers.

(2) Since a Schottky barrier is formed at the interface, electrons with enough energy will overcome the potential and migrate to the semiconductors. This collection efficiency is described by Fowler’s theory which shows dependence on the energy difference between the hot carriers and the barrier height.

(3) Electrons injected into the semiconductor will aid in reducing the adsorbed species.

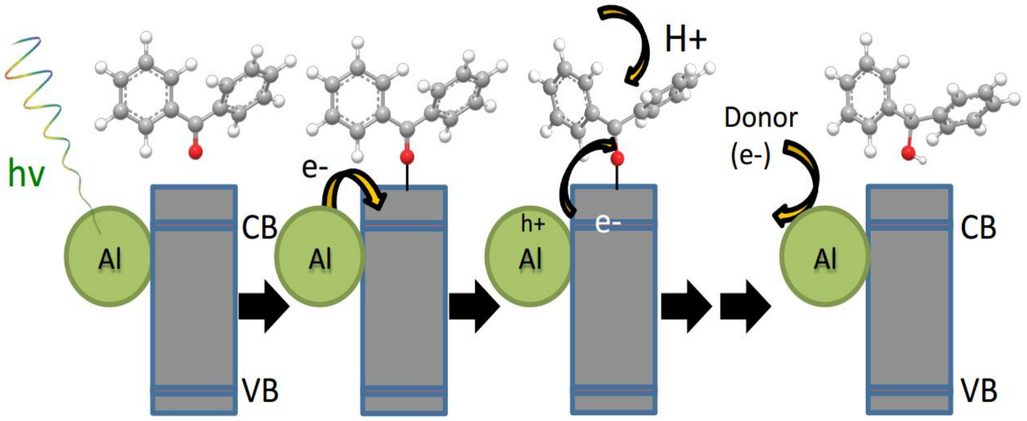

Figure 3.3 Schematic diagram showing the process of light excitation, hot carrier generation and transfer, and redox reactions with adsorbed molecules.

To efficiently utilize hot carriers and provide more insight into the mechanism of plasmonically-enhanced photocatalysis, it is crucial to study timescales of both electron relaxation in metal NPs and electron transfer from the particle to the semiconductor. TAS has been widely employed to study this dynamic process and obtain the relative timescales [9]. For noble metal NPs, the electron-electron relaxation is around 10-100 fs and a transfer time within 240 fs is observed in Au/TiO_2 samples as indicated by an absorption rise in TAS. Therefore, hot carriers are injected over the barrier while they thermally relax through scattering.

Early demonstrations of catalytic Au/TiO_2 nanopowders were shown to increase the reaction rates of both acetic acid and 2-propanol oxidation [10]. A direct electron transfer mechanism from Au to TiO_2 was proposed and increase of catalytic activity due to plasmonic near-field enhancement in the Au was ruled out. Given that smaller metal NPs have been observed to be more active than larger ones, Au NPs with diameters of less than 5 nm have been combined with anatase/rutile TiO_2 nanostructures to achieve aerobic oxidation of alcohols [11]. Under visible light radiation, the system showed enhancement in photocatalytic activity compared to the case in the dark. The performance of Au/TiO_2 was strongly affected by the anatase and rutile interface which contributed to efficient carrier transfer. Ligand exchange processes for Au NPs have also been proven to help with efficient electron injection. By replacing the long chain organic ligands (polyvinylpyrrolidone) with 3-mercaptopropionic acid and later complete removal by vacuum evaporation, the decomposition rate was enhanced with control over monodispersity [12]. It was further proposed that Au/CeO_2 core-shell structures could increase the probability of hot carrier utilization. A greater yield of benzaldehyde was achieved using the core-shell system compared to a mixture of Au and CeO_2 composites [13].

3.2 Solar Cells

3.2.1 Operational Principles and Figures of Merit

Solar cells are two-terminal optoelectronic devices that convert light into electricity via the photovoltaic effect. Figure. 3.4 [14] is a schematic diagram that shows the operation of a solar cell. When solar radiation is incident on the cell, photons with energies greater than the bandgap of the semiconductor (absorbing material) will generate electron-hole pairs which can be separated and efficiently collected. This leads to a photocurrent in the external circuit and the generation of a large voltage, providing power to the external load. Figure 3.4 shows example light and dark current-voltage (I-V or J-V) curves for a solar cells. The light J-V curve is shifted from the dark curve as a function of light intensity.

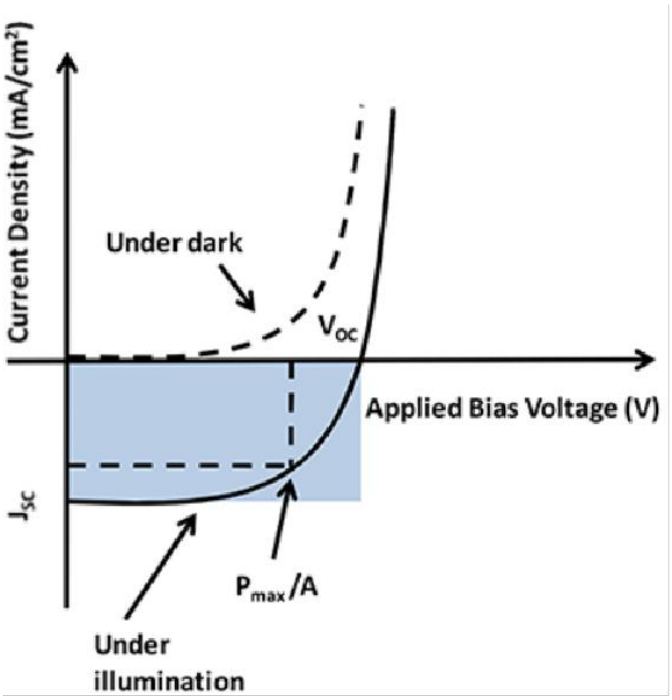

Figure 3.4 Example current-voltage characteristic curves of a solar cell in the dark and under illumination [14].

In practice, there are other effects, such as series and shunt resistance and trap state mediated recombination, which lead to an I-V relationship that deviates from the ideal case, as is expressed in Equation 3.1. I_L is the short circuit photocurrent, I_0 is the saturation current, R_S and R_{SH} are the series and shunt resistance, respectively, and n is the diode ideality factor.

$$I = I_L - I_0 \exp[\frac{q(V + IR_S)}{nkT}] - \frac{V + IR_S}{R_{SH}} \tag{3.1}$$

The performance of a solar cell is typically quantified by several figures of merit [15]. The short-circuit current, I_{SC}, is the current that flows through a photovoltaic device at zero bias. I_{SC} depends on the generation and collection of charge carriers, and the area-independent short-circuit current density, or J_{SC}, is often employed in its place. The open-circuit voltage, V_{OC}, is the maximum photovoltage obtained from a solar cell device at zero current. The V_{OC} is largely dependent on the band gap or absorption edge of the photovoltaic material and can be reduced by recombination processes. The fill factor, *FF*, is a measure of the squareness of the current-voltage curve and is defined as the ratio of the current times the voltage at the device maximum power point of operation to the product of I_{SC} and V_{OC}. The power conversion efficiency, PCE, is the ratio of the maximum power from the device to the input power from the sun. PCE is calculated using Equation 3.2, where 100 mW/cm^2 is the AM1.5G standard terrestrial solar irradiance.

$$\mathrm{PCE} = \mathrm{J_{SC}} \times \mathrm{V_{OC}} \times \mathrm{FF}/100\ \mathrm{mW/cm^2} \qquad (3.2)$$

3.2.2 Device Architectures of Near-infrared Colloidal Quantum Dot Solar Cells

Near-infrared CQD solar cells fall under the general class of “third generation” solar cells with promising theoretical conversion efficiencies exceeding the Schockley-Queisser limit. They exhibit the advantages of low cost, ease of fabrication, near-infrared sensitivity for efficient light harvesting, the potential for multiple exciton generation, and bandgap tunability which is potentially useful for multijunction solar cells.

Early devices that used CQDs as the absorbing layer employed a Schottky or metal-semiconductor junction for operation [16]. They relied primarily on the difference in work functions for the transparent conductive oxide (TCO), and the top metal electrode to generate a built-in field and promote the flow of a photocurrent across the absorbing medium. This absorbing medium was initially a polymer CQD composite layer; however, after further studies on the electronic impact of the polymer [17], the composite was replaced with a pure CQD layer. Figure 3.5(a) shows the structure of a CQD Schottky junction solar cell. These solar cell designs that used CQDs as both the absorbing medium and charge transport medium were based on the rectifying junction present at the p-type PbX (X = S or Se) CQD film and shallow work function metal interface. Various materials, including Al, Ca, Mg and Ag have been used as the shallow work function metal in Schottky devices [18-21]. Improvements in the performances of these devices led to PCEs exceeding 3%, and air stability was improved through engineering of the stabilizing ligands [22]. The air stability was further improved through the insertion of a LiF blocker at the semiconductor–metal interface to limit degradation. Further studies on improving the air stabilities of Schottky cells have involved inverting the junction and oxidation of the CQDs at the semiconductor–metal interface. The CQD Schottky architecture has several advantages, such as functional simplicity and ease of fabrication, and has achieved PCEs exceeding 5% [23]. The major drawback of this architecture is Fermi level pinning at the rectifying junction which limits the V_{OC} to well under the band gap of the material.

As a means to overcome the limitations of the Schottky junction architecture, the depleted heterojunction (DH) CQD solar cell was developed [24]. The DH architecture consists of an n-type electron acceptor forming a heterojunction with a p-type CQD film. The full device structure starts with a substrate (usually glass or a flexible transparent material) with a transparent conductive oxide (TCO, usually indium tin oxide or fluorinedoped tin oxide). The electron acceptor or n-doped layer is a wide band gap semiconductor, such as TiO_2 or ZnO, and the absorbing p-type CQD film layer is deposited on top of this layer. Finally, the device is completed with an optional highly doped metal oxide, such as molybdenum trioxide (MoO_3), and a hole-collecting deep work function metal such as gold. As a hole extraction layer, MoO_3 has a large work function.

Further improvements in DH solar cells were realized by replacing the MoO_3 hole extraction layer with a thin layer of PbS CQDs employing ethanedithiol (EDT) ligands which facilitated optimal band alignment with the PbS CQD absorbing layer, as well as achieving superior long term stability in air. Figure 3.5(b) shows the architecture of a photovoltaic cell employing the DH design. An additional limitation of Schottky junction devices is the distance between the photogeneration plane, located near the CQD-TCO interface, and the charge separation junction, located at the CQD–metal interface. The DH architecture eliminates this issue as photogeneration occurs very close to the metal oxide–CQD junction itself. The doping levels of each material determine the depletion widths on both sides of the junction; typically, the n-type wide band gap semiconductor is highly doped to ensure that more of the depletion region falls on the CQD film side. The electric field associated with the depletion layer helps promote charge extraction through the CQD film by extending charge transport beyond the carrier diffusion length [25].

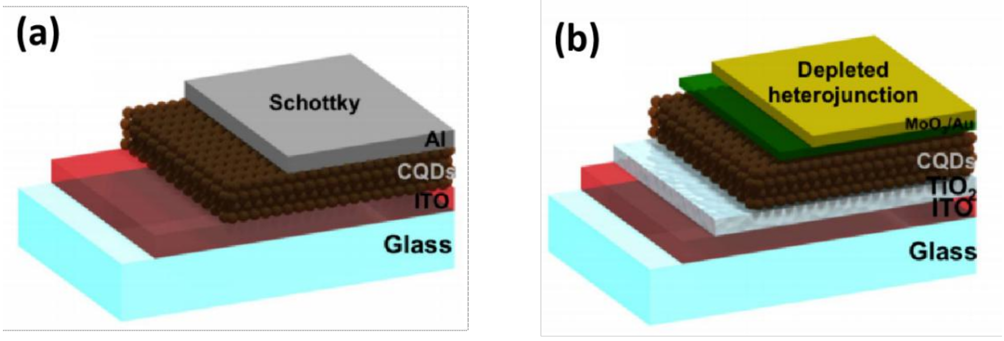

Figure 3.5 Schematic of different CQD solar cell architectures employing: (a) a Schottky junction and (b) a depleted heterojunction.

In theory, homojunction-type devices offer advantages over heterojunction devices due to the elimination of potential voltage losses due to band offsets. Fabricating such a structure out of CQD films has been difficult due to the need to engineer both n- and p-type CQDs. An initial homojunction demonstration was enabled by the fabrication of stable n-type CQD films [26]. The doping character of

CQD films is determined by the net stoichiometry of the system considering both the CQD cores and ligands. In practice, CQD doping types are affected by the ligands and the chemical processing environments. Halide anion ligands, delivered through tetrabutylammonium iodide or cadmium bromide/iodide treatments, have proven to be efficient in achieving n-type doping of CQD films under inert atmosphere processing conditions [27,28]. Additionally, PbS CQDs can be treated with Ag ions during synthesis to increase the doping density on the p-side of the junction, thereby extending the electric field farther into the lightly doped n-type films [29]. Bidoping has also been successfully used to achieve n-type doping of PbS CQDs [30]. Further optimization of the homojunction device design resulted in a field-enhanced device, which employed engineering of the electric field profile of the junction region. Recently, bulk CQD homojunction PbS solar cells were fabricated with a record PCE of 13.3% [31]. Using a cascade surface modification process, the carrier diffusion length in bulk PbS CQD films increased considerably to 340 nm.

3.3 Photodetectors

Photodetectors are optical sensors that convert optical signals to electric current through a photoconductive or photovoltaic effect. They are exploited in a wide variety of applications both in industry and research labs. They are used in imaging sensors such as digital cameras, free space communications, medical equipment, and consumer electronic devices such as remote controls and televisions.

3.3.1 Figures of Merit

For all photodetetors, semiconductors are usually used as photosensitive materials at certain wavelength ranges, and a conductivity change is observed upon illumination with electromagnetic radiation. Several figures of merit are defined to evaluate the performance of photodetectors with different configurations [32-34].

Responsivity is the ratio of the generated photocurrent or photovoltage to the incident optical power. The expression is given in Equation 3.3, where η is the external quantum efficiency (the ratio of electrons extracted as current to the incident photons), q is the electron charge, λ is wavelength, h is Planck's constant, c is the speed of light, ω is the electrical modulation frequency, τ is the time constant, and G is the photoconductive gain.

$$R = \frac{\eta q \lambda}{hc} \frac{1}{\sqrt{1+\omega^2\tau^2}} G \tag{3.3}$$

In photodetectors, the output signal is usually not entirely due to photocurrent converted from incident power and is often accompanied by undesirable noise, including thermal noise, shot noise, and noise from the optical receivers. The signal-to-noise ratio (SNR) is thus an important parameter and is expressed in Equation 3.4, where P is the optical power incident on the detector and i_n is the noise current.

$$SNR = \frac{RP}{i_n} \tag{3.4}$$

Besides the above two criteria, another very important parameter is detectivity, expressed in Equation 3.5. Here, A is the detector area, and B is the electrical bandwidth. Detectivity is very useful since it is normalized to exclude the differences caused by device architectures and areas and can be used to directly compare performance due to material differences.

$$D = \frac{\sqrt{AB}R}{i_n} \tag{3.5}$$

3.3.2 Device Architectures

Device architectures of photodetectors are categorized into two main types, as shown in Figure 3.6. Photoconductors (Figure 3.6(a)) are composed of a semiconductor material sandwiched between two metal contacts [35]. After light is incident on the device, electron-hole pairs are generated which leads to increased carrier density and photoconductivity. In this structure, trap states are present in the absorbing materials which hinders the movement of one type of carrier and facilitates transport of the other. Photoconductors are therefore called single carrier type photodetectors. The lifetime of the carriers is enhanced in this way and they transverse through the device multiple times for a high gain and responsivity [36]. The disadvantage of using photoconductors is that they exhibit small bandwidth due to the long carrier lifetime.

The other type of photodetector architecture is the photodiode which is shown in Figure 3.6(b). The structure involves two materials, with at least one of them being a semiconductor. Depending on the specific type of the other material, a homojunction (two of the same type of semiconductor) [37], a heterojunction (two different types of semiconductors) [38], or a Schottky junction (a metal and a semiconductor) [39] is formed. Photodiodes are two-carrier-type photodetectors that use both electrons and holes to achieve responsivity. A built-in potential field acts to separate the electron-hole pairs which are extracted by their respective contacts. Photodiodes generally exhibit faster response times than photoconductive photodetectors, and longer depletion widths are highly desirable in these devices.

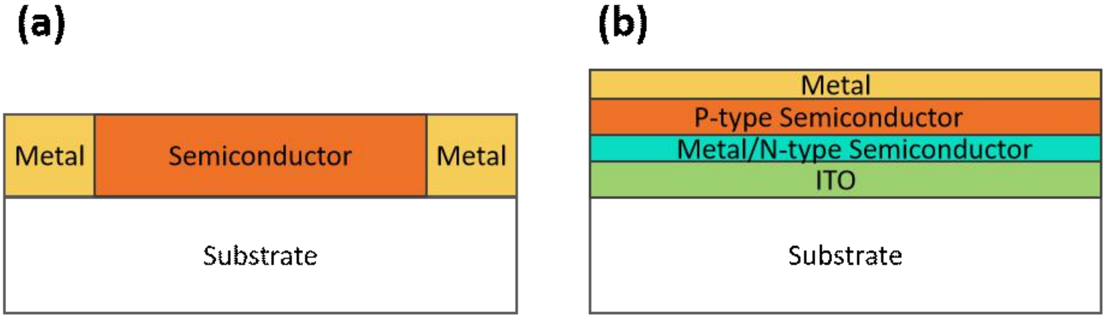

Figure 3.6 Schematic diagram showing photoconductor (a) and photodiode (b) architectures used in photodetectors.

3.3.3 Materials and Development

Crystalline silicon has been extensively developed as an absorbing material for photodetection in the visible regime [40,41]. Silicon photodetectors are mostly used in imaging applications (e.g. charged-coupled devices), and have also been employed in electronic integrated circuits due to compatible fabrication techniques. However, silicon has a low absorption coefficient in the visible and near-infrared range which limits its sensitivity, and it is not a suitable material for infrared detection. To overcome this shortcoming, amplification schemes such as silicon avalanche detectors are used to obtain excellent sensitivity while reducing material consumption.

Other classes of photodetectors have been developed to work in the infrared regime with practical applications in night vision and telecommunications, gas sensing, and medical imaging. In comparison to silicon, III-V direct band gap semiconductors (e.g. GaAs, InP or InGaAs-based materials) [42,43] have much higher absorption at 1-3 μm and therefore have been used to fabricate photodetectors for the short wavelength infrared. For the mid- (3-5 μm) and long (8-14 μm) wavelength infrared regions, HgCdTe and InSb are the two main types of materials that are dominant in the ecommercial market [44,45].

In recent years, solution-processed nanomaterials have been shown to exhibit the superior characteristics of low temperature processing, low cost, large area, ease of fabrication techniques, and compatibility with flexible substrates. Most importantly, their unique optoelectronic properties can be tailored for high responsivity and large bandwidth which show great potential for outperforming conventional photodetectors. Low dimensional semiconductors (0D, 1D, and 2D materials) have shown high absorption and gain, and photodetectors have been made from PbS-, CdS-, PbSe-, and graphene-based quantum dots, ZnO-, GaSb-, and Sb2Se3-based nanowires, and MoS_2- and WS_2-based nanosheets [46-50]. Further improvements are dependent on optimizing the chemical synthesis and functionalization for improved film quality and incorporating strong light interaction strategies such as plasmonic nanostructures and photonic crystals.

References

[1] Twilton, Jack, Patricia Zhang, Megan H. Shaw, Ryan W. Evans, and David WC MacMillan. "The merger of transition metal and photocatalysis." *Nature Reviews Chemistry* 1, no. 7 (2017): 1-19.

[2] Wang, Zheng, Can Li, and Kazunari Domen. "Recent developments in heterogeneous photocatalysts for solar-driven overall water splitting." *Chemical Society Reviews* 48, no. 7 (2019): 2109-2125.

[3] Ong, Chin Boon, Law Yong Ng, and Abdul Wahab Mohammad. "A review of ZnO nanoparticles as solar photocatalysts: synthesis, mechanisms and applications." *Renewable and Sustainable Energy Reviews* 81 (2018): 536-551.

[4] Lee, Gang-Juan, and Jerry J. Wu. "Recent developments in ZnS photocatalysts from synthesis to photocatalytic applications—A review." *Powder technology* 318 (2017): 8-22.

[5] Garg, Priyanka, Sourabh Kumar, Indrani Choudhuri, Arup Mahata, and Biswarup Pathak. "Hexagonal planar CdS monolayer sheet for visible light photocatalysis." *The Journal of Physical Chemistry C* 120, no. 13 (2016): 7052-7060.

[6] Schneider, Jenny, Masaya Matsuoka, Masato Takeuchi, Jinlong Zhang, Yu Horiuchi, Masakazu Anpo, and Detlef W. Bahnemann. "Understanding TiO2 photocatalysis: mechanisms and materials." *Chemical reviews* 114, no. 19 (2014): 9919-9986.

[7] Ameta, Rakshit, and Suresh C. Ameta. *Photocatalysis: principles and applications*. Crc Press, 2016.

[8] Linic, Suljo, Phillip Christopher, and David B. Ingram. "Plasmonic-metal nanostructures for efficient conversion of solar to chemical energy." *Nature materials* 10, no. 12 (2011): 911-921.

[9] Li, Jiangtian, Scott K. Cushing, Fanke Meng, Tess R. Senty, Alan D. Bristow, and Nianqiang Wu. "Plasmon-induced resonance energy transfer for solar energy conversion." *Nature Photonics* 9, no. 9 (2015): 601.

[10] Kowalska, Ewa, Orlando Omar Prieto Mahaney, Ryu Abe, and Bunsho Ohtani. "Visible-light-induced photocatalysis through surface plasmon excitation of gold on titania surfaces." *Physical Chemistry Chemical Physics* 12, no. 10 (2010): 2344-2355.

[11] Tsukamoto, Daijiro, Yasuhiro Shiraishi, Yoshitsune Sugano, Satoshi Ichikawa, Shunsuke Tanaka, and Takayuki Hirai. "Gold nanoparticles located at the interface of anatase/rutile TiO2 particles as active plasmonic photocatalysts for aerobic oxidation." *Journal of the American Chemical Society* 134, no. 14 (2012): 6309-6315.

[12] Ding, Dawei, Kai Liu, Shengnan He, Chuanbo Gao, and Yadong Yin. "Ligand-exchange assisted formation of Au/TiO2 schottky contact for visible-light photocatalysis." *Nano letters*14, no. 11 (2014): 6731-6736.

[13] Li, Benxia, Ting Gu, Tian Ming, Junxin Wang, Peng Wang, Jianfang Wang, and Jimmy C. Yu. "(Gold core)@(ceria shell) nanostructures for plasmon-enhanced catalytic reactions under visible light." *ACS nano* 8, no. 8 (2014): 8152-8162.

[14] Gusain, Abhay, Roberto M. Faria, and Paulo B. Miranda. "Polymer Solar Cells—Interfacial Processes Related to Performance Issues." *Frontiers in chemistry* 7 (2019).

[15] Kosyachenko, Leonid A., ed. *Solar Cells: Silicon Wafer-Based Technologies*. BoD–Books on Demand, 2011.

[16] McDonald SA, Konstantatos G, Shiguo Zhang, et al. Solutionprocessed PbS quantum dot infrared photodetectors and photovoltaics. Nat Mater 2005, 4, 138–42.

[17] Maria A, Cyr PW, Klem EJD, Levina L, Sargent EH. Solutionprocessed infrared photovoltaic devices with >10% monochromatic internal quantum eflciency. Appl Phys Lett 2005, 87, 213112.

[18] Koleilat GI, Levina L, Shukla H, et al. Eflcient, Stable Infrared Photovoltaics Based on Solution-Cast Colloidal Quantum Dots. ACS Nano 2008, 2, 833–40.

[19] Luther JM, Law M, Beard MC, et al. Schottky Solar Cells Based on Colloidal Nanocrystal Films. Nano Lett 2008, 8, 3488–92.

[20] Johnston KW, Pattantyus-Abraham AG, Clifford JP, et al. Schottky-quantum dot photovoltaics for eflcient infrared power conversion. Appl Phys Lett 2008, 92, 151115.

[21] Johnston KW, Pattantyus-Abraham AG, Clifford JP, et al. Eflcient Schottky-quantum-dot photovoltaics: The roles of depletion, drift, and diffusion. Appl Phys Lett 2008, 92, 122111.

[22] Debnath R, Tang J, Barkhouse DA, et al. Ambient-Processed Colloidal Quantum Dot Solar Cells via Individual PreEncapsulation of Nanoparticles. J Am Chem Soc 2010, 132, 5952–3.

[23] Piliego C, Protesescu L, Bisri SZ, Kovalenko MV, Loi MA. 5.2% eflcient PbS nanocrystal Schottky solar cells. Energy Environ Sci 2013, 6, 3054–9.

[24] Pattantyus-Abraham AG, Kramer IJ, Barkhouse AR, et al. Depleted-Heterojunction Colloidal Quantum Dot Solar Cells. ACS Nano 2010, 4, 3374–80.

[25] Willis SM, Cheng C, Assender HE, Watt AAR. The Transitional Heterojunction Behavior of PbS/ZnO Colloidal Quantum Dot Solar Cells. Nano Lett 2012, 12, 1522–6.

[26] Tang J, Liu H, Zhitomirsky D, et al. Quantum Junction Solar Cells. Nano Lett 2012, 12, 4889–94.

[27] Ning Z, Voznyy O, Pan J, et al. Air-stable n-type colloidal quantum dot solids. Nat Mater 2014, 13, 822–8.

[28] Voznyy O, Zhitomirsky D, Stadler P, Ning Z, Hoogland S, Sargent EH. A Charge-Orbital Balance Picture of Doping in Colloidal Quantum Dot Solids. ACS Nano 2012, 6, 8448–55.

[29] Liu H, Zhitomirsky D, Hoogland S, et al. Systematic optimization of quantum junction colloidal quantum dot solar cells. Appl Phys Lett 2012, 101, 151112.

[30] Stavrinadis A, Rath AK, de Arquer FPG, et al. Heterovalent cation substitutional doping for quantum dot homojunction solar cells. Nat Commun 2013, 4.

[31] Choi, Min-Jae, F. Pelayo García de Arquer, Andrew H. Proppe, Ali Seifitokaldani, Jongmin Choi, Junghwan Kim, Se-Woong Baek et al. "Cascade surface modification of colloidal quantum dot inks enables efficient bulk homojunction photovoltaics." Nature Communications 11, no. 1 (2020): 1-9.

[32] Zeng, Junpeng, Xiaoming Li, Ye Wu, Dandan Yang, Zhiguo Sun, Zehao Song, Hao Wang, and Haibo Zeng. "Space-Confined growth of CsPbBr3 film achieving photodetectors with high performance in all figures of merit." Advanced Functional Materials 28, no. 43 (2018): 1804394.

[33] Nalwa, Hari Singh, ed. Photodetectors and fiber optics. Elsevier, 2012.

[34] Zeng, Junpeng, Xiaoming Li, Ye Wu, Dandan Yang, Zhiguo Sun, Zehao Song, Hao Wang, and Haibo Zeng. "Space-Confined growth of CsPbBr3 film achieving photodetectors with high performance in all figures of merit." Advanced Functional Materials 28, no. 43 (2018): 1804394.

[35] Amani, Matin, Emma Regan, James Bullock, Geun Ho Ahn, and Ali Javey. "Mid-wave infrared photoconductors based on black phosphorus-arsenic alloys." ACS nano 11, no. 11 (2017): 11724-11731.

[36] De Iacovo, Andrea, Carlo Venettacci, Lorenzo Colace, Leonardo Scopa, and Sabrina Foglia. "High responsivity fire detectors based on PbS colloidal quantum dot photoconductors." IEEE Photonics Technology Letters 29, no. 9 (2017): 703-706.

[37] Xu, Yijun, Changlong Liu, Cheng Guo, Qiang Yu, Wanlong Guo, Wei Lu, Xiaoshuang Chen, Lin Wang, and Kai Zhang. "High performance near infrared photodetector based on in-plane black phosphorus pn homojunction." Nano Energy 70 (2020): 104518.

[38] Xiong, Da, Weili Deng, Guo Tian, Yuyu Gao, Xiang Chu, Cheng Yan, Long Jin, Yuhan Su, Wei Yan, and Weiqing Yang. "A piezo-phototronic enhanced serrate-structured ZnO-based heterojunction photodetector for optical communication." Nanoscale 11, no. 6 (2019): 3021-3027.

[39] Chang, Yu, Liang Chen, Jianyuan Wang, Wei Tian, Wei Zhai, and Bingbo Wei. "Self-Powered Broadband Schottky Junction Photodetector Based on a Single Selenium Microrod." The Journal of Physical Chemistry C 123, no. 34 (2019): 21244-21251.

[40] Desiatov, Boris, and Marko Lončar. "Silicon photodetector for integrated lithium niobate photonics." Applied Physics Letters115, no. 12 (2019): 121108.

[41] Qiu, Xiaodong, Xuegong Yu, Shuai Yuan, Yuhan Gao, Xuemei Liu, Yang Xu, and Deren Yang. "Trap assisted bulk silicon photodetector with high photoconductive gain, low noise, and fast response by Ag hyperdoping." Advanced Optical Materials 6, no. 3 (2018): 1700638.

[42] Wang, Wenjuan, Xiaomin Ren, Hui Huang, Xingyan Wang, Hailin Cui, Ang Miao, Yiqun Li, and Yongqing Huang. "Tunable photodetector based on GaAs/InP wafer bonding." IEEE electron device letters 27, no. 10 (2006): 827-829.

[43] Ejeckam, F. E., C. L. Chua, Z. H. Zhu, Y. H. Lo, M. Hong, and R. Bhat. "High-performance InGaAs photodetectors on Si and GaAs substrates." Applied physics letters 67, no. 26 (1995): 3936-3938.

[44] Tian, Zhongyun, Ruoxi Ji, Shengqiong Lei, and Boqi Gu. "Measurement of noise of photovoltaic HgCdTe and InSb infrared detector." In Detectors, Focal Plane Arrays, and Applications, vol. 2894, pp. 174-179. International Society for Optics and Photonics, 1996.

[45] Ning, Zhen-Dong, Shu-Man Liu, Shuai Luo, Fei Ren, Fengjiao Wang, Tao Yang, Feng-Qi Liu, Zhan-Guo Wang, and Lian-Cheng Zhao. "Growth and characterization of InAs/InAsSb superlattices by metal organic chemical vapor deposition for mid-wavelength infrared photodetectors." Materials Letters164 (2016): 213-216.

[46] Wu, Jianghong, Yanghua Lu, Sirui Feng, Zhiqian Wu, Shuyuan Lin, Zhenzhen Hao, Tianyi Yao, Xinming Li, Hongwei Zhu, and Shisheng Lin. "The Interaction between Quantum Dots and Graphene: The Applications in Graphene-Based Solar Cells and Photodetectors." Advanced Functional Materials 28, no. 50 (2018): 1804712.

[47] Ning, Yi, Zhiming Zhang, Feng Teng, and Xiaosheng Fang. "Novel transparent and self-powered UV photodetector based on crossed ZnO nanofiber array homojunction." Small 14, no. 13 (2018): 1703754.

[48] Xie, Ying, Bo Zhang, Shuxian Wang, Dong Wang, Aizhu Wang, Zeyan Wang, Haohai Yu et al. "Ultrabroadband MoS2 photodetector with spectral response from 445 to 2717 nm." Advanced Materials 29, no. 17 (2017): 1605972.

[49] Sun, Jiamin, Meng Peng, Yushuang Zhang, Lei Zhang, Rui Peng, Chengcheng Miao, Dong Liu et al. "Ultrahigh hole mobility of Sn-catalyzed GaSb nanowires for high speed infrared photodetectors." Nano letters 19, no. 9 (2019): 5920-5929.

[50] Zhao, Mei, Jianwei Su, Yang Zhao, Peng Luo, Fakun Wang, Wei Han, Yuan Li, Xiaotao Zu, Liang Qiao, and Tianyou Zhai. "Sodium-Mediated Epitaxial Growth of 2D Ultrathin Sb2Se3 Flakes for Broadband Photodetection." Advanced Functional Materials (2020): 1909849.

Chapter 4

Photophysical Studies of Solution-processed Aluminum Nanoparticles

4.1 Dynamics of Energy Transfer in Large Plasmonic Aluminum Nanoparticles

This section is adapted from Refence [1]. Reprinted with permission from ACS Photonics, Volume 5, Issue 3, Pages 805-813, "Dynamics of Energy Transfer in Large Plasmonic Aluminum Nanoparticles," by K. J. Smith, Y. Cheng, E. S. Arinze, N. E. Kim, A. E. Bragg, and S. M. Thon, copyright © 2017.

4.1.1 Introduction

Novel realizations of metal nanoparticles (NPs) are of continuing interest due to their unique optical properties and potential applications in optoelectronics, sensing, and catalysis [1-4]. Plasmonic materials have great appeal as harvesters of visible light, with plasmonic enhancement promising increased efficiency and spectral sensitivity of catalytic materials. In contrast to bulk metals, metal NPs exhibit localized surface plasmonic resonances (LSPRs) that are tunable via adjustment of particle size, shape, and composition as well as the properties of the surrounding environment. Methods for synthesizing, functionalizing, and manipulating gold and silver NPs are well established, and hence their photophysical properties, including narrow and tunable LSPRs across the visible and near-infrared (NIR) regions of the electromagnetic spectrum, are well characterized. However, large-scale deployment of precious-metal materials is impractical for many applications due to their high cost and relatively low earth abundance. Several alternatives have been proposed and synthesized, but there remains an urgent need to understand their photophysical properties, many of which differ nontrivially from gold and silver due to their unique electronic structures and complex dielectric constants.

Aluminum, in particular, is an inexpensive earth-abundant plasmonic material and a promising alternative to noble metals for applications requiring UV sensitivity and scalability. The plasmon resonance of bulk aluminum metal falls in the ultraviolet, but the LSPRs of aluminum NPs have been tuned successfully to the visible and NIR using size- and shape modulation [5-7] and are tunable over an even wider spectral range than those of Au or Ag. Aluminum also forms a native oxide layer at its surface in air that further red-shifts the LSPRs of particles. Unlike the interband transitions of gold (5d−6s) and silver (4d−5s), with threshold energies that overlap with the intraband plasmon resonance, the interband transitions of aluminum fall at 1.5 eV and do not overlap significantly with the intraband transitions [8]. Greater understanding of how these differences in electronic structure affect energy-transfer mechanisms is critical for developing optoelectronic and photocatalytic applications based on plasmonic aluminum [9,10].

The photophysical dynamics of noble-metal plasmonic nanomaterials have been characterized extensively with ultrafast transient absorption spectroscopy over the last two decades. Studies on relaxation dynamics of aluminum have been recently conducted on bulk films, nanorods, and nanodisks [11-14]. It is now well understood that interaction between a plasmonic NP and a femtosecond laser pulse creates a coherent electronic state (a "plasmon") that rapidly dephases (typically in 5−10 fs) to a highly nonthermal electron distribution. These "excited" nonequilibrium NPs subsequently relax through a sequence of energy-conversion and -transfer mechanisms beginning with thermalization via electron−electron (10−100 fs)and electron−lattice (~1−10 ps) scattering followed by lattice relaxation by intraparticle equilibration (10's of ps) and thermal energy transport to the surrounding environment (100's of ps to ns). The extensive body of work that has explored these processes has also led to an understanding of how energy transfer scales with NP dimensions [15] and shape [16] as well as particle composition [17] and interface properties [18]. Transient optical methods have also been used to demonstrate that hot electrons generated in noble-metal NPs are able to overcome an interfacial Schottky barrier when coupled to TiO_2, a common and robust semiconductor, thereby facilitating enhanced photocatalytic activity.

In this study, we report the first photophysical characterization of energy-transfer dynamics in large, solution-synthesized aluminum NPs. Time scales for spectral dynamics are similar to those ascribed for electron−electron, electron− photon, and lattice cooling temperatures for noble-metal particles, although we find that the spectral responses of Al NPs differ qualitatively. Notably, bleaching of the interband transitions is largely isolated from spectral changes associated with LSPR and provides a window into electron− electron thermalization dynamics. Furthermore, we find a ~250 ps energy transfer to the surrounding medium, comparable to energy-transfer rates for small (<10 nm in diameter) NPs, but much faster than predicted for the particle size studied (98 nm in diameter). To understand this phenomenon, we investigated thermal energy transfer dynamics using a two-interface model and find that rapid thermal energy transfer out of the Al core is mediated by the presence of the ~4 nm thick native oxide layer, pointing the way to using surface modifications as a tool to engineer heat-transfer rates in applications such as photocatalysis.

4.1.2 Synthesis and Optical Properties

We synthesized aluminum NPs using modifications of established procedures.56 Briefly, the particles were formed through decomposition of dimethylethylamine alane under mild heating using titanium(IV) isopropoxide as a catalyst. Morphologies of the synthesized aluminum NPs are shown in the transmission electron microscope (TEM) image in Figure 4.1(a). According to our analysis of the size distribution, the particles are relatively monodisperse with an average diameter of 98 ± 12 nm. The NP shapes are primarily icosahedra and truncated trigonal bipyramids. Figure 4.1(b) shows a high-resolution TEM image of a single aluminum NP taken using a FEI Talos S200 in which a thin oxide shell with an average thickness of approximately 3.7 ± 0.8nm is visible, consistent with previous observations.57 On the basis of the morphologies obtained from these images, we employed finite-difference time-domain (FDTD) simulations to predict the LSPR spatial field intensity distribution (Figure 4.1(c)) and spectrum (Figure 4.1(d)) of the aluminum NPs. The blue curve in Figure 4.1(d) shows the experimental extinction spectrum of the aluminum NPs in 2propanol measured by UV−vis spectrophotometry. The solution exhibited a clear broadband absorption peak due to the NP dipolar plasmon resonance with a maximum at 392 nm, as well as a peak at 269 nm associated with the quadrupolar plasmon resonance in both simulated and measured extinction spectra. We used FDTD simulations to calculate the extinction cross section of an icosahedral aluminum NP 93 nm in diameter with and without an aluminum oxide shell of 3.7 nm in thickness. The simulated peak extinction cross sections of the aluminum NPs without (red curve) and with (orange curve) an oxide layer are 389 and 393 nm, respectively; the latter matches well with that of the measured extinction peak, with the broadening of the peaks in the measured extinction spectra compared to the simulated ones attributed to the slight size inhomogeneity of the Al NP solution. We also observe that there is a broad shoulder, both in the measured and the calculated extinction spectra, between 800 and 900 nm that is clearer from plots of the first derivative shown in the inset of Figure 1D. This shoulder in the experimental spectrum falls at 815 nm and agrees well with the known spectral position of the parallel-band interband transitions in aluminum (~1.5 eV).21 Importantly, the extinction spectrum is dominated by particle scattering except in the region of the interband transition (vide infra).

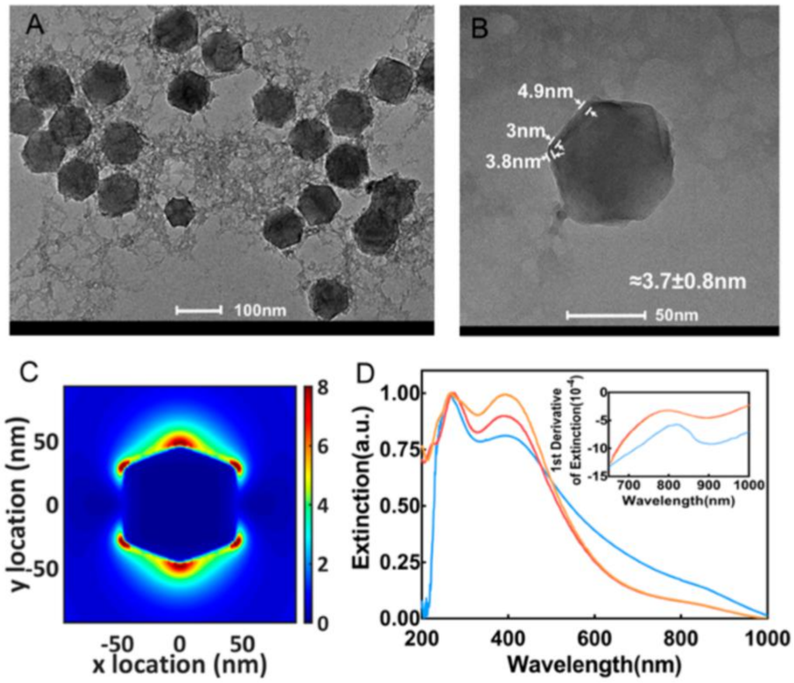

Figure 4.1 (a) TEM image of aluminum NPs. (b) Single aluminum particle surrounded by an oxide layer with an average thickness of 3.7 nm. (c) FDTD-calculated spatial electromagnetic field profile for a 93 nm diameter aluminum NP at the LSPR wavelength of 393 nm (color scale in arbitrary units). (d) UV−vis−NIR extinction (blue curve) of an aluminum NP solution in 2-propanol. FDTD-calculated extinction cross sections for a single bare aluminum icosahedron in a 2-proponal background (red curve) and an aluminum icosahedra with a 3.7 nm thick aluminum oxide shell (orange curve) in the same background. The inset shows the first derivative of measured (blue) and simulated (red/orange) extinction near the aluminum interband transition (1.5 eV).

4.1.3 Electron Relaxation Dynamics using Transient Absorption Spectra

Guided by this understanding of steady-state properties, we interrogated the photophysics of these particles suspended in 2-propanol with transient absorption spectroscopy.

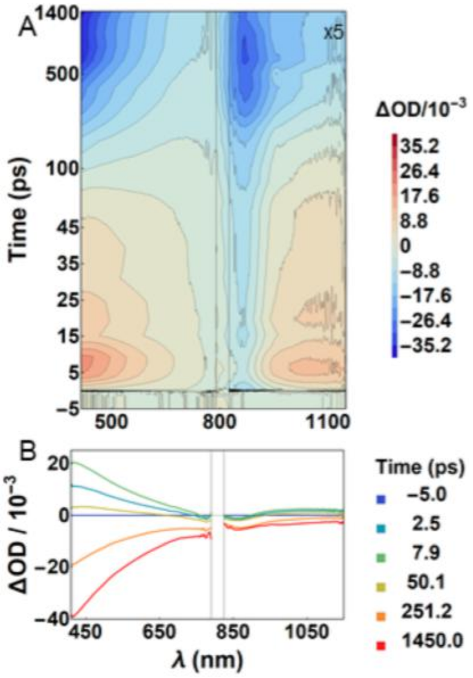

Figure 4.2 (a) Contour plot of transient spectra at 420−790 nm and 820−1150 nm after 400 nm excitation with a fluence of 134 μ J cm^{-2}. The time axis is linear from 0 to 50 ps and logarithmic from 50 to 1450 ps. Data in the NIR region are scaled by a factor of 5 for clarity. (b) Visible (left) and NIR (right) transient spectra at selected time delays of the same data sets (no scaling applied in NIR).

Figure 4.2 (a) presents a contour plot of time-dependent changes in optical density (i.e., extinction) from 420 to 1150 nm following interaction with ultrafast laser pulses at 400 nm (fluence of 134 μ m cm −2).“Time zero”can be identified by the sharp line near the bottom of the plot that is associated with ultrafast coherent interactions of the laser pulses with the sample solution that occur during the pulse cross correlation. Spectra collected at various time delays for each spectral region are plotted in Figure 4.2 (b). In total, Figure 4.2 demonstrates that changes in extinction occur broadly across the visible and NIR. Figure 4.3 plots temporal traces obtained by averaging over three different spectral regions: a region to the red of the LSPR peak (415−500 nm), near the aluminum interband transition (825−900 nm), and in the NIR beyond the interband transition (1000 – 1125 nm). Transient spectral dynamics can be summarized as follows: The spectral intensity near the interband transition bleaches immediately following excitation, whereas a slow induction to a positive △OD occurs broadly across the visible and beyond 900 nm, reaching a maximum positive value by 8 ps. At later time delays, the intensity of the broad positive signal modulates periodically with an overall decrease in amplitude, turning to a negative △OD on a time scale of a few hundred picoseconds. The time dependence of transient signals collected in the visible and longer-wavelength NIR are highly similar. Interestingly, despite the plasmon resonance having a maximum extinction at 392 nm, no extinction bleach is observed in this region immediately after excitation, which differs from studies conducted previously with noble-metal nanoparticles and aluminum nanodisks. A different temporal response is observed near the Al interband transition. Here the extinction drops rapidly to negative values within a few hundred femtoseconds after sample excitation (Figure 4.3, red symbols), a time scale slower than the experimental time resolution, but faster than the slow induction of extinction observed in other spectral regions. This negative dip arises from a "bleach" of the Al interband transition. At later delays, the bleach is overtaken by a broad negative extinction observed across the near-infrared. Numerous studies have demonstrated the effects of high fluence laser excitation on the photophysics of plasmonic NPs, and it is critical to rule these out before ascribing the time scales observed to specific energy-transfer processes. Nonlinear effects can include, but are not limited to, bubble formation by local solvent vaporization, persistent hole burning through particle ablation or melting, and multiphoton absorption.60 Notably, the broad spectral response we observe long after photoexcitation manifests as a reduction in optical density. In contrast, the formation of large vapor bubbles around photoexcited gold NPs has been shown to increase the probe extinction via increased Mie scattering; additionally, the threshold fluence for bubble formation (5.2 mJ cm^{-2} for 60 nm Au NPs) [19] is much higher (~ 100-fold) than what was used for our transient absorption studies (vide infra). To rule out contributions from laser-induced melting, we examined NP morphology using high-resolution TEM (HRTEM) imaging both before and after prolonged exposure to the 400 nm excitation source (4−6 h of irradiation with continuous sample mixing). The images reveal that there is no observable change in particle morphology. Additionally, there was no observable change in the steady-state absorption of the ensemble, indicating no changes in the particle properties with irradiation. Finally, spectral transients were collected at a series of laser excitation fluences. Together, these control experiments indicate that the spectral responses apparent reflect the intrinsic relaxation dynamics of the plasmonic particles in a linear excitation regime. As described in the introduction, the photoinduced responses of Au and Ag NPs involve at least four processes that impact their transient spectral dynamics: electron−electron thermalization (~100 fs), electron−phonon thermalization (~1 ps), and lattice relaxation dynamics, which include coherent phonon oscillations (~ few-10' s of ps period) and thermal energy transfer to the surrounding medium (10' s to 100' s of ps). The transient spectra of Al NPs evolve on qualitatively similar time scales as Au and Ag, although the transient spectra have somewhat different characteristics due to the weaker overlap between the intra- and interband transitions in Al and the fact that extinction associated with the Al intraband transition is dominated by the scattering cross section. The ultrafast induction in the interband bleach region is similar to behavior observed with Ag NPs in a glass matrix;36 this induction in the bleach is attributed to electron−electron thermalization that fills states above the Fermi level that serve as terminal states for the interband transition, such that the bleach of this transition increases with electronic relaxation. The rise in transient spectra broadly across the visible and NIR occurs in part due to particle lattice heating in response to LSPR excitation and subsequent electron thermalization. It also arises from modulation in the extinction coefficient due to phonon breathing modes activated by electron−lattice energy transfer. The signal induction can be seen quite clearly for Al NPs, as there is no overlap with the interband transition in the visible spectral region. Importantly, we expect that this signal will be dominated by modulation in scattering cross section; qualitatively, the rapid thermal expansion of the particle should increase the scattering cross section. The rapid photoinduced depletion of the interband transition in the NIR provides a direct signature of electron−electron thermalization within the material by which to clock the slow induction in electron-lattice thermalization and lattice heating. Finally, the slower inversion of the broad transient spectrum occurs on time scales consistent with thermal energy transport observed with noble-metal NPs. The optical response at the latest delays explored in our experiment (~1 ns) is characterized by a broadband negative signal that has been observed in silver and gold particles previously and has been attributed to thermal lensing64 or changes in the dielectric medium of the solvent. In the present study the possibility of thermal lensing was ruled out by varying the slit width of the spectrograph in order to confirm that 100% of transmitted light was observed on the detector. The dielectric constant of the solvent is expected to decrease as it heats up due to thermal energy transport. Previous studies that attributed negative extinction to changes in the dielectric of the solvent medium were conducted in water ($(\partial \varepsilon$ m $/ \partial T)_v = -6.2 \times 10^{-5}$ K^{-1}) [20]; in contrast, $(\partial \varepsilon / \partial T)_v \approx -0.15$ K^{-1} for 2-propanol [21]. The authors of the previous study observed this effect only at very high laser excitation fluences (>1 mJ cm^{-2}); although our experiments were conducted with comparatively lower pump fluences, the extremely high sensitivity of the 2-propanol dielectric constant to temperature variation explains this effect.

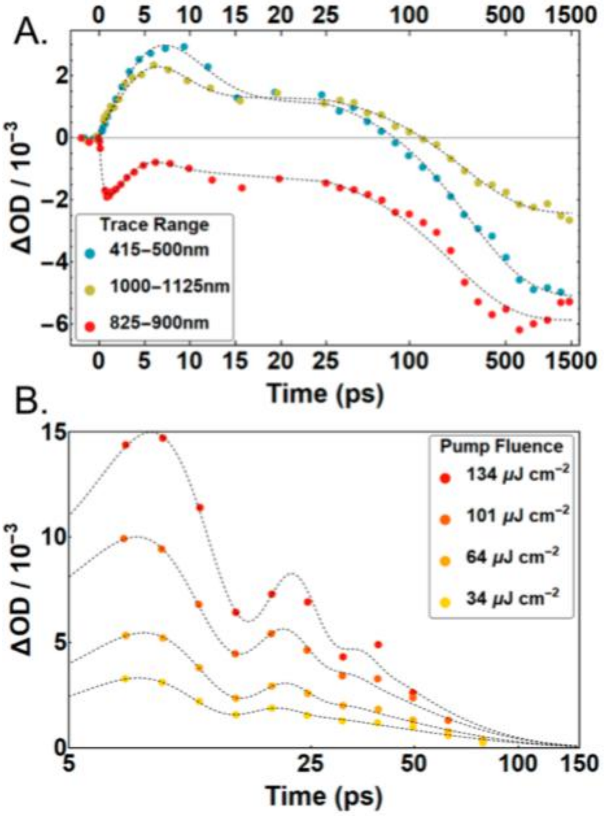

Figure 4.3 (a) Time-dependent traces obtained from three different spectral regions: near the LSPR peak (415−500 nm) (blue); off the LSPR peak in the NIR (1000−1125 nm) (gold); and in the interband transition region of metallic aluminum (825−900 nm) (red). Data from the visible region of the spectrum were scaled by a factor of 0.2 in order to display all three data sets in one plot. Fitting curves (described in the text) are displayed in black. (B) Fits to damped signal oscillations observed in the visible region at each of the excitation fluences used in this study.

In order to get a better handle on the time scales associated with these processes, we fit the traces plotted in Figure 4.3 (a) with various time-dependent functions. The signal intensity after lattice heating was modeled with exponential rise (τ_1) and decay (τ_2) as well as damped harmonic oscillations according to Equation 4.1.

$$I(t) = a_1(1 - e^{\frac{-t}{\tau_1}}) + a_2 e^{\frac{-t}{\tau_2}} + a_3 e^{-(\gamma t)^2} \cos(\frac{2\pi t}{\tau_R} + \varphi) + c \qquad (4.1)$$

Time scales obtained for all three regions are very similar and are listed in Table 4.1.

Table 4.1 Time Constants Obtained by Fitting Wavelength Dependent Transients with Equation 4.1.

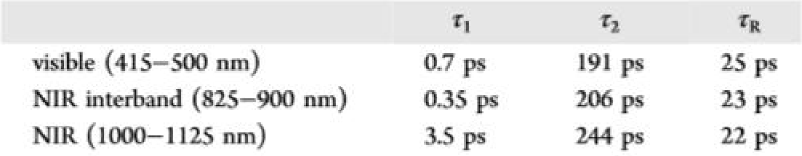

	τ_1	τ_2	τ_R
visible (415−500 nm)	0.7 ps	191 ps	25 ps
NIR interband (825−900 nm)	0.35 ps	206 ps	23 ps
NIR (1000−1125 nm)	3.5 ps	244 ps	22 ps

The intensity in the region of the interband transition of metallic aluminum (800−850 nm) exhibits a bleach signal that appears rapidly following the instrument response. This behavior is similar to that exhibited by noble metals while probing in the region of their respective interband transitions. As noted above, transient signals in the region of the interband transition also have contributions from the time-dependent spectral response of the particles observed at other wavelengths (i.e., scattering); this is clear from the very similar modulations in signal intensity on the picosecond to nanosecond time scales that occur with a clear offset in spectral intensity between the interband and 1000−1125 nm regions. The superposition of these signals makes it difficult to analyze the time dependence of the interband bleach feature alone. When the fit model (Equation 4.1) is applied to the region near the interband transition of aluminum, this reveals a bleach induction time, τ_{bleach}, of ~350 fs, which reflects the slowest phases of electron−electron thermalization. This time scale is slightly longer than the longest electron thermalization time scales observed in large Au and Ag NPs. As noted above, the signature of this bleach becomes less pronounced and is overtaken by the broad negative extinction spectrum at later delays, indicating that the bleach recovers as a consequence of thermal energy transfer out of the Al core. Although exact separation of the time-dependent scattering cross section and interband absorption is not possible, a crude analysis reveals that the interband transition partially recovers on a time scale commensurate with nanoparticle cooling. Based on precedent with noble-metal NPs, the slowest relaxation time scales observed in our measurements are assigned to thermal energy transport to the surrounding solvent environment. Various models for thermal energy transfer from nanoparticles to the surrounding media have been developed and applied. For example, Vallée and co-workers have applied thermal-transfer models to fit the time dependence of transient absorption measurements conducted with Au and Ag in solution and embedded in various glasses. These previous studies have investigated a large range of nanoparticle sizes (from about 5 to 133 nm in diameter). Their model involved a single interface between an NP and the surrounding medium to compute the temperature evolution of both the particle and the medium. Thermal dynamics in this model are governed by the interfacial thermal conductance (G) as well as the thermal conductivity (Λ) and heat capacity (c) of both the metal NP and surrounding medium. Whereas the bulk values of Λ and c are reasonable approximations for NPs, G is generally not known and is varied to fit the temporal behavior observed from optical measurements. Therefore, this line of investigation has also explored the impact of particle size and the chemical composition of interfaces on energy transfer.

4.1.4 Thermal Energy Transfer Mediated by Oxide Shell

We extended our analysis to a two-interface model to incorporate the native aluminum oxide layer on our particles. Table 4.2 gives a summary of parameters relevant for the aluminum NP/ aluminum oxide shell/2-propanol system.

Table 4.2 Heat Capacities and Thermal Conductivities of Aluminum, Aluminum Oxide, and 2-Propanol.

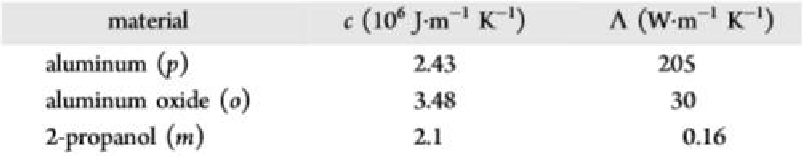

material	c (10^6 J·m^{-1} K^{-1})	Λ (W·m^{-1} K^{-1})
aluminum (p)	2.43	205
aluminum oxide (o)	3.48	30
2-propanol (m)	2.1	0.16

We used our model to explore the thermal dynamics in aluminum NPs with 93 nm diameters and 3.7 nm aluminum oxide shells suspended in 2-propanol. Our results are plotted in Figure 4A and indicate that heat dissipates much more quickly from the aluminum core when an oxide shell is present (blue dashed line) compared to the case without an oxide shell (blue solid line). Notably, the 1/e time scale for energy loss from the Al core from these simulations is ~300 ps when the oxide is present, in close agreement with the relaxation time scales observed in our experiments. Varying the free parameter G (thermal interface conductance) can control the rate of decay. The value used for the plot in Figure 4 was chosen from typical literature values for the thermal interfacial conductance of metal/metal oxide interfaces.Additionally, we predict that large Al NPs (93 nm in diameter) with an oxide layer possess thermal transport properties equivalent to those of much smaller particles (10 nm in diameter, solid blue line in Figure 4.4 (b)) with no oxide layer. These results indicate that the native oxide coverage on Al NPs likely provides an intrinsic protection against melting or ablation after interaction with a high-intensity laser pulse by facilitating fast and efficient thermal energy transfer to the surrounding solvent. We also found that the temperature evolution decay time scale (1/e) had little dependence on the oxide thickness, indicating that the addition of even a thin oxide shell could be a highly effective means for controlling the lattice temperature of plasmonic NPs. Previous work has demonstrated an increase in thermal energy transfer from Au NPs when encased by a silica shell. This work revealed a dependence on the silica shell thickness, but that the method of shell formation greatly impacted control of thermal energy transport because porous SiO_2 could allow penetration of solvent toward the Au core. In contrast, direct oxidation of the Al surface results in a compact native oxide layer that should prohibit formation of channels through which solvent can directly interface with the metal surface. Methods for replacing the native oxide layer on Al NPs in the solution phase have been demonstrated using fluoropolymer capping ligands and oxidizing salts (aluminum iodate hexahydrate). The thickness of the oxide layer could also be potentially tuned by introducing varied amounts of oxidizing agents.

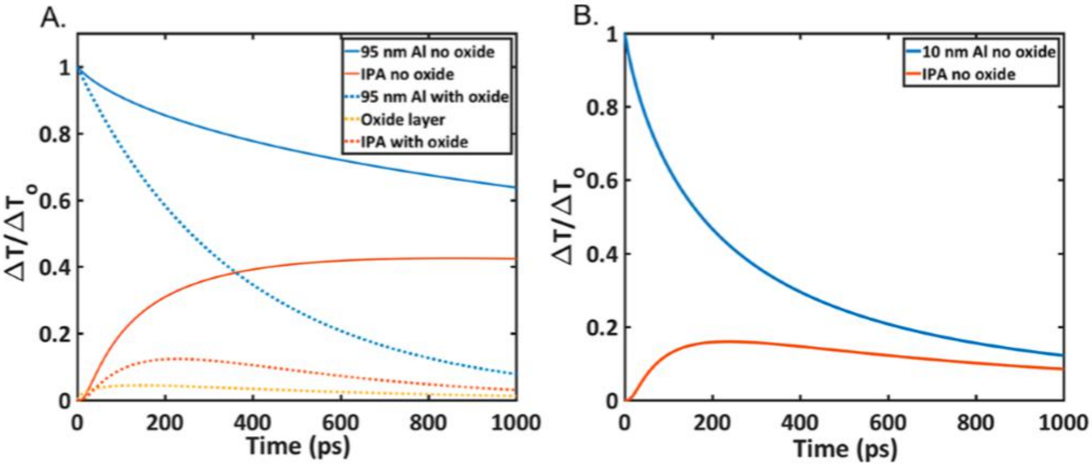

Figure 4.4. Simulations of thermal energy transport. (a) Temperature evolution relative to the initial temperature increase (ΔT_0) of the nanoparticle after optical excitation at the surface of a large (93 nm diameter) aluminum nanoparticle (solid blue line) and 3 nm into the surrounding 2-propanol (solid red line) for the case where no oxide is included, and where a thin oxide shell layer on the nanoparticle is incorporated into the model (blue and red dotted lines). The yellow dotted line corresponds to temperature evolution in the oxide layer. (b) Temperature evolution for a small (10 nm diameter) aluminum nanoparticle without an oxide layer. The thermal decay dynamics in this case roughly match those of the larger particle with an oxide shell.

4.1.5 Conclusion

We presented the first characterization of the photophysical dynamics of solution-synthesized plasmonic aluminum NPs, an emerging earth-abundant materials platform of interest for photocatalysis, optoelectronics, and sensing applications. We found that the response of large Al NPs differ qualitatively from noble-metal NPs: transient optical responses are dominated by evolution in scattering cross-section; furthermore, the optical response near the interband transition is dominated by evolution in absorption cross-section that are largely isolated from intraband transitions, allowing for study of electron−electron thermalization dynamics. We found that signal induction time scale match predictions for electron−lattice relaxation processes in related materials, and energy transfer to the surrounding medium from large particles is comparable to the energy-transfer rates predicted for much smaller particles. To understand this phenomenon, we investigated thermal energy transfer dynamics using a two-interface model to account for the presence of a native oxide layer on the aluminum NPs that mediates rapid thermal energy transfer out of the Al core. We propose that using surface modifications, including controlled oxidation, could be an effective tool to engineer heat-transfer rates from large particles to the surrounding medium and could be an important strategy for applications in which thermal management is critical for system performance and stability, including in photocatalytic and sensing applications.

References

[1] Smith, Kenneth J., Yan Cheng, Ebuka S. Arinze, Nicole E. Kim, Arthur E. Bragg, and Susanna M. Thon. "Dynamics of Energy Transfer in Large Plasmonic Aluminum Nanoparticles." ACS Photonics 5, no. 3 (2017): 805-813.

[2] Sau, T. K.; Rogach, A. L.; Jackel, F.; Klar, T. A.; Feldmann, J. Properties and Applications of Colloidal Nonspherical Noble Metal Nanoparticles. Adv. Mater. 2010, 22 (16), 1805−1825.

[3] Talapin, D. V.; Lee, J.-S.; Kovalenko, M. V.; Shevchenko, E. V. Prospects of Colloidal Nanocrystals for Electronic and Optoelectronic Applications. Chem. Rev. 2010, 110 (1), 389−458.

[4] Luo, X.; Morrin, A.; Killard, A. J.; Smyth, M. R. Application of Nanoparticles in Electrochemical Sensors and Biosensors. Electroanalysis 2006, 18 (4), 319−326.

[5] Knight, M. W.; King, N. S.; Liu, L.; Everitt, H. O.; Nordlander, P.; Halas, N. J. Aluminum for Plasmonics. ACS Nano 2014, 8 (1), 834−840.

[6] Chan, G. H.; Zhao, J.; Schatz, G. C.; Van Duyne, R. P. Localized Surface Plasmon Resonance Spectroscopy of Triangular Aluminum Nanoparticles. J. Phys. Chem. C 2008, 112 (36), 13958−13963.

[7] Lecarme, O.; Sun, Q.; Ueno, K.; Misawa, H. Robust and Versatile Light Absorption at Near-Infrared Wavelengths by Plasmonic Aluminum Nanorods. ACS Photonics 2014, 1 (6), 538−546.

[8] Ehrenreich, H.; Philipp, H. R.; Segall, B. Optical Properties of Aluminum. Phys. Rev. 1963, 132 (5), 1918−1928.

[9] Hao, Q.; Wang, C.; Huang, H.; Li, W.; Du, D.; Han, D.; Qiu, T.; Chu, P. K. Aluminum Plasmonic Photocatalysis. Sci. Rep. 2015, 5, 15288.

[10] Zhou, L.; Zhang, C.; McClain, M. J.; Manjavacas, A.; Krauter, C. M.; Tian, S.; Berg, F.; Everitt, H. O.; Carter, E. A.; Nordlander, P.; Halas, N. J. Aluminum Nanocrystals as a Plasmonic Photocatalyst for Hydrogen Dissociation. Nano Lett. 2016, 16 (2), 1478−1484.

[11] Rethfeld, B.; Kaiser, A.; Vicanek, M.; Simon, G. Ultrafast Dynamics of Nonequilibrium Electrons in Metals under Femtosecond Laser Irradiation. Phys. Rev. B: Condens. Matter Mater. Phys. 2002, 65 (21), 214303.

[12] Nie, S.; Wang, X.; Park, H.; Clinite, R.; Cao, J. Measurement of the Electronic Gruneisen Constant Using Femtosecond Electron Diffraction. Phys. Rev. Lett. 2006, 96 (2), 025901.

[13] Pomfret, M. B.; Brown, D. J.; Epshteyn, A.; Purdy, A. P.; Owrutsky, J. C. Electrochemical Template Deposition of Aluminum Nanorods Using Ionic Liquids. Chem. Mater. 2008, 20 (19), 5945− 5947.

[14] Su, M.-N.; Dongare, P. D.; Chakraborty, D.; Zhang, Y.; Yi, C.; Wen, F.; Chang, W.-S.; Nordlander, P.; Sader, J. E.; Halas, N. J.; Link, S. Optomechanics of Single Aluminum Nanodisks. Nano Lett. 2017, 17 (4), 2575−2583.

[15] Hu, M.; Hartland, G. V. Heat Dissipation for Au Particles in Aqueous Solution: Relaxation Time versus Size. J. Phys. Chem. B 2002, 106 (28), 7029−7033.

[16] Dowgiallo, A.-M.; Knappenberger, K. L. Ultrafast Electron− phonon Coupling in Hollow Gold Nanospheres. Phys. Chem. Chem. Phys. 2011, 13 (48), 21585.

[17] Ge, Z.; Cahill, D. G.; Braun, P. V. AuPd Metal Nanoparticles as Probes of Nanoscale Thermal Transport in Aqueous Solution. J. Phys. Chem. B 2004, 108 (49), 18870−18875.

[18] Hu, M.; Wang, X.; Hartland, G. V.; Salgueirino-Maceira, V.; Liz Marzan, L. M. Heat Dissipation in Gold−silica Core-Shell Nanoparticles. Chem. Phys. Lett. 2003, 372 (5), 767−772.

[19] Katayama, T.; Setoura, K.; Werner, D.; Miyasaka, H.; Hashimoto, S. Picosecond-to-Nanosecond Dynamics of Plasmonic Nanobubbles from Pump−Probe Spectral Measurements of Aqueous Colloidal Gold Nanoparticles. Langmuir 2014, 30 (31), 9504−9513.

[20] Hodak, J.; Martini, I.; Harland, G. Spectroscopy and Dynamics of Nanometer-Sized Noble Metal Particles. J. Phys. Chem. B 1998, 102 (36), 6958−6967.

[21] Haynes, W. M., Ed. CRC Handbook of Chemistry and Physics, 95th ed.; CRC Press: Oakville, 2014.

4.2 Size- and Surface-Dependent Photoresponses of Solution-Processed Aluminum Nanoparticles

This section is adapted from Reference [1]. Reprinted with permission from ACS Photonics doi.org/10.1021/acsphotonics.9b01170, "Size and surface-dependent photoresponses of solution-processed aluminum nanoparticles." by Yan Cheng, Kenneth J. Smith, Ebuka S. Arinze, Rachel Dziatko, Tina Gao, Benjamin P. Frank, Susanna M. Thon, and Arthur E. Bragg., copyright © 2020.

4.2.1 Introduction

Plasmonic nanomaterials continue to attract considerable interest for novel applications in optoelectronics, sensing, and catalysis that take advantage of the concentration of electromagnetic fields of light or the electronic excitation associated with localized surface plasmon resonances (LSPRs) [1-6]. There is particular interest in using plasmonic nanoparticles (NPs) as sensitizers for photocatalysis [7,8]. Specifically, it has been demonstrated that hot electrons in plasmonic NPs originating from optical LSPR excitation can overcome the Schottky barrier with an adjoining material to generate reactive conduction-band electrons for catalysis [9,10] with an efficiency that depends on the electronic and thermal relaxation dynamics of the NP. The photothermal properties of plasmonic NPs are also of great interest for their use in applications such as plasmonic photothermal therapies [11,12]. The finite thermal conductivity of metal NPs allows them to be utilized as extremely efficient heat sources through far-field illumination [13]. Optically resonant excitation of the LSPR results in localized heating around the particle with large temperature gradients. Not only can this thermal energy be used to destroy biological tissue (e.g., cancer cells)

[14.15], but also these temperature gradients have been used experimentally to direct the motion of nearby objects through thermophoretic forces [16,17]. The impacts of material architecture, interfaces, and the chemical environment on electronic and lattice-energy dissipation pathways are critical to the efficacy of these applications.

The LSPR underlying the photoresponses of these materials is a coherent collective response of carriers (i.e., electrons) to electromagnetic radiation that is tunable according to particle size, shape, and composition. Noble-metal particles such as gold and silver have been extensively studied over the years both in efforts to elucidate the fundamental properties of plasmonic nanomaterials and in the development of optical applications. However, the large-scale deployment of materials, devices, or chemical applications based on precious metals has the potential to be costly and also limited by the relatively low elemental abundance of precious metals. In recent years, aluminum has emerged as an inexpensive, earthabundant alternative to noble metals for plasmonic nanomaterials, yet much less is known about the plasmonic responses of Al nanomaterials, including the impact of native oxides on their photothermal and photoacoustic behaviors as well as their charge-transfer potential for catalytic sensitization. A firm understanding of the photophysical properties of these particles and how they vary with size, shape, and chemical environment is essential for the development of Al-based plasmonic material applications.

There are currently few published studies of the photophysical properties of plasmonic Al nanomaterials in the literature. Su et al. have investigated the electronic relaxation behaviors of single Al nanodisks [18,19]. Because of the polycrystalline nature of the Al nanodisks, fast (subpicosecond) electron−phonon relaxation time scales were observed, and damping of phonon vibrations was found to be largely determined by the presence of intrinsic lattice defects and rough surfaces, with minimal dependence on the substrate environment. The oxide shell was identified as providing an interface with the Al core that trapped and detrapped carriers, with the potential to enable long hot-carrier lifetimes. We recently reported on the photothermal-energytransfer dynamics of a different Al nanomaterial: solutionprocessed, single-crystal Al NPs (~100 nm diameter) suspended in 2-propanol (IPA). We observed a broad, rapid (subpicosecond to picosecond) decrease in probe light transmission across the visible and near-IR regions following sample excitation at 400 nm, which we attributed to a combination of electron−phonon energy transfer followed by changes in the scattering cross-section of particles as a result of electron-to-phonon energy transfer and lattice expansion. Periodic modulation in probe transmission across the visible and near-IR regions associated with coherent phonon/acoustic vibrations was resolved with a period of ~14 ps. This was followed by a slow increase in light transmission observed on a time scale of ~ 250 ps, ultimately leading to a net increase in light transmission by 1 ns that we attributed to a decrease in the surrounding solvent dielectric constant due to thermal energy transfer from the Al particle. The latter assignment was supported by simulations of thermal energy transfer: A simple two-interface (Al/Al oxide/solvent) model revealed that the fast local heating of the solvent is facilitated by the intermediary aluminum oxide, which quickly and efficiently mediates thermal energy transfer from the Al core to the surrounding medium. Indeed, from the model, it can be seen that oxide-coated particles cool on time scales that are roughly an order of magnitude faster than those of particles without an oxide layer; for example, a 100nm particle with an oxide layer will cool on a comparable time scale as that of a 10 nm particle without an oxide layer.

Here we present an extended study of Al NPs to investigate in more detail the impacts of both the particle size and the surface composition on their photothermal properties. In particular, we examine the size dependence of the frequencies and damping rates for the acoustic phonon vibrations that are activated by lattice expansion [20]. These high-frequency acoustic vibrations can be measured using techniques including transient absorption (TA) spectroscopy (as conducted in our work) and Raman scattering spectroscopy. The damped oscillations in time-dependent signals are sensitive not only to the mechanical properties of the plasmonic particles but also to how these resonators interact with the surrounding environment. There is considerable precedent in the literature regarding this sensitivity: Studies of the acoustic properties of alloyed and core−shell multicompositional metal NPs have revealed that both the composition and mechanical interfaces are important factors that inflfluence energy transfer. The vibrational mode frequencies of metal−dielectric core−shell particles have been found to be strongly affected by their amorphous oxide shells. Additionally, surface ligands affect the mechanical coupling between the metal, dielectric, and the surrounding solvent; this has been demonstrated in recent studies on core−shell [21-23] semiconductor quantum dots in which an accurate interpretation of the vibrational resonances is obtained by including the capping ligands in an elastic continuum model [24]. Inhomogeneous broadening in NP solutions can also accelerate the ensemble decay dynamics. Thus the specific structure, composition, and surface functionalization of plasmonic NPs are all important factors that dictate the details of their energy-dissipation dynamics.

4.2.2 Synthesis, Size distribution, and Surface Characterizations

Colloidal Al NPs were synthesized using solution-processed methods based on modifications to published procedures; details are provided in the Methods section. By delaying the addition time of the capping agent, we were able to controllably tune the size of the particles. We prepared four samples with varied particle dimensions in our study and verified their sizes using transmission electron microscopy (TEM), as shown in Figure 4.5(a)−(d).

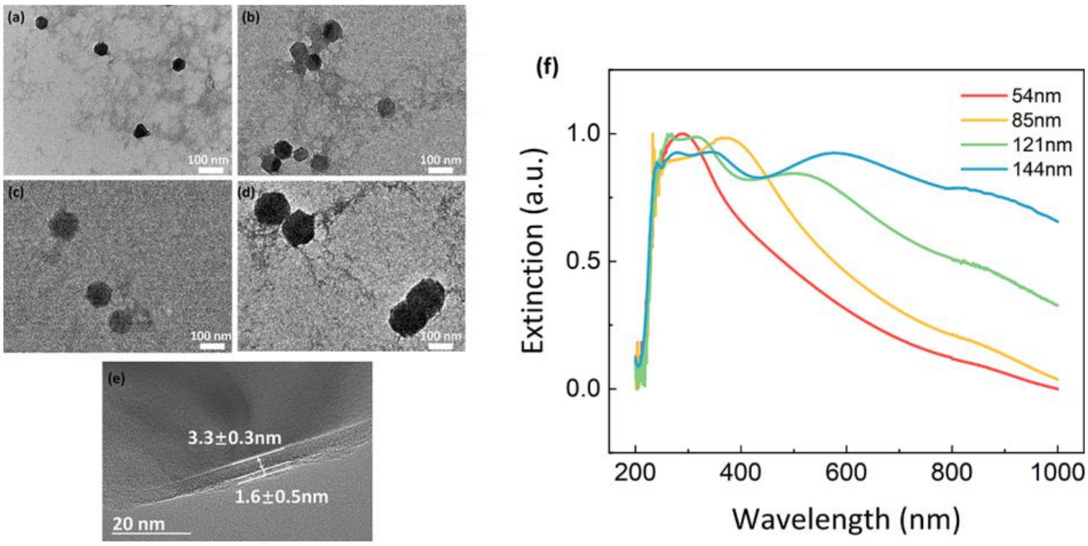

Figure 4.5 (a−d) TEM images of Al NPs with mean diameters of 54, 85, 121, and 144 nm. (e) High-resolution TEM image showing both the surface oxide (thickness of 3.3 ± 0.3 nm) and the organic ligand shell (thickness of 1.6 ± 0.5 nm) on an Al NP. (f) UV−vis−NIR spectrophotometric extinction spectra for Al NP solutions with these four difffferent mean diameters, as indicated in the legend.

The majority of the particles exhibit icosahedral shapes, and the four samples we studied have average particle diameters of approximately 54, 85, 121, and 144 nm. High resolution TEM images, shown in Figure 4.5 (e) and in Figure 4.6, indicate the presence of an oxide layer (thickness of 3.3 ± 0.3 nm) and an organic ligand layer (thickness of 1.6 ± 0.5 nm) on the surface of the Al particles, as expected from the synthesis procedure and previous work on similar particles.

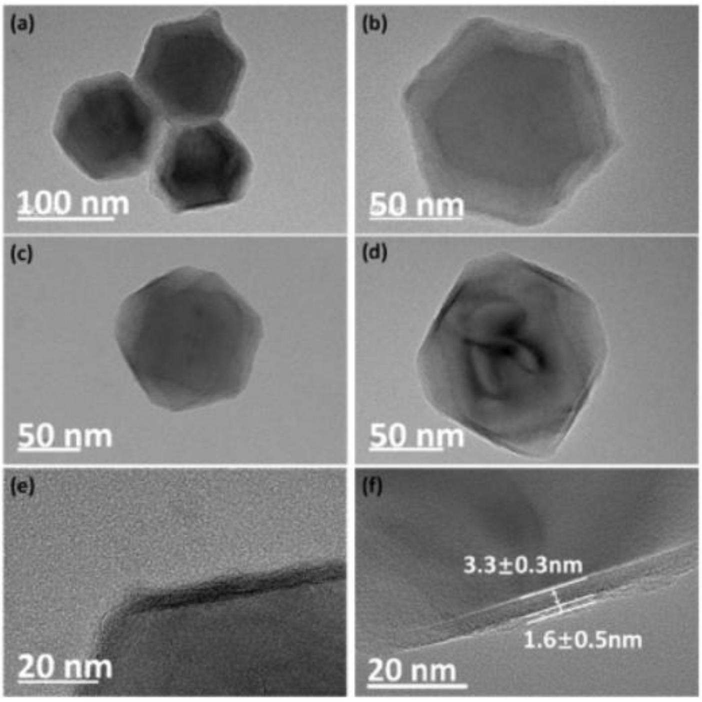

Figure 4.6 (a)-(f) Additional high resolution transmission electron microscopy (HRTEM) images of Al NPs. The oxide and organic ligand shells are visible in all images, although their thickness is obscured by faceting in (a)-(c). A thickness measurement is displayed in (f). Further characterization of oxide thickness and ligand surface coverage is provided below.

Our assignment of structures apparent in the TEM images is substantiated by a collection of surface characterizations: X-ray photoelectron spectroscopy (XPS) of Al0/Al3+ 2p states (Figure 4.7 (a)) confirms the existence and the chemical composition of an Al/Al2O3 core/shell structure and reveals a 3.1 nm ±10% oxide-shell thickness. XPS (C 1s, Figure 4.7 (b)), Fourier transform infrared (FTIR, Figure 4.8) spectroscopy, nuclear magnetic resonance (NMR, Figures 4.9 and 4.10) spectroscopy, and thermogravimetric analysis (TGA) (Figure 4.11) provide clear chemical signatures indicating that only an oleate ligand is bound to the surface and at relatively high surface coverages (~5 molecules/nm^2). X-ray photoelectron spectroscopy (XPS) measurements were conducted on the Al NPs to investigate the their composition (Figure 4.7). The Al 2p spectra shown in Figure 4.7 (a) clearly contain features associated with both Al (Al^0) and Al oxide (Al^{3+}) at binding energies of 72.7eV and 75.1eV, respectively. Sputtering of the sample was conducted to confirm a metallic Al core existed. As the sputtering time increases, the relative intensity of the Al^0 peak increases, corresponding to the removal of the oxide layer. The oxide layer thickness was calculated to be approximately 3.1±10% nm using established methods, consistent with that estimated from the HRTEM measurement in Figure 4.6 (f). XPS spectra collected in the C 1s region (Figure 4.7(b)) of the Al NPs prior to sputtering reveal a small shoulder (next to a dominant peak) whose peak position (289 eV) is consistent with a carboxylate group. The 5.3% intensity ratio between this shoulder and the dominant C 1s feature is consistent stoichiometrically with surface-bound oleate ($C_{17}H_{33}COO$) and the absence of any other organics at the surface.

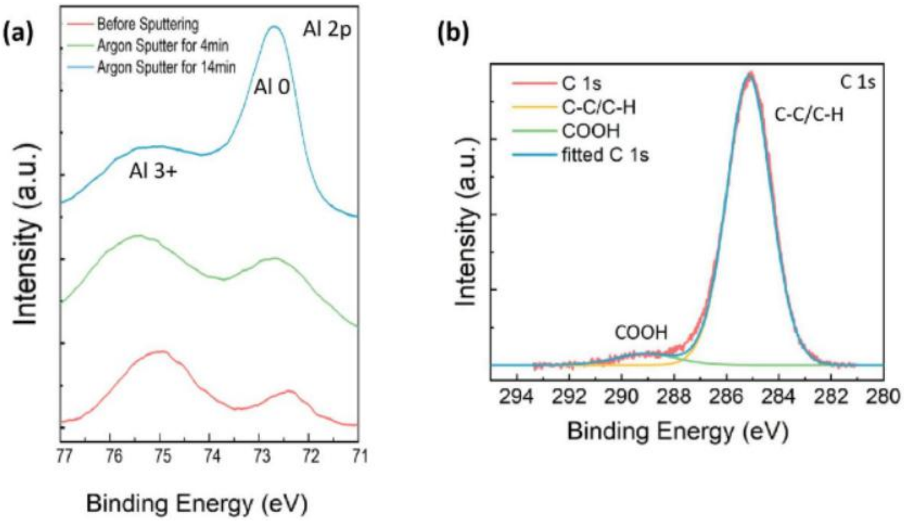

Figure 4.7: X-ray photoelectron spectroscopy (XPS) measurements of (a) the Al^0 2p and Al^{3+} 2p levels before and after argon sputtering of the surface as indicated in the legend and (b) the C 1s region (red) of the Al NPs prior to sputtering and fits (yellow, green, blue) as indicated in the legend. The presence of the Al3+2p peak in the XPS spectrum indicates the presence of an oxide shell on the Al NPs, and the thickness of the shell was determined to be 3.1±10% nm as described in the text below. The intensity ratio between the carboxylate-associated shoulder in (b) and the aliphatic C 1s feature is consistent with surface-bound oleate.

We also utilized Fourier transform infrared (FTIR) spectroscopy and nuclear magnetic resonance (1H NMR) measurements to further characterize the chemicalstate of the oleic acid/oleate ligand (i.e. bound or unbound carboxylate).

FTIR spectra obtained with our oleate-capped aluminum nanoparticles as well as free oleic acid are shown in Figure 4.8. The FTIR spectra indicate modifications to stretching vibrations consistent with the oleate being bound to the surface of the aluminum nanoparticles: the spectrum of the nanoparticles shows two peaks for the CH_2 symmetric and asymmetric stretches of oleate that are slightly lower in energy relative to the free oleic acid stretches, as has been observed previously for surface bound oleate ligands. More significantly, the strong C=O stretching feature observed for free oleic acid at 1707 cm^{-1} does not appear in spectra measured with our Al nanoparticles; instead, we observe two broad features at lower frequencies (1588 and 1412 cm^{-1}) that correspond with the COO-symmetric and asymmetric stretches of oleate bound to the nanoparticle sample, as has been observed previously. Table 4.3 summarizes the frequencies for these features.

Table 4.3 Critical FTIR peak assignments.

	CH_2 Symmetric Stretch	CH_2 Asymmetric Stretch	C=O stretch	COO- Symmetric Stretch	COO- Asymmetric Stretch
Oleic Acid	2852 cm^{-1}	2922 cm^{-1}	1707 cm^{-1}	N/A	N/A
Al NP	2850 cm^{-1}	2917 cm^{-1}	N/A	1412 cm^{-1}	1588 cm^{-1}

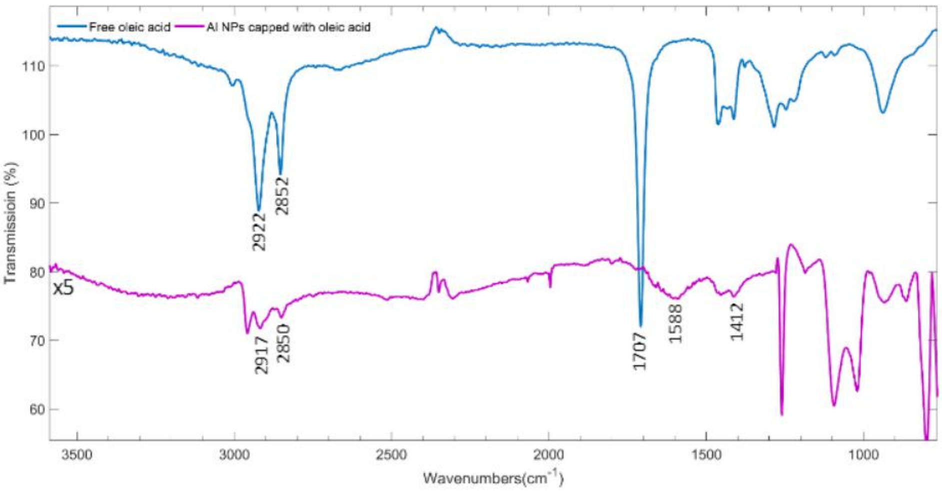

Figure 4.8 FTIR spectra of free oleic acid (blue) and oleate-capped aluminum nanoparticles (pink) cast from IPA, multiplied by 5 and offset for comparison of vibrational features.

1H NMR spectra were collected for ligand-capped aluminum nanoparticles and free oleic acid suspended/dissolved in deuterated chloroform. Full spectra for each sample are presented in Figure 4.9. Figure 4.10 (a) provides labels for hydrogen sites; Figures 4.10 (b-d) illustrate spectral differences for free vs. particle-bound oleate for specific hydrogen sites. The spectrum of the nanoparticles shows characteristic peaks of oleate bound to the surface of nanoparticles. The peaks for hydrogens “e” and “f” are the most resolved but are broadened and are shifted slightly downfield (Figure 4.10 (b)), a trend previously observed in the literature. The peaks associated with hydrogens closer to the surface-bound carboxylate group (e.g. the “a” and “c” sites around the carbon double bond, Figures 4.10 (c-d)) are also broadened and either barely visible or not present due to their proximity to the nanoparticles, which rotate slowly on the timescale of the measurement. Table 4.3 summarizes the positions of features from NMR spectra.

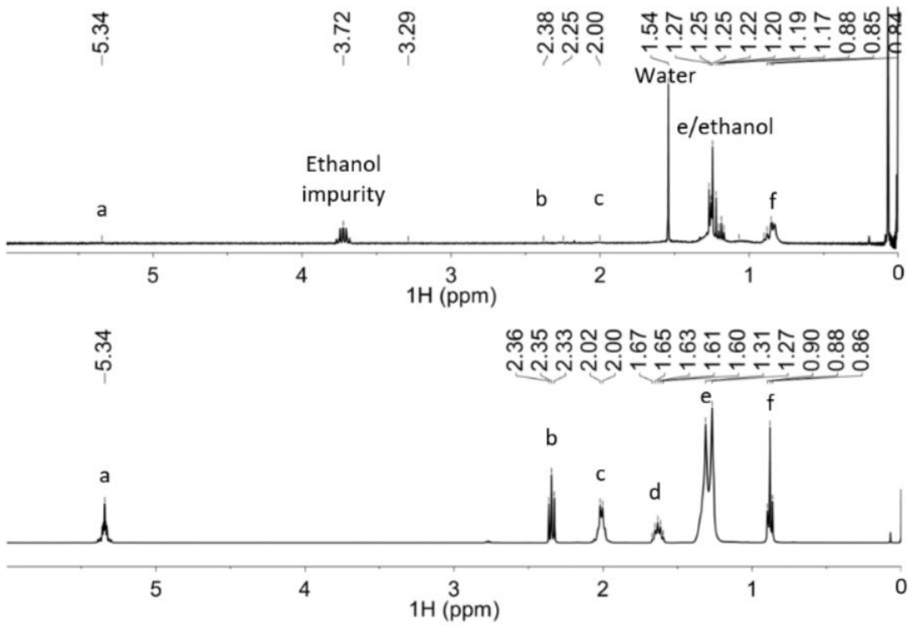

Figure 4.9 Full 1H NMR of (a) aluminum nanoparticles capped with oleate ligand and (b) free oleic acid with peak assignments (c.f. Figure 4.6 (a)).

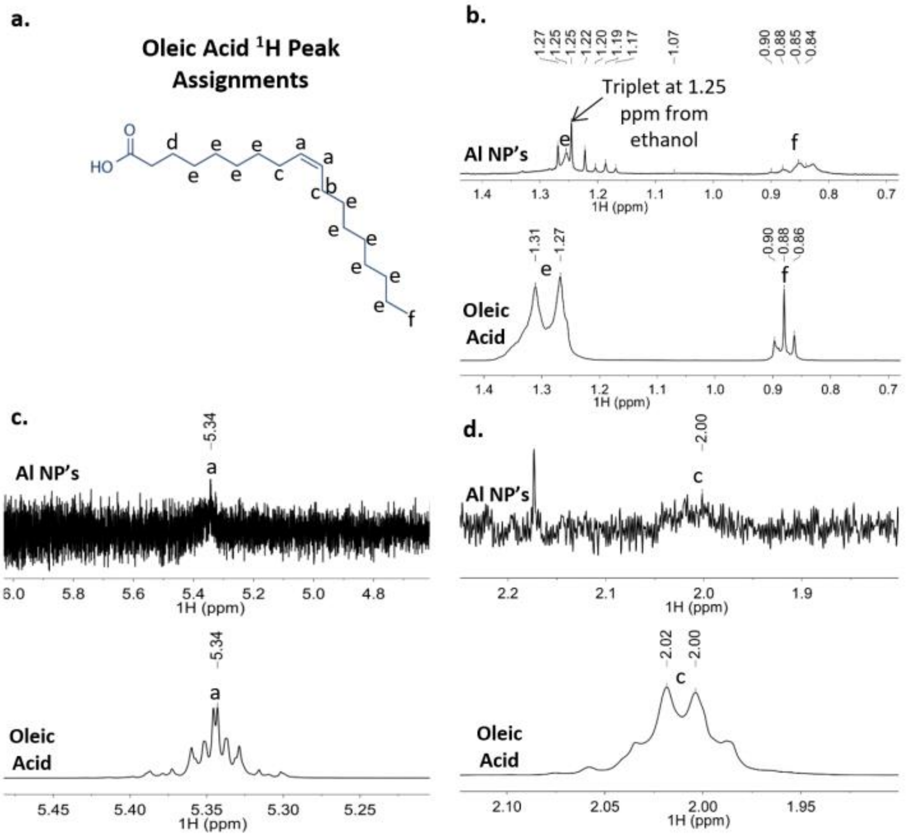

Figure 4.10 (a) Structure of oleic acid with 1 H peak assignments and (b, c, d) highlighted regions of aluminum nanoparticle and free oleic acid 1 H NMR spectra.

4.2.3 Size-dependent Transient Absorption Spectra

We used UV−vis−NIR spectrophotometry to measure the extinction spectra of the four particle samples in IPA. The particles show tunable dipolar LSPR peaks with wavelengths that range from 288 to 577 nm as the particle size increases (Figure 4.1 (f)). Higher order modes also appear in the spectra at wavelengths below 400 nm with increasing particle size. The broad shoulder in all spectra near 850 nm in wavelength corresponds to the aluminum interband transition. Figure 4.7 (a) and (b) presents contour plots of transient absorption spectra collected for 54 and 144 nm Al NPs, respectively, excited near the peak of their plasmon resonances (specifically, 400 nm excitation for 54, 85, and 121 nm particles and 580 nm excitation for 144 nm particles). Here positive absorption (shaded red) corresponds to decreased probe light transmission, whereas a negative signal (shaded blue) corresponds to increased probe transmission. Time delays are reported along a split linear/log axis to highlight the spectral dynamics across all relevant time scales; time zero is clear from the sharp coherent, nonlinear pulse interaction with IPA (which appears as a dark line in Figure 4.7 (a) and (b)) that occurs prior to signal induction. The time-dependent spectral evolution observed with the particle ensembles of different sizes are qualitatively similar to what we have previously observed with ~100 nm diameter particles: In all cases, a slow induction to a positive ΔOD (i.e., a decreased probe light transmission) occurs at wavelengths >950 nm, peaking between 5 and 15 ps after excitation. This positive signal decays to ΔOD = 0 by ~100−150 ps and continues to decay to a negative value (i.e., increased light transmission) within a nanosecond. We have previously assigned the initial positive ΔOD increase to an enhanced scattering cross-section due to lattice expansion that follows electron-to-phonon energy transfer; in contrast, the increased light transmission (ΔOD < 0) observed at 1 ns is attributed to a change in the solvent refractive index due to local heating that alters both the scattering and the absorption cross sections of the NPs, as previously modeled with finite-difference time domain (FDTD) simulations. For larger particles, we observe a rapid bleach near the aluminum interband electron transition that peaks at <900 nm in wavelength; similar behavior was observed for 100 nm particles studied previously.

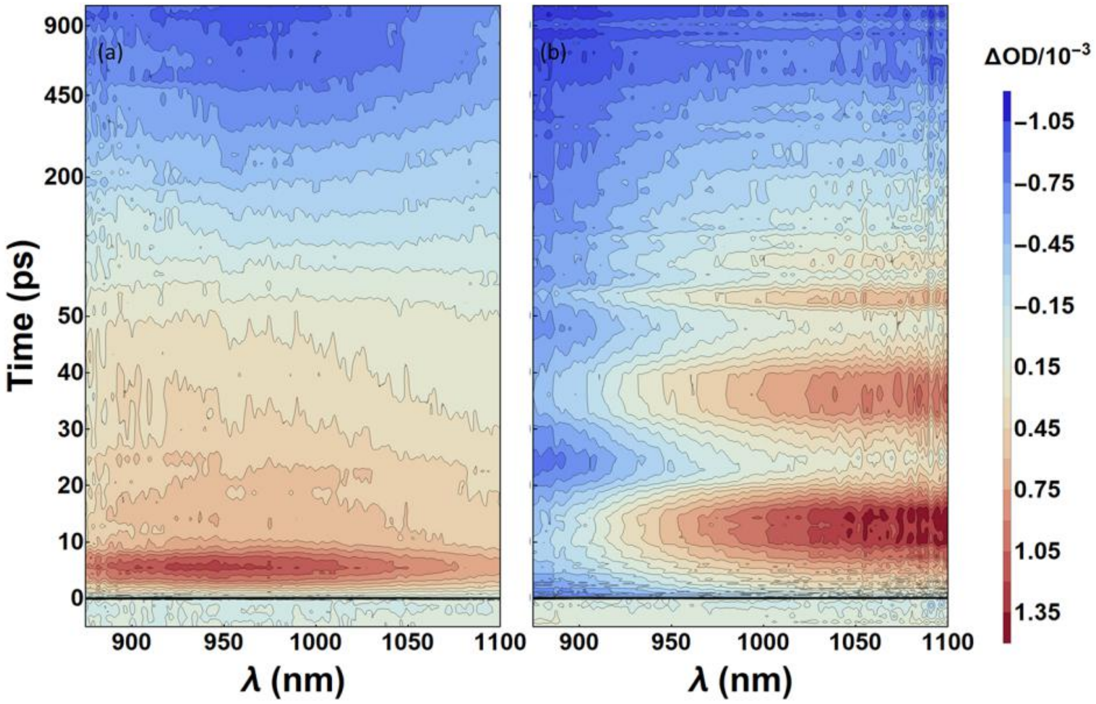

Figure 4.11 Contour plots of transient spectra (plotted in terms of the change in optical density, △OD) collected for particles with (a) ~54 and (b) ~144 nm diameters. Transients are plotted on a split linear−log time scale to highlight the spectral evolution on time scales up to ~1 ns after excitation. The contour for the smallest particles is scaled by 0.25 for comparison.

Although the changes in optical transmission with probe delay remain qualitatively similar across all sizes studied, it is clear from Figure 4.7 that the presence of signal modulations associated with acoustic lattice modes (i.e., coherent phonon vibrations), which are initiated by rapid electron-to-phonon energy transfer, is highly dependent on the particle sample. For example, whereas a highly recurrent oscillatory response is observed after excitation of the 144 nm particles (Figure 4.7

(b)), vibrations associated with the 54 nm particles are strongly damped (Figure 4.7(a)). Whereas data for each of the samples were collected out to 1 ns to track the dynamics of the photothermal energy transfer from the NP to the solvent, data sets containing a higher number of time delays through 100 ps were also collected to carefully characterize the time dependence of these phonon vibrations. Figure 4.11 (a) plots the time dependence of transient cuts through the near-IR absorption for all particle sizes studied, illustrating the differences in acoustic particle vibrations with size in terms of both phonon frequency and overall damping. For the larger particles studied (~121 and 144 nm), signal oscillations recur repeatedly through the first 100 ps that follow excitation. In samples of particles that have a diameter of 100 nm or smaller, the vibrations are apparent but are highly damped. Finally, as seen in Figures 4.11 and 4.12 (a), the time delay at which the signal peaks (i.e., when the transmission is minimized) increases monotonically with particle size. The functional form used to fit the traces from the TA data plotted in Figure 4.12 (a) is given in Equation 4.2.

$$I(t) = a_r(1 - e^{\frac{-t}{\tau_r}}) + a_p e^{\frac{-t}{T1}} e^{\frac{-t^2}{(T_2^*)^2}} \cos(\frac{2\pi t}{\tau_p} + p) + a_d e^{\frac{-t}{\tau_d}} + c \qquad (4.2)$$

The fitting function parameters include an initial increase in the cross section (induction time τ_r), a damped periodic signal oscillation with period τp and phase p, oscillation damping with both homogeneous (T_1) and inhomogeneous (T_2*) contributions, a slow cross-section decay (lifetime τ_d), and corresponding scaling constants (a_r, a_d, and a_p) as well as a constant offset (c) that accounts for the reversal in light transmission arising from changes in the local solvent dielectric (or refractive index) due to thermal energy transfer from the NP to the surrounding solvent on longer time scales. The thermalization lifetime, τ_d, could not be reliably determined from data sets extending only to 100 ps, the duration most useful for accurately determining the periods of the acoustic vibrations. To more accurately the find the thermal decay time scales, data collected on longer time scales (up to 1 ns, but after oscillations have ceased) were fit to a single exponential decay, as shown in Figure 3b. Thus, in total, the time scales for the evolution of TA signals were determined as follows: The signal decay on longer time delays attribufto thermal energy transfer from the NP to the solvent was fit separately to a single exponential decay (Figure 3b, dashed lines). Time constants extracted from these fits were found to be τd = 173, 243, 244, and 284 ps for the 54, 85, 121, and 144 nm particles, respectively. The remaining fit parameters (τr, τp, p, T_1, and signal amplitudes) were adjusted for best fifit to the signal oscillations seen in Figure 3a. Notably, although T_2* is listed as a variable parameter in Equation 4.2, for statistical particle size distributions, it is related to the oscillation period as

$$T_2^* = \frac{\tau_p}{\pi\sqrt{2}}\left(\frac{d}{\sigma_d}\right) \tag{4.2}$$

where d is the particle diameter and σd is its standard deviation. Thus T_2* was constrained by the size distribution determined with TEM for each particle sample (σ_d for each d listed in Table 4.4). Best fit parameters obtained from this procedure are given in Table 4.4. In the case of the 85 nm particles, T1 could not be accurately determined given the width of the particle size distribution (and therefore the dominance of T_2* in the overall damping dynamics), which is a consequence of the difficulty in controlling the Al NP size dispersity through the use of carboxyl functional groups. However, when T_1 was fixed at 38.7 ps (a value determined by simulations described later), the value of d/σd determined by fitting T_2* was within 10% of the value determined by TEM (4.4 vs 3.95, respectively).

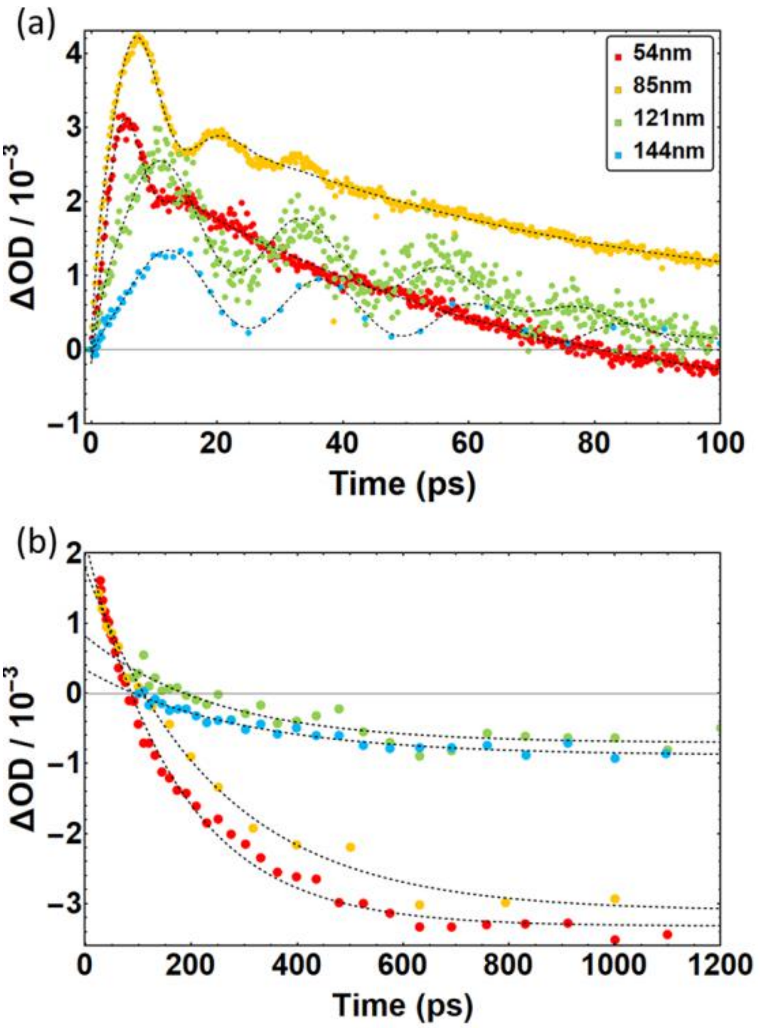

Figure 4.12 (a) Time-dependent changes in near-IR extinction (integrated 1000−1075 nm) observed for particles of each size. Fits are shown as dashed lines; fitting functions are described in the text. (b) Time-dependent signals for the same samples plotted on time scales relevant to thermal energy transfer to the solvent.

Table 4.4 Parameters Determined from Fitting the Time-Dependent Evolution of Transient Absorption Signals to Equation 1 and from TEM Analysis (d and σd) as a Function of Nanoparticle Size.

d (nm)	σ_d (nm)	d/σ_d	T_1 (ps)	T_2^* (ps)	τ_p (ps)	τ_r (ps)	τ_d (ps)	p (rad)
54	10.5	5.14	6.9	24.5	11.3	1.41	173	4.4
85	21.4	3.97	39	27.0	15.5	1.09	243	4.6
121	8.40	14.4	63	147	22.6	1.81	244	4.6
144	4.30	33.4	88	364	24.2	1.83	284	4.5

4.2.4 Acoustic Phonon Study using Finite-element Analysis

On the basis of our fits, we find that the phonon breathing period, T_1 damping time scale, and thermal-energy-transfer time scales increase monotonically with increasing particle size. In contrast, the initial signal rise time is similar across particle samples.

We note that we tried fitting the data without a rise component but found that the oscillatory component alone could not correctly capture the shape of the signal induction. This behavior is consistent with impulsive particle expansion as a combined result of electron−phonon and initial phonon−phonon thermalization that sets the coherent phonon modes into motion. Notably, τd, T1, and τp scale roughly linearly with the NP diameter, d.

The periods and damping time scales of the phonon vibrations extracted from the transient absorption data are determined by the mechanical properties of the Al NPs and their interactions with the surrounding chemical environment. Although our measurement results showed that both the Al NP size and the size dispersity clearly affect the phonon vibration dynamics, the role that the presence and the nature of the surface oxide and the organic ligand layer plays in the dynamics, if any, was unknown. We performed finite element method (FEM) calculations using frequency domain analysis to solve Navier's equation and the Navier−Stokes equations to model the vibrational period and the damping associated with the oscillations in the experimental data to answer this question. Our initial 3D model consisted of a single aluminum icosahedron with or without a 4 nm thick continuous, crystalline Al2O3 shell but excluded the organic ligands. The NP was surrounded by an IPA background in the simulations. For each particle size, we calculated the properties of the fundamental radial phonon mode, which dominate oscillations seen in TA data. The inset of Figure 4.9 (a) shows the displacement profile of the fundamental breathing mode of a core−shell Al/Al2O3 icosahedron. To investigate the size dependence of the Al NP phonon oscillations, we calculated the vibrational period and damping time for particles of four different sizes corresponding to our measured samples. As shown in Figure 4.9 (a), the oscillation periods of the core−shell particles are 7.6, 12, 17.1, and 20.6ps for particles with diameters of 54, 85, 121, and 144 nm, respectively. The oscillation periods of the fundamental breathing modes in the core−shell particles were slightly shorter than those calculated for pure Al NPs with the same diameters. The oscillation period has an approximately linear dependence on the diameter of the particle, which is consistent with Lamb’s theory. Our calculated results show similar trends compared with the values extracted from the transient spectral measurements, with some deviations. The damping time scale is defined as the time at which the displacement amplitude reaches 1/e of its initial value and is equivalent to T1 in Equation 1. In Figure 4.13 (b), we show the results of our FEM simulations for the phonon vibrational modes associated with particles of different sizes. Damping times of 34.5, 62, 95.4, and 116.2 ps were obtained for core−shell particles with diameters of 54, 85, 121, and 144 nm, respectively. The trend of longer damping times with larger particle sizes was consistent for both Al-only and Al/Al_2O_3 core/shell particles. However, these calculated damping times from our simple particle model are, in general, much longer than the values we extracted from the TA measurements. We attribute the discrepancy to the simplified model of the NP surface in the initial simulation model, in which we assumed purely crystalline Al (in the case of the bare Al particles) and Al_2O_3 (in the case of the core−shell particles) interacting with the surrounding fluid. We hypothesize that continuum damping processes associated with organic surfactant molecules bound to the particle surfaces as well as the noncrystalline and nonstoichiometric nature of the native aluminum oxide layer, the presence of which we confirmed with a suite of surface characterizations (Figures 4.5−4.10), could play a nontrivial role in the acoustic dynamics.

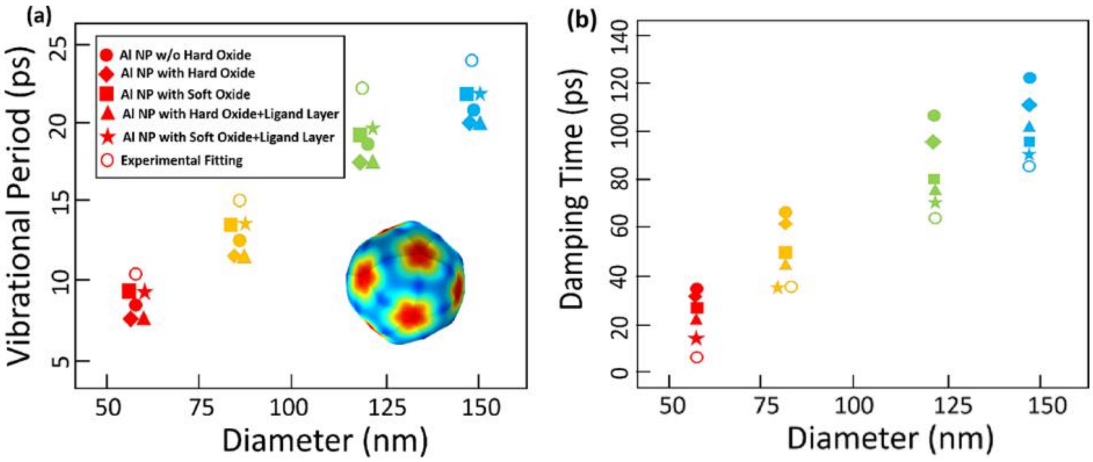

Figure 4.13 (a) Vibrational oscillation periods and (b) damping times calculated for icosahedral Al NPs of different sizes via finite element method simulations. The solid circles, rhombuses, squares, triangles, and open circles represent pure Al particles, particles with a 4 nm thick crystalline oxide shell, particles with a soft (reduced Young's modulus) oxide shell, particles with a 1.3 nm oleic-acid shell layer, and experimental results from TA measurements, respectively. The stars represent the combined simulation results for particles with both a soft oxide shell and an oleic-acid ligand layer. The inset of panel a is a calculation of the displacement of the fundamental radial mode for a 144 nm icosahedral Al NP with a 4 nm crystalline oxide shell.

We sought to account for the hypothesized noncrystalline nature of the thin aluminum oxide shell by reducing its assigned Young's modulus. As the Young's modulus of the oxide shell decreases, the damping time for particles of all sizes also decreases, whereas the oscillation period increases (Figure 4.14), leading to a closer match with experimental values.

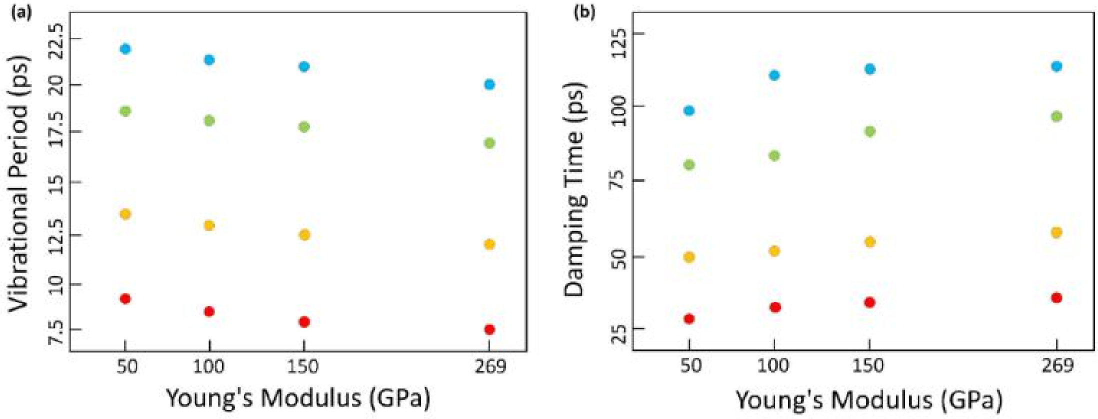

Figure 4.14 (a) Vibrational periods and (b) damping times calculated using finite element methods for single Al NPs with diameters of 54 nm (red), 85 nm (yellow), 121 nm (green), and 144 nm (blue) as a function of the Young's modulus of a 4 nm oxide shell layer which is varied between 50 GPa and 269 GPa.

The results of the FEM model for an oxide shell Young's modulus of 50 GPa, consistent with literature reports on amorphous oxides, are shown in Figure 4.13. We next added an additional 1.3 nm capping layer on top of the oxide surface in the simulation model to account for the presence of the oleic-acid capping ligands using mechanical properties for the ligand shell from literature reports. As can be seen in Figure 4.13 (a) and (b), adding a thin organic shell to the particles results in no significant change in the oscillation periods. However, the damping times were considerably decreased, and the soft ligand shell played a more important role in the damping properties of the smaller particles. This resulted in calculated decay times of 21.3, 46.6, 79.6, and 104.4ps, compared with the experimental decay times of 6.9, 39, 63, and 88 ps. The results from the FEM model that includes both a soft oxide shell and a ligand layer are also shown in Figure 4.13. We compare the vibrational periods and damping times for the four sets of NPs obtained via fitting of our transient absorption spectra (τ_p and T_1) and simulations of a single particle with a soft oxide shell and a ligand layer (τ_p.sim and T_1.sim) in Table 4.5. In a quantitative comparison with experiments, adding a soft oxide shell layer had the largest impact on the vibrational period, and the calculated results match the experimental values to within 9.1−18.1%, depending on the particle size. Adding a ligand shell to a crystalline oxide shell had a smaller effect on the vibrational period (a 14.5− 28.3% deviation from the experimental values) but produced damping times that are closer to the experimental values. In combination, the particle model that included both a soft oxide layer and an organic ligand shell most closely approached both the experimental vibrational period (primarily due to the soft oxide) and the damping time scale (primarily due to the ligand).

Table 4.5 Vibrational Periods and Damping Times for 54, 85, 121, and 144 nm Al NPs from TA Experiments (τp and T1) and FEM Simulations (τp.sim and T1.sim) Including Both a Soft Oxide Layer and Ligand Shell.

d (nm)	τ_p (ps)	$\tau_{p.\mathrm{sim}}$ (ps)	T_1 (ps)	$T_{1.\mathrm{sim}}$ (ps)
54	10.6	9.1	6.9	16.2
85	15.1	13.5	39	38.7
121	22.6	18.7	63	69.7
144	24.2	22	88	90.5

4.2.4 Size-dependent Thermal Energy Transfer

Finally, we used an extended two-interface model to calculate the temperature evolution in both the particles and the solvent. As shown in Figure 4.15, we calculated solvent thermal heating times associated with the peak value of $\Delta T/\Delta T_0$ in the solvent of 150, 210, 280, and 320 ps for particles with average diameters of 54, 85, 121, and 144 nm, respectively. Fast heat-transfer rates are observed for core−shell particles of all sizes compared with those predicted for aluminum-only particles, which follow the same trend as that in the TA measurements. This further confirms that the oxide shell efficiently mediates heat transfer between the particle and the solvent independent of particle size.

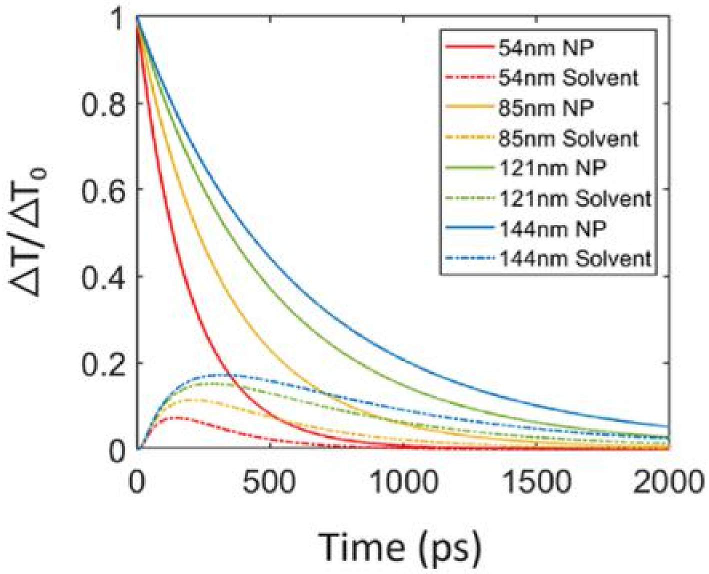

Figure 4.15 Normalized calculated temperature evolutions relative to the initial temperature increase at both the outer edge of the aluminum cores and 3 nm into the surrounding solvent (IPA) of core−shell Al/Al2O3 NPs with sizes ranging from 54 to 144 nm in diameter. An oxide shell layer of 4 nm in thickness is included in the simulation.

4.2.5 Conclusion

We studied the photothermal responses of solution-grown Al NPs as a function of the NP size. In our TA measurements, we observed fast heat-transfer rates to the solvent for NPs of all sizes, mediated by the native oxide shell, which is substantiated by the results of a two-interface model for heat transfer. We also observed phonon vibrations in the optical spectra with decreasing periods and damping times as the size of the NPs decreased. FEM calculations verify the qualitative trends observed in experiment. We refifined this model by considering surface effects on phonon damping and found that the noncrystalline nature of the native oxide shell and the presence of surface ligands lead to faster damping dynamics than predicted for pure Al NPs interacting with only a surrounding fluid. Our study provides insight into the roles of the surface composition and the particle size on both the photothermal and photoacoustic properties of Al-based plasmonic NPs. Specifically, by adding or subtracting “soft” surface components, such as oxide or polymer shells, phonon damping rates and thermal-energy-transfer times can be systematically increased or decreased. This effect could be useful for tuning NP properties “on demand” through a prescriptive design for applications in photocatalysis, sensing, and medicine.

References

[1] Cheng, Yan, Kenneth J. Smith, Ebuka S. Arinze, Rachel Dziatko, Tina Gao, Benjamin P. Frank, Susanna M. Thon, and Arthur E. Bragg. "Size and surface-dependent photoresponses of solution-processed aluminum nanoparticles." ACS Photonics (2020).

[2] Sau, T. K.; Rogach, A. L.; Jackel, F.; Klar, T. A.; Feldmann, J. Properties and Applications of Colloidal Nonspherical Noble Metal Nanoparticles. Adv. Mater. 2010, 22 (16), 1805−1825.

[3] Talapin, D. V.; Lee, J.-S.; Kovalenko, M. V.; Shevchenko, E. V. Prospects of Colloidal Nanocrystals for Electronic and Optoelectronic Applications. Chem. Rev. 2010, 110 (1), 389−458.

[4] Luo, X.; Morrin, A.; Killard, A. J.; Smyth, M. R. Application of Nanoparticles in Electrochemical Sensors and Biosensors. Electroanalysis 2006, 18 (4), 319−326.

[5] Guo, S.; Zhang, S.; Sun, S. Tuning Nanoparticle Catalysis for the Oxygen Reduction Reaction. Angew. Chem., Int. Ed. 2013, 52 (33), 8526−8544.

[6] Murray, R. W. Nanoelectrochemistry: Metal Nanoparticles, Nanoelectrodes, and Nanopores. Chem. Rev. 2008, 108 (7), 2688−2720.

[7] Wang, P.; Huang, B.; Dai, Y.; Whangbo, M.-H. Plasmonic Photocatalysts: Harvesting Visible Light with Noble Metal Nanoparticles. Phys. Chem. Chem. Phys. 2012, 14 (28), 9813−9825.

[8] Ma, X.-C.; Dai, Y.; Yu, L.; Huang, B.-B. Energy Transfer in Plasmonic Photocatalytic Composites. Light: Sci. Appl. 2016, 5 (2), No. e16017.

[9] Atta, S.; Pennington, A. M.; Celik, F. E.; Fabris, L. TiO2 on Gold Nanostars Enhances Photocatalytic Water Reduction in the NearInfrared Regime. Chem. 2018, 4 (9), 2140−2153.

[10] Mendez-Medrano, M. G.; Kowalska, E.; Lehoux, A.; Herissan, A.; Ohtani, B.; Bahena, D.; Briois, V.; Colbeau-Justin, C.; RodríguezLopez, J. L.; Remita, H. Surface Modification of TiO2 with Ag Nanoparticles and CuO Nanoclusters for Application in Photocatalysis. J. Phys. Chem. C 2016, 120 (9), 5143−5154.

[11] Qin, Z.; Bischof, J. C. Thermophysical and Biological Responses of Gold Nanoparticle Laser Heating. Chem. Soc. Rev. 2012, 41 (3), 1191−1217.

[12] Huang, X.; Jain, P. K.; El-Sayed, I. H.; El-Sayed, M. A. Plasmonic Photothermal Therapy (PPTT) Using Gold Nanoparticles. Lasers Med. Sci. 2008, 23 (3), 217.

[13] Jones, S.; Andren, D.; Karpinski, P.; Kall, M. Photothermal Heating of Plasmonic Nanoantennas: Influence on Trapped Particle Dynamics and Colloid Distribution. ACS Photonics 2018, 5 (7), 2878−2887.

[14] Kim, M.; Lee, J.-H.; Nam, J.-M. Plasmonic Photothermal Nanoparticles for Biomedical Applications. Adv. Sci. 2019, 6 (17), 1900471.

[15] Bagley, A. F.; Hill, S.; Rogers, G. S.; Bhatia, S. N. Plasmonic Photothermal Heating of Intraperitoneal Tumors through the Use of an Implanted Near-Infrared Source. ACS Nano 2013, 7 (9), 8089− 8097.

[16] Braun, M.; Cichos, F. Optically Controlled Thermophoretic Trapping of Single Nano-Objects. ACS Nano 2013, 7 (12), 11200− 11208.

[17] Chen, J.; Cong, H.; Loo, F.-C.; Kang, Z.; Tang, M.; Zhang, H.; Wu, S.-Y.; Kong, S.-K.; Ho, H.-P. Thermal Gradient Induced Tweezers for the Manipulation of Particles and Cells. Sci. Rep. 2016, 6.

[18] Su, M.-N.; Dongare, P. D.; Chakraborty, D.; Zhang, Y.; Yi, C.; Wen, F.; Chang, W.-S.; Nordlander, P.; Sader, J. E.; Halas, N. J.; et al. Optomechanics of Single Aluminum Nanodisks. Nano Lett. 2017, 17 (4), 2575−2583.

[19] Su, M.-N.; Ciccarino, C. J.; Kumar, S.; Dongare, P. D.; Hosseini Jebeli, S. A.; Renard, D.; Zhang, Y.; Ostovar, B.; Chang, W.-S.; Nordlander, P.; et al. Ultrafast Electron Dynamics in Single Aluminum Nanostructures. Nano Lett. 2019, 19 (5), 3091−3097.

[20] Crut, A.; Maioli, P.; Del Fatti, N.; Vallee, F. Acoustic Vibrations of Metal Nano-Objects: Time-Domain Investigations. Phys. Rep. 2015, 549, 1−43.

[21] Stoll, T.; Maioli, P.; Crut, A.; Burgin, J.; Langot, P.; Pellarin, M.; Sanchez-Iglesias, A.; Rodríguez-Gonzalez, B.; Liz-Marzan, L. M.; Del Fatti, N.; et al. Ultrafast Acoustic Vibrations of Bimetallic Nanoparticles. J. Phys. Chem. C 2015, 119 (3), 1591−1599.

[22] Kirakosyan, A. S.; Shahbazyan, T. V. Vibrational Modes of Metal Nanoshells and Bimetallic Core-Shell Nanoparticles. J. Chem. Phys. 2008, 129 (3), No. 034708.

[23] Hodak, J. H.; Henglein, A.; Hartland, G. V. Photophysics of Nanometer Sized Metal Particles: Electron-Phonon Coupling and Coherent Excitation of Breathing Vibrational Modes. J. Phys. Chem. B 2000, 104 (43), 9954−9965.

[24] Mongin, D.; Juve, V.; Maioli, P.; Crut, A.; Del Fatti, N.; Vallee, F.; Sanchez-Iglesias, A.; Pastoriza-Santos, I.; Liz-Marzan, L. M. Acoustic Vibrations of Metal-Dielectric Core−Shell Nanoparticles. Nano Lett. 2011, 11 (7), 3016−3021.

Chapter 5

Multicolored and Semi-transparent PbS CQDs Solar Cells using Optimized Multi-layer Interference

This section is adapted from Reference [1]. Reprinted with permission from Optics Express 24, no. 4, A101-A112, "Color-tuned and transparent colloidal quantum dot solar cells via optimized multilayer interference," by E.S. Arinze, B. Qiu, N. Palmquist, Y. Cheng, Y. Lin, G. Nyirjesy, G. Qian, and S. M. Thon, copyright © 2017.

5.1 Introduction

Multi-colored solar cells, solar cells with controlled, tunable spectral reflection and absorption profiles, are of significant interest due to their potential to be coated on exterior surfaces of urban infrastructures, such as building facades, rooftops and automotive skins, to serve both aesthetic and functional purposes [1,2]. In tandem cell applications, there is also a need to systematically control absorption and, in turn, achieve the required current-matching in cells that possess different spectral absorption profiles. Additionally, semitransparent solar cells are attractive for integration into portable electronics [3] and for window coatings to help with building and vehicular heat management [4,5]. Solar cells based on solution processed materials are especially promising for these large-area applications because of their thin-film and lightweight nature, ease and flexibility of fabrication, associated low costs, and high efficiency potential. Past examples of colored solution-processed solar cell technologies include using combinations of dyes [6], photonic filters [7], physically- or chemically-modified absorbing/transport layers [8], integrated liquid/photonic crystals [9], embedded optical microcavities and dielectric mirrors [10], and modified top/bottom electrodes in dye-sensitized, organic, and perovskite solar cells [11,12]. Although multi-colored and semitransparent solar cells based on perovskites and organic materials have been demonstrated, their narrow spectral absorbing ranges, which lie mainly within the visible portion of the spectrum, represent a significant drawback for achieving high photocurrents. As a result, light management strategies to produce cell colors or achieve transparency come with an unavoidable loss of device efficiency.

Colloidal quantum dots (CQDs), semiconducting nanocrystals stabilized in solution, are a promising candidate material for achieving multicolored and semitransparent solar cells due to their band gap tunability, which is enabled by the quantum size effect, Specifically, lead sulfide and lead selenide (PbS, bulk band gap energy of 0.41 eV , and PbSe, bulk band gap energy of 0.27 eV) CQDs have band gaps that can be tuned from the near-infrared to the visible portion of the spectrum. As a result, visible absorption losses induced by the design of multicolored or semitransparent cells can potentially be compensated for by enhanced absorption in the infrared region.

Standard CQD film-based devices (Figure 5.1) [13-15] employ different electronic layers that have thicknesses on the order of the optical wavelengths of interest. The layer thicknesses and design are typically optimized for their electrical properties, but optical thin-film interference plays a large role in these devices as well, as demonstrated by efforts to utilize interference effects to achieve semitransparency and absorption enhancement via electrode modification [16,17] and microcavity structuring[18,19]. Traditionally, transparency in CQD-based devices is induced by employing thin absorbing layers [20,21]. In this study, we design, optimize and fabricate multicolored and transparent CQD solar cells based on thin film interference engineering concepts to customize both optical and electrical device properties [22]. Using physical and mathematical modeling techniques, including Transfer Matrix Method (TMM) calculations [23] and multiobjective optimization algorithms [24,25], we have developed an optimization method for the custom-design of multicolored and transparent CQD solar cells that could be generalized to other materials systems. The optimization sequence is depicted in Figure 5.1(c). The method maximizes reflection and transmission at specific wavelengths, creating a desired cell color, while simultaneously requiring high photocarrier generation rates in a solar cell device. Our multi-layer thin film calculations were based on a depleted heterojunction architecture design for CQD photovoltaics, but could be generalized to include any optoelectronic layer structure. Figure 5.1 shows an example of this architecture, which consists of an optically thick glass substrate, followed by indium tin oxide (ITO, the bottom contact), TiO2 (the n-type layer), PbS CQD film (the p-type layer), MoO3 (buffer layer), and Ag (the top electrode).

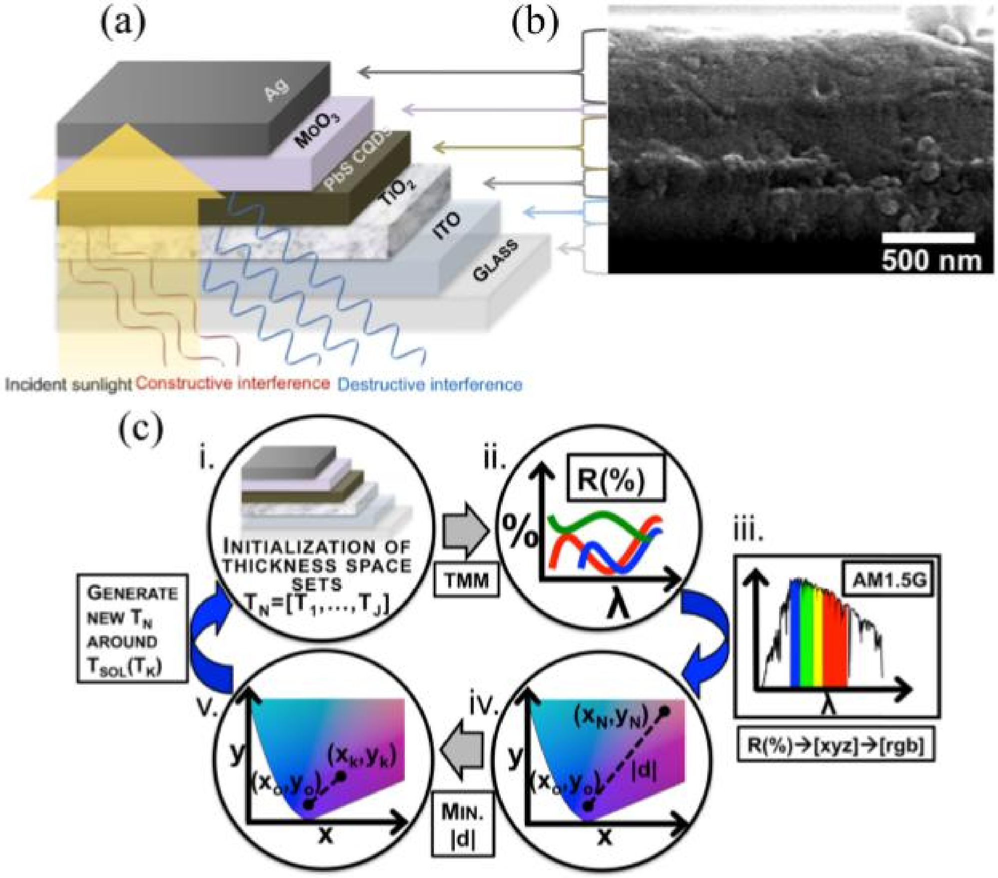

Figure 5.1 (a) Schematic of a CQD-based solar cell illustrating the spectrally-dependent optical interference patterns that can result from tuning the thicknesses of the different cell layers. As incident broadband sunlight passes through the device, constructive or destructive interference occurs at certain wavelengths, resulting in wavelength-dependent reflectivity and transmission, giving the cell its apparent color or semitransparency. (b) Cross-sectional scanning electron microscope (SEM) image of the structure shown in (a) with the layers labeled. (c) Graphic representation of the optimization technique to produce cells with defined color characteristics. Space set of thickness combinations is (i) initialized and each combination is transformed to (ii) a reflection spectrum via TMM. These spectra in combination with incident (iii) AM1.5G and color matching functions are translated to rgb colors on (iv) chromaticity plots where the distance to the intended color is (v) minimized. This optimization cycle repeats until a global minimum is realized.

5.2 Optimization of the Photocurrent-color Tradeoff

Our device model makes the following initial assumptions: (1) layers included in the multilayer device are considered homogeneous and isotropic; (2) interfaces are parallel and optically flat; (3) light is incident normal to the device and can be modeled as a plane wave; (4) all photogenerated charge carriers contribute to photocurrent in the device (100% internal quantum efficiency). All of these assumptions can be removed as-needed by modifying the materials models and incorporating experimental data into the calculations.

We use the TMM, which takes the thicknesses and complex refractive indices of all layers as inputs, and calculates normalized electrical field profiles within the multi-layer structure. In our simulations, the materials models are composed of complex refractive index data from the literature and experimental ellipsometry measurements, and we consider a broadband illumination source with a wavelength range of 300–1800 nm. In the case of opaque reflective colored solar cells, Ag is used as the back contact, and ITO is used as the back contact for the semitransparent solar cells. We calculate the reflection spectrum of the device, and predict the expected “color” by combining this spectrum with an appropriate set of color matching functions (1931 CIE) and an illuminating spectrum (AM1.5G). The predicted color can be represented on a 2-dimensional chromaticity plot, as shown in Figure 5.3(a) Cell “transparency” is calculated by averaging transmittance data over the visible wavelength range (420 nm – 680 nm) output by the TMM calculations.

In order to optimize the color response of our cells, we use particle swarm optimization (PSO), a population-based algorithm, tailored for our specific application, as illustrated in Figure 5.1(c). A “swarm size” of solution thickness sets is initialized and fed into the TMM to generate associated reflection spectra, which are then transformed to apparent color. These [rgb] co-ordinates are then optimized for a specific reflected color/wavelength response by minimizing the distance between the target point and solution point on the chromaticity plot, yielding a global solution via multiple iterations. The presence of two different populations (pbest and pcurrent) and particle movements in PSO allows for both greater degrees of exploration and faster convergence when compared to other optimization methods, such as genetic algorithms. Due to the multilayer architecture of our device and highly multidimenstional search space involved, a semi-periodic reflectivity landscape with multiple local minima emerges. Therefore, employing a PSO with a relatively large "swarm size" provides an efficient route to identifying the global minimum for our highly multidimensional optimization problem. Despite the infrared responsivity of the PbS CQDs, there still exists a trade-off between the available photocurrent and visible transparency in device designs. This trade-off can be partially mitigated by taking the advantage of multi-layer interference effects to reduce visible field overlap with the CQD layer while maintaining absorption in the infrared. In order to achieve high photocurrent with minimum loss of visible transparency, we used PSO to perform single-objective optimizations on the layer thicknesses, keeping the PbS layer thickness constant. The three optimization targets chosen to explore the entire parameter space involved with the trade-off were high transparency, high photocurrent, and low transparency. The available photocurrent and average transparency of each solution to the three optimization problems are shown in Figure 5.2.

In Figure 5.2 (a), the average transparency is plotted as a function of CQD layer thickness, and the available photocurrent is represented by the color. The top curve is the set of solutions at each given PbS CQD film thickness optimized for the highest transparency. The middle curve is optimized for the highest photocurrent at each film thickness. Higher photocurrent comes with the expected trade-off of lower transparency. The bottom curve is calculated for the lowest transparency, and it has the lowest available photocurrent of the three sets of solutions. The difference between the bottom curve and the middle curve represents both the photocurrent and degree of transparency that can be gained for a given active layer thickness by doing a rational layer thickness optimization via our method. The high photocurrent for the middle curve is achieved by maximizing the electric field intensity within the absorbing layer. The high transparency of the top curve is achieved by employing multi-layer interference to minimize the electric field intensity at visible wavelengths within the absorbing layer. The difference between these two cases is visualized in Figures 5.2(b) and 5.2(c). In the optimized photocurrent case (Figure 5.2(c)), there is an intensity peak at a wavelength near 700 nm within the CQD film, allowing more longer wavelength light to be absorbed within this layer. In the optimized transparency case (Figure 5.2(b)), there is no electric field intensity peak at the edge of the visible spectral range; instead, there is a peak closer to 800 nm at the NIR edge, allowing visible light to be transmitted and maintaining a relatively high photocurrent through NIR photon absorption.

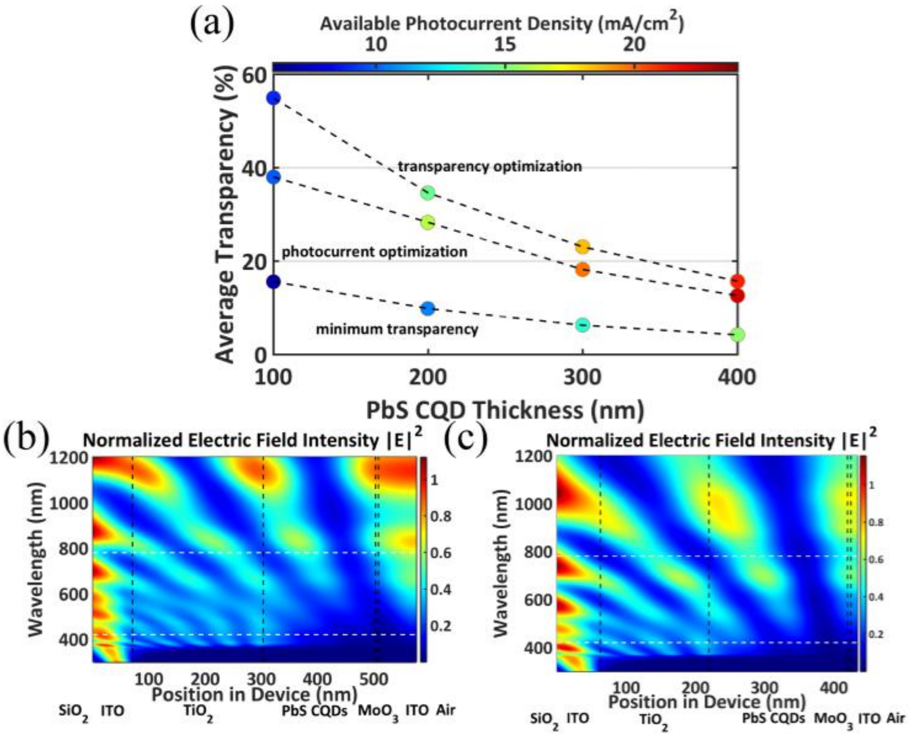

Figure 5.2 (a) Calculated average transparency (%) and corresponding available photocurrent density (mA/cm^2, color bar) versus PbS CQD film thickness (nm). Top curve: optimized for maximum average visible transparency. Middle curve: optimized for maximum available photocurrent density. Bottom curve: calculated for minimum average transparency. Calculated electric field intensity as a function of wavelength and position in the transparent device structure (ITO back contact) with a PbS CQD layer thickness of 200 nm for: (b) transparency optimized case; (c) photocurrent-optimized case.

The tradeoffs between attainable color or transparency and minimum device photocurrent are illustrated in Figure 5.3(a). From this plot, it is apparent that photocurrent requirements more strongly affect "redder" colors, whereas the range of "bluer" colors that can be achieved shows little correlation with achievable photocurrent. Figure 5.3(b) shows transmittance plots for devices optimized for their transparency based on photocurrent restrictions. As expected, lower required device photocurrents result in higher potential visual transparency levels. Figure 5.3(c) shows the dependence of the photocurrent/transparency tradeoff on the CQD excitonic peak wavelength.

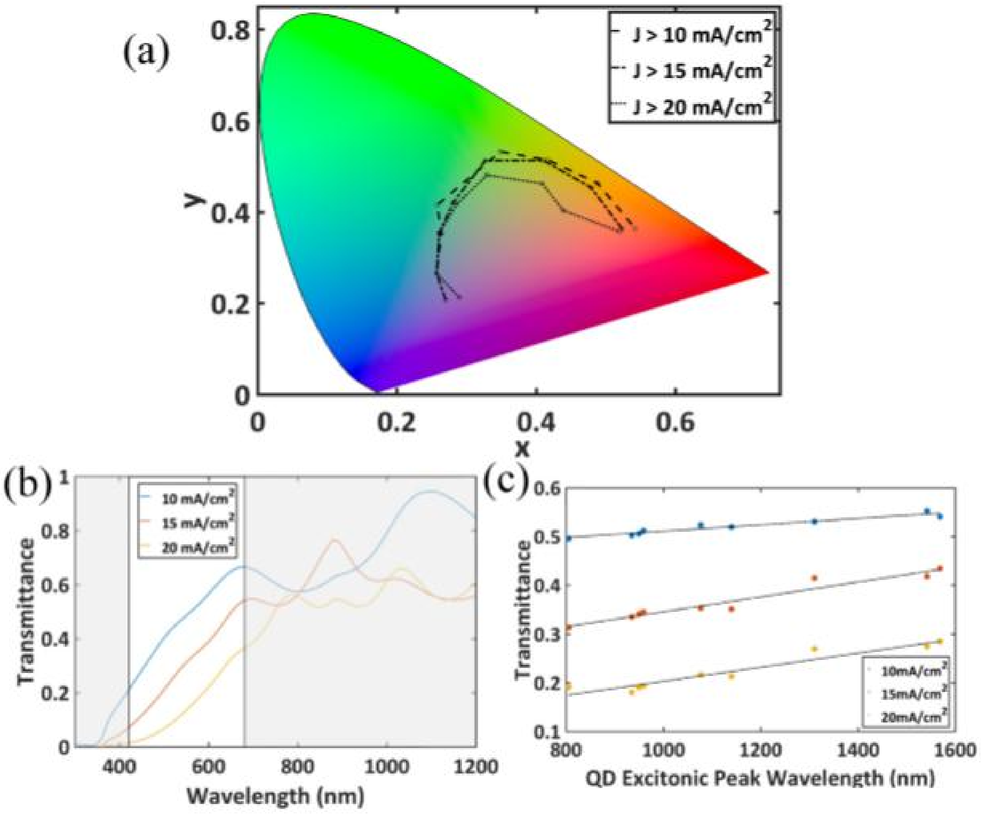

Figure 5.3 (a) Chromaticity plot showing achievable colors given minimum photocurrent requirements (J>10 mA/cm^2, J>15 mA/cm^2, and J > 20 mA/cm^2). Calculated Transmittance plots showing: (b) trade-off between transparency and photocurrent (for CQDs with 950 nm exciton peak wavelength), and (c) achievable transparency given minimum photocurrent requirements for different CQD excitonic peak wavelengths.

5.3 Effects of Non-ideal Layers on Color Saturation

In evaluating the prospects for real devices, it is important to take into account non-ideal effects, such as interface roughness, non-uniformity of the layer physical properties, and the presence of scattering centers formed by impurities and contaminants. We can incorporate these effects into our model by using another parameter, the effective "optical roughness" of each layer. We create a sufficiently large number of samples with random thicknesses by adding the standard deviation of a Gaussian distribution based on the measured or assumed roughness to the mean thickness for each layer. We then calculate the reflectance curve of each sample in the distribution and statistically average the reflectance from all samples to derive the effective reflectance curves.

Due to the nanostructured nature of the material itself as well as the deposition technique, the CQD layer typically has a geometrical roughness of 3-10 nm. The geometrical roughness of the underlying electrodes and oxide layers deposited by evaporation, which can be determined from surface profilometry, is usually smaller than that of the CQD films. However, the effective optical roughness can be significantly greater than the geometrical roughness. One possible origin of optical inhomogeneity in the ITO and TiO_2 layers is the compositional and structural non-uniformity introduced during the deposition and processing steps, which can be seen as a spatial variation in the refractive index profile of the electrode films. Figure 4 shows the effects of non-ideal interference on the reflectance curves as well as the effective colors of the devices. As can be seen in Figure 5.4 (a), the reflectance from devices with rough CQD layers is smoothed in the red spectral region, while the shorter-wavelength region is mostly unaffected by the roughness. For rough TiO_2 and ITO layers, the deviations from the ideal case are greater in the blue region. The changes in the reflectance curves reduce the wavelength selectivity, and make the apparent color less saturated. The chromaticity plot in Figure 5.4 (b) demonstrates this effect for a device that is designed to be blue in color. As the effective optical roughness of the ITO/TiO_2 layer increases, the chromaticity point moves towards the white point, decreasing the saturation, and shifting the color towards brown-grey. In Figure 5.4(c), after accounting for the optical roughness, all 3 points corresponding to the maximum achievable saturation of red, blue and green, are closer to the white point. This approach to considering the effects of non-ideal interference is particularly useful for understanding color in real devices.

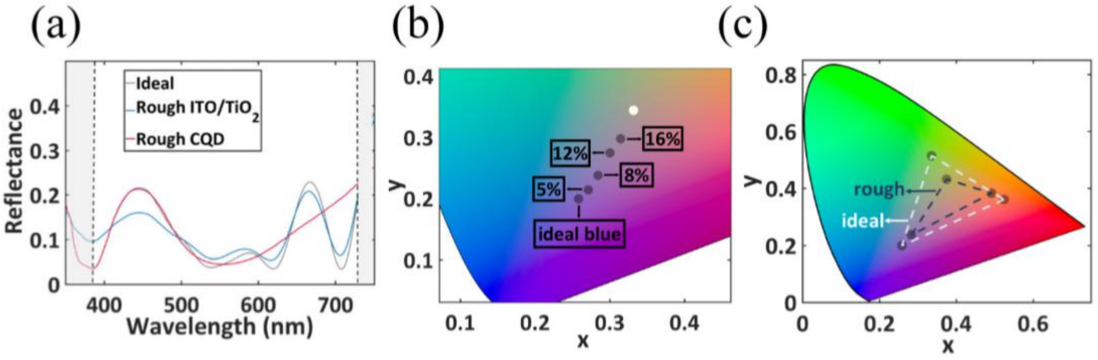

Fig. 5.4 (a) Simulated reflectance curves for a specific color objective with and without an effective optical roughness of 10% for the ITO/TiO2 layers and 10% for the CQD layer. (b) Effects of different levels of roughness on the chromaticity of a "blue" device. Percentages refer to the ratio of the standard deviation to the ideal thickness of the ITO/TiO2 layer. The white point of the standard illuminant is also plotted as a reference point. (c) Roughness (10%) has the effect of moving the vertices on the largest achievable triangle of color profiles closer to the white point.

5.4 Application in Tandem Structures

Our proposed method for color-tuning CQD solar cells is of particular interest for applications in all-CQD and hybrid tandem photovoltaics, where current-matching is critical to series-connected device performance. CQDs are particularly suited to tandem applications because of their band gap tunability, infrared responsivity, and compatibility with a variety of materials systems afforded by their solution-processing. This flexibility effectively eliminates the difficulty of finding a materials combination possessing both appropriate band gaps and suitable lattice matching for optimized multijunction cells. Proof-of-principle studies have demonstrated tandem structures utilizing all-CQD materials systems and CQDs in conjunction with polymer materials. In these series-connected CQD tandem structures, current matching is essential to obtain high efficiency devices. Generally, this is achieved by empirically adjusting the layer thicknesses until approximately equal photon absorption occurs in the two active layers. Here, we use our optimization algorithm to take into account the effects of interference in a multilayered stack to design optimum absorbing layer thicknesses. For our optimization simulation, we employed a PbS CQD system comprised of 1.55 eV and 0.95 eV dots which are both within 5% of the optimum band gaps for the maximum efficiency in a two-junction tandem structure. In addition, our simulated tandem structure integrated a graded recombination layer as demonstrated in a previous study. Calculating absorption using only the Beer-Lambert law in the active layers, not taking into account reflection, gave optimum thicknesses of 350 nm and 247 nm for the front and back cells, respectively, predicting a maximum photocurrent of 18.1 mA/cm2. Using our optimization process, we obtained optimum thicknesses of 350 nm and 196 nm for the front and back cells, respectively, achieving an output-matched photocurrent of 18.6 mA/cm2. We achieved a ~3% increase in expected photocurrent using our optimized approach, even though it takes into account reflection and the detrimental parasitic absorptions in the electrodes and the other non-active layers in the 9 layer tandem stack, whereas the control case does not. Our optimization method, accounting for both interference and reflection, provides an efficient route for tandem layer designs in both CQD and hybrid systems.

5.5 Experimental Results and Discussion

We fabricated several proof-of-principle CQD solar cell devices based on our optimization method designs for different colors using PbS CQDs with exciton peak wavelengths near 950 nm. To minimize the fabrication uncertainty in the layer thicknesses, we used commercial ITO-coated glass substrates with ITO thicknesses of 28 nm for our “red” and “green” cell designs. For the “blue” cell, we deposited ITO on a glass substrate via e-beam evaporation, followed by an annealing process, to obtain our target optical thickness. The TiO2 layer was also deposited using e-beam evaporation for precise thickness control, and a TiCl4 solution treatment was applied afterwards. The PbS CQD layer was built up using a layer-bylayer solid state ligand exchange process. Two or three drops of oleic acid capped PbS CQD solution at a concentration of 50 mg/mL per layer were deposited through a 0.22 μm pore filter and spin-cast on the substrate. 0.5% mercaptopropionic acid (MPA) in methanol was used to soak the film for 3 seconds to replace the oleic acid, then the film was spin-cast dry. Lastly, the films were washed with methanol twice to remove the unbound ligands, completing the deposition of one CQD film layer. The total CQD film thickness was controlled through the acceleration, spin speed, spin time and number of layers and verified using profilometry measurements. We were able to control the thickness of the CQD layers to within +/− 15 nm. The top contact was composed of a thin MoO3 buffer layer and Ag, which were both deposited via e-beam evaporation. Photographs of the colored and transparent cells are shown in Figure 5.5(a). We measured the reflectance of each solar cell using an Agilent Cary 5000 UV-Vis-NIR spectrophotometer with an integrating sphere insert, calculated the corresponding xyz color values by integrating over the AM1.5G spectrum, and plotted them in a chromaticity diagram. The reflectance spectra are plotted in Figure 5.5(b), and the calculated color of the fabricated devices is shown in Figure 5.5(d).

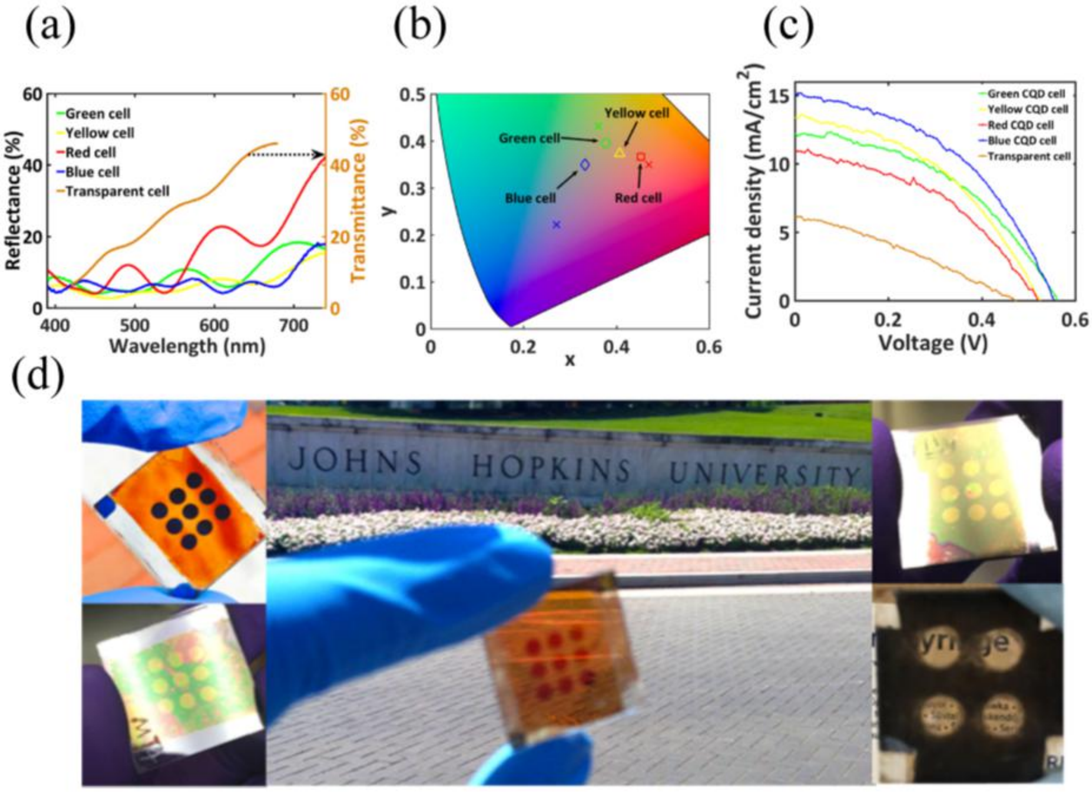

Figure 5.5 (a) Experimental reflectance and transmittance spectra for colored and semi-transparent solar cells, respectively. (b) Chromaticity plot showing the calculated coordinates for different colored devices. Crosses indicate design points while corresponding colored shapes indicate experimental points. (c) J-V characteristics taken under simulated solar illumination for colored and semi-transparent devices. (d) Photographs of blue (upper left), green (lower left), red (center), yellow (upper right), and semi-transparent (lower right) CQD solar cells.

We also fabricated semi-transparent devices based on our optimization method. The top contact of these devices was a composite electrode consisting of spin-coated Ag nanowires and ITO nanoparticles. Our test devices had measured visible transparencies ranging from 27.3% to 32.2%. The measured transmittance spectrum of the highest efficiency device is plotted in Figure 5.5(c).

All current density-voltage measurements were carried out in a nitrogen-purged environment. Current density−voltage curves were measured using a Keithley 2400 source meter with illumination provided by a Sciencetech solar simulator with an irradiance of 1000 W/m^2. The active area of the solar cell was illuminated through a circular aperture with an area of 0.044 cm2 ± 0.003 cm^2. The power through the aperture, measured using a Thorlabs broadband power meter, was used to calibrate the power density. The measured short circuit current (JSC), open circuit voltage (VOC), fill factor (FF), and power conversion efficiency (PCE) for the different cells are summarized in Table 5.1. The differences in performance between the devices are related to their different design parameters, which are determined by the need to optimize reflection and transmission over specific wavelength ranges. Blue is a relatively difficult color to produce using this method, since the reflections are minimized due to the strong absorption of the CQD film in the blue region of the spectrum. The optimal design included a very thick CQD film layer. The lower FF of the semi-transparent device is related to the difficulty in making a strongly conducting top transparent contact without heat-processing due to the presence of the temperaturesensitive underlying CQD film. Generally, the experimental photocurrents were smaller than those predicted by the simulations by approximately 50-60%, due to experimental deviations from the model assumptions. The simulations make the assumption of perfect carrier collection (IQE = 100%), whereas CQD solar cell IQE is typically on the order of 50-90% above the band gap. Additionally, experimental variations in the device layer thicknesses can contribute to lower average photocurrents. On average, the ITO, TiO2, and PbS CQD layer thicknesses in our devices were within 15nm, 10nm, and 15nm, respectively, of the design thicknesses.

Table 5.1 Average performance characteristics of colored and transparent solar cell devices showing open-circuit voltage (VOC), short-circuit current (JSC), fill factor (FF) and power conversion efficiency (PCE). All measurements are for at least 6 devices.

Cell Type	**V_{OC}(V)**	**J_{SC}(mA/cm^2)**	**FF**	**PCE (%)**	**Design Parameters ITO/TiO$_2$/PbS/MoO$_3$/Ag (nm)**
Blue	0.56 ± 0.01	14.5 ± 0.6	0.43 ± 0.01	3.5 ± 0.1	240/113/400/100/475
Green	0.55 ± 0.01	12.1 ± 0.7	0.42 ± 0.02	2.8 ± 0.1	28/150/297/12/60
Yellow	0.51 ± 0.05	12.4 ± 0.7	0.40 ± 0.04	2.5 ± 0.5	28/150/297/12/60
Red	0.48 ± 0.06	10.2 ± 0.7	0.40 ± 0.04	2.0 ± 0.5	28/166/222/22/274
Transparent	0.45 ± 0.06	5.1 ± 0.7	0.31 ± 0.01	0.7 ± 0.2	28/349/170/17/85(ITO)

5.6 Conclusion and Outlook

We developed a method for producing arbitrary spectral profiles in layered solar cell structures using thin film interference modeling techniques combined with optimization algorithms. At selected wavelengths, our model maximizes reflection and/or transmission to create a target color and transparency level while simultaneously maximizing photocarrier generation rates. Our study revealed that designs with minimum transparency do not necessarily correspond to the highest attainable device photocurrent, providing a pathway for high efficiency colored devices. Although effective optical roughness in the films decreases the color saturation, CQD solar cell devices with well-defined color profiles can still be produced. Our optimization method produced layer designs for tandem solar cell applications, with increases in expected photocurrent over conventional designs despite taking into account optical losses. Experimentally, we fabricated proof-of-principle blue, green, yellow, red and semi-transparent devices. The measured reflectance and transmittance spectra agreed well with the perceived color and transparency levels. Future work will focus on broadening the application of our model to hybrid materials systems (single junction and tandem design structures based on non-CQD-based films) and explicitly including additional loss mechanisms. The device layer structure used in this study includes a wide band gap n-type TiO_2 layer, an absorbing p-type CQD thin film, and a MoO_3 buffer layer. The overall device performance could be improved by employing the current best-performing CQD device architecture strategies which inlcude graded doped CQD layers formed using solution-based halide passivation treatments. This architecture strategy substitutes the TiO_2 layer for a ZnO thin film with higher electron mobility, eliminates the buffer layer, and incorporates a graded doped CQD layer for higher charge extraction efficiency. Finally, this work, coupled with the development of more efficient room temperature-processed transparent electrode materials, should extend the range of functionalities of flexible optoelectronic devices.

Reference

[1] Arinze, Ebuka S., Botong Qiu, Nathan Palmquist, Yan Cheng, Yida Lin, Gabrielle Nyirjesy, Gary Qian, and Susanna M. Thon. "Color-tuned and transparent colloidal quantum dot solar cells via optimized multilayer interference." Optics express 25, no. 4 (2017): A101-A112.

[2] A. Henemann, “BIPV: Built-in solar energy,” Renew. Energy Focus 9(6), 14–19 (2008).

[3] Z. L. Wang, G. Zhu, Y. Yang, S. Wang, and C. Pan, “Progress in nanogenerators for portable electronics,” Mater. Today 15(12), 532–543 (2012).

[4] H. Davidsson, B. Perers, and B. Karlsson, “Performance of a multifunctional PV/T hybrid solar window,” Sol. Energy 84(3), 365–372 (2010).

[5] T. Miyazaki, A. Akisawa, and T. Kashiwagi, “Energy savings of office buildings by the use of semi-transparent solar cells for windows,” Renew. Energy 30(3), 281–304 (2005).

[6] H. Otaka, M. Kira, K. Yano, S. Ito, H. Mitekura, T. Kawata, and F. Matsui, “Multi-colored dye-sensitized solar cells,” J. Photochem. Photobiol. Chem. 164(1-3), 67–73 (2004).

[7] H. J. Park, T. Xu, J. Y. Lee, A. Ledbetter, and L. J. Guo, “Photonic color filters integrated with organic solar cells for energy harvesting,” ACS Nano 5(9), 7055–7060 (2011).

[8] C.-C. Chueh, S.-C. Chien, H.-L. Yip, J. F. Salinas, C.-Z. Li, K.-S. Chen, F.-C. Chen, W.-C. Chen, and A. K.-Y. Jen, “Toward High-Performance Semi-Transparent Polymer Solar Cells: Optimization of Ultra-Thin Light Absorbing Layer and Transparent Cathode Architecture,” Adv. Energy Mater. 3(4), 417–423 (2013).

[9] W. Zhang, M. Anaya, G. Lozano, M. E. Calvo, M. B. Johnston, H. Míguez, and H. J. Snaith, "Highly efficient perovskite solar cells with tunable structural color," Nano Lett. 15(3), 1698–1702 (2015).

[10] K.-T. Lee, M. Fukuda, S. Joglekar, and L. J. Guo, "Colored, see-through perovskite solar cells employing an optical cavity," J. Mater. Chem. C Mater. Opt. Electron. Devices 3(21), 5377–5382 (2015).

[11] Y.-Y. Lee, K.-H. Tu, C.-C. Yu, S.-S. Li, J.-Y. Hwang, C.-C. Lin, K.-H. Chen, L.-C. Chen, H.-L. Chen, and C.-W. Chen, "Top Laminated Graphene Electrode in a Semitransparent Polymer Solar Cell by Simultaneous Thermal Annealing/Releasing Method," ACS Nano 5(8), 6564–6570 (2011).

[12] R. Koeppe, D. Hoeglinger, P. A. Troshin, R. N. Lyubovskaya, V. F. Razumov, and N. S. Sariciftci, "Organic Solar Cells with Semitransparent Metal Back Contacts for Power Window Applications," ChemSusChem 2(4), 309–313 (2009).

[13] E. H. Sargent, "Colloidal quantum dot solar cells," Nat. Photonics 6(3), 133–135 (2012).

[14] G. H. Carey, A. L. Abdelhady, Z. Ning, S. M. Thon, O. M. Bakr, and E. H. Sargent, "Colloidal Quantum Dot Solar Cells," Chem. Rev. 115(23), 12732–12763 (2015).

[15] S. Emin, S. P. Singh, L. Han, N. Satoh, and A. Islam, "Colloidal quantum dot solar cells," Sol. Energy 85(6), 1264–1282 (2011).

[16] X. Zhang, C. Hägglund, M. B. Johansson, K. Sveinbjörnsson, and E. M. J. Johansson, "Fine Tuned Nanolayered Metal/Metal Oxide Electrode for Semitransparent Colloidal Quantum Dot Solar Cells," Adv. Funct. Mater. 26(12), 1921–1929 (2016).

[17] X. Zhang, C. Hägglund, and E. M. J. Johansson, "Highly Efficient, Transparent and Stable Semitransparent Colloidal Quantum Dot Solar Cells: A Combined Numerical Modeling and Experimental Approach," Energy Environ. Sci. advance article (2017).

[18] X. Zhang and E. M. J. Johansson, "Utilizing light trapping interference effects in microcavity structured colloidal quantum dot solar cells: A combined theoretical and experimental approach," Nano Energy 28, 71–77 (2016).

[19] O. Ouellette, N. Hossain, B. R. Sutherland, A. Kiani, F. P. García de Arquer, H. Tan, M. Chaker, S. Hoogland, and E. H. Sargent, "Optical Resonance Engineering for

Infrared Colloidal Quantum Dot Photovoltaics," ACS Energy Lett. 1(4), 852–857 (2016).

[20] X. Zhang, G. E. Eperon, J. Liu, and E. M. J. Johansson, "Semitransparent quantum dot solar cell," Nano Energy 22, 70–78 (2016).

[21] S. Akhavan, B. Guzelturk, V. K. Sharma, and H. V. Demir, "Large-area semi-transparent light-sensitive nanocrystal skins," Opt. Express 20(23), 25255–25266 (2012).

[22] E. S. Arinze, G. Nyirjesy, Y. Cheng, N. Palmquist, and S. M. Thon, "Colloidal quantum dot materials for infrared optoelectronics," in (2015), Vol. 9608, pp. 960813–960813–9.

[23] G. F. Burkhard, E. T. Hoke, and M. D. McGehee, "Accounting for Interference, Scattering, and Electrode Absorption To Make Accurate Internal Quantum Efficiency Measurements in Organic and Other Thin Solar Cells," Adv. Mater. 22(30), 3293–3297 (2010).

[24] J. Kennedy, "Particle Swarm Optimization," in Encyclopedia of Machine Learning, C. Sammut and G. I. Webb, eds. (Springer US, 2011), pp. 760–766.

[25] K. Deb, Multi-Objective Optimization Using Evolutionary Algorithms (John Wiley & Sons, 2001).

Chapter 6

Antimony Selenide Nanowires for Flexible Broadband Photodetectors

This section is adapted from Reference [1]. Reprinted with permission from Advanced Electronic Materials, 2, no. 9, 1600182, "An Antimony Selenide Molecular Ink for Flexible Broadband Photodetectors," by M. R. Hasan, E. S. Arinze, A. K. Singh, V. P. Oleshko, S. Guo, A. Rani, Y. Cheng, I. Kalish, , M. E. Zaghloul, M. V. Rao, N. V. Nguyen, A. Motayed, A. V. Davydov, S. M. Thon and R. Debnath, copyright © 2016.

6.1 Introduction

As digital imaging devices gain in popularity, the quest for new infrared-sensitive materials that do not depend on epitaxial thin-film deposition techniques has intensified. The ability to deposit semiconducting films from solution has shown great potential for various electronic and optoelectronic applications and emerged as an attractive low-cost approach to fabricating high-quality semiconducting thin films

[2-7]. One can simply employ “soft” nonvacuum processes such as spin-coating, ink-jet printing, and similar techniques to enable high throughput device fabrication and realize new technologies particularly in the area of flexible optoelectronics [8-10].

Research on solution-processed semiconductors has focused on both organic and inorganic systems. However, molecular organic systems have several disadvantages including poor environmental, mechanical, and thermal stability as well as poor electronic transport as compared to their inorganic counterparts. On the other hand, inorganic semiconductors can take advantage of covalently bonded frameworks to achieve desirable electronic transport properties and band gaps [11-13]. There have been tremendous efforts to deposit inorganic films with excellent properties using chemical bath deposition, spray pyrolysis, and other solution-based methods [14-17].

Among various inorganic semiconductors, metal chalcogenides, particularly, group V–VI compounds have been widely studied for their optoelectrical and thermoelectric properties and successfully utilized in thin film transistors, solar cells, thermoelectric devices, photodetectors (PDs), and phase change memory applications. These films have typically been prepared via sophisticated deposition techniques such as catalyst-assisted chemical vapor deposition, sputtering, thermal evaporation, and molecular beam epitaxy that require energy-intensive, high vacuum deposition conditions not amenable to high-throughput mass production.

Although most metal chalcogenides are very difficult to dissolve in common solvents, recent developments in solution-based chemistry of chalcogenides have overcome this limitation, and homogeneous, high-quality semiconductor films derived from true molecular inks have been grown successfully [18]. Typically, an ink is made by dissolving stoichiometric amounts of elemental chalcogens with metal in hydrazine solutions [19]. Unfortunately, hydrazine is highly toxic and explosive, which limits the practicality of production. Some less hazardous and volatile solvents, such as mixtures of amine and thiols, have been used for solution deposition, but their application has been limited to bulk metal chalcogenide thin film growth from their respective compounds [20].

Antimony selenide (Sb_2Se_3) has emerged from the group V–VI chalcogenides as an excellent candidate for optoelectronics due to its direct band gap of about 1.1 eV in the NIR regime and p-type semiconductor behavior. 1D Sb_2Se_3 nanostructures are of particular interest due to their high surfaceto-volume ratio and tunable properties that can be used to enhance the performance of optoelectronic devices. Such NWs have been synthesized in the past using solution-based growth methods, but Sb_2Se_3 –based devices, (e.g., PDs) have been fabricated mostly on rigid substrates. The complicated growth methods based on toxic solvents and limited performance to date have hindered Sb_2 Se_3 from competing with traditional crystalline PD technologies.

Here, we report on a method for template-free, facile, onestep solution-based and in-situ growth of Sb_2Se_3 nanowires (NWs) on flexible polyimide substrates for fast response and high-performance flexible PDs. Our one-pot synthesis method is based on a molecular ink prepared by directly mixing elemental antimony and selenium into a solution of ethylenediamine (EDA) and 2-mercaptoethanol (ME). This is the first time, to our knowledge, that this facile synthesis method has been used to fabricate Sb_2Se_3 PDs. Chemical, structural and optical properties of the NWs obtained from this technique are characterized. Sb_2Se_3 PDs fabricated on flexible substrates exhibit excellent figures of merit, such as a broadband photoresponse spanning from the ultraviolet (UV) to near-infrared (NIR) range, fast temporal response, and superior mechanical stability. Previous studies on Sb_2Se_3-based flexible PDs have primarily focused on using polyethylene terephthalate (PET). However, in this study, we substitute PET for polyimide, a film with a higher glass transition temperature (350 vs 78 °C), superior maximum operating temperature (350 vs 160 °C), and chemical exposure while maintaining excellent performance. Additionally, we demonstrate that the spectral response of our detectors should be tunable by adjusting the nanowire size. Our results indicate that molecular-ink-based flexible, scalable, and tunable systems have the potential to replace conventional broadband and NIR optoelectronic technology.

6.2 Morphology and Composition Analysis

Our deposition method for Sb2Se3 films is depicted in Figure 6.1 and involves the following steps: (i) dissolving elemental Sb with excess Se at a molar ratio of 1:3 in EDA and ME to produce the precursor solutions under magnetic stirring for several days in a nitrogen glove box; (ii) spin-casting the resulting dark orange molecular ink onto polyimide substrates, and (iii) annealing the as-deposited films.

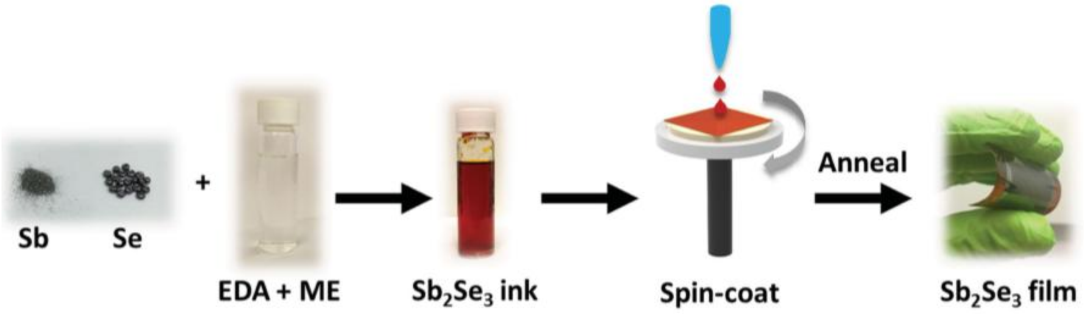

Figure 6.1 Fabrication scheme for Sb_2Se_3 nanostructure formation on flexible substrates utilizing a molecular ink. The process begins with dissolution of elemental Sb and Se in ethylenediamine (EDA) and 2-mercaptoethanol (ME) to produce a molecular ink that is spin-cast onto a flexible substrate and annealed to form a flexible nanowire-based film.

We used field-emission scanning electron microscopy (FESEM) to image the Sb2Se3 nanostructures on flexible polyimides after thermal processing at 350 °C in the presence of excess Se, as shown in Figure 6.2 (a). The FESEM image shows the formation of randomly oriented NWs having a small range of lengths and diameters.

The processing temperature and selenium concentration are key fabrication parameters as they dictate the aspect ratio of the nanostructures, which, in turn, affects the device optical properties. Formation of NWs from the as-deposited films takes place at around 200 °C in the presence of excess selenium; however, when the concentration of Se is lowered (to near the stoichiometric concentration), the films grow instead with a nanograin-like morphology. Compositional mapping by energy-dispersive X-ray spectroscopy (EDXS) shows the distribution of Sb and Se elements in the film, and one can clearly see the individual nanostructures in the elemental maps.

Transmission electron microscopy (TEM) measurements revealed rod-like morphology of 0.1-1.2 µm long Sb_2Se_3 NWs with diameters ranging from 100 to 300 nm (Figure 6.2 (b)). The corresponding selected-area diffraction (SAED) pattern (Figure 6.2 (b) , inset) and phase-contrast high-resolution TEM (HRTEM) images (Figure 6.2 (c)) indicate that the Sb2Se3 nanostructures are single orthorhombic crystals growing along the <001> direction of the Pbnm space group. The SAED pattern of an individual NW indexed as the [430] zone shows a 002 point reflection with 0.20 nm lattice spacing (d002= 0.19810 nm) and a 340 point reflection with 0.23 nm lattice spacing (d340= 0.23431 nm). More detailed analysis of SAED patterns revealed additional splitting of {34 l } reflections due to twinning of NWs along the growth direction likely caused by close-packed growth conditions. The latter was supported by examination of corresponding TEM micrographs. The HRTEM image in Figure 6.2 (c) (left) reveals several families of interplanar lattice fringes, including large 0.58 nm (020) spacing (d 020 = 0.5885 nm) parallel to the growth direction, and the inset shows a Fast Fourier Transform (FFT) pattern implying [100] orientation for the Sb2Se3 NW sample area indicated by the red box. The enlarged HRTEM fragment (Figure 6.2 (c) , right) shows orthogonal 0.19 nm (022) and (0-22) lattice fringes observed in the vicinity of a partially amorphized NW surface.

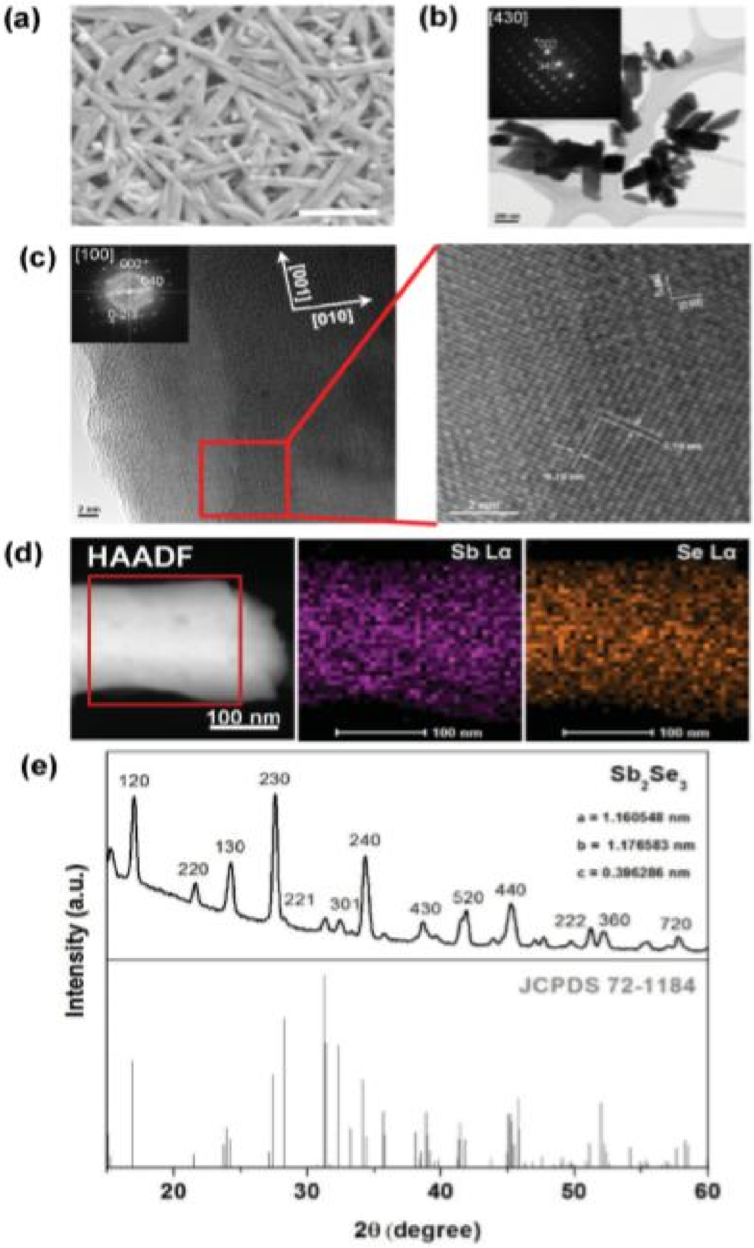

Figure 6.2 Analytical electron microscopy and XRD analysis of Sb2 Se3 NWs: a) High magnification FESEM image. The scale bar corresponds to 1 µm. b) Bright-field (BF) TEM of Sb2Se3 NWs with an SAED pattern in the [430] orientation (inset). c) HRTEM of a single crystalline orthorhombic NW growing along the <001> direction with the corresponding FFT pattern in the [100] orientation (upper left inset). The right inset shows an enlargement of the area marked by the red box on the left showing the (022) and (0-22) lattice fringes. d) HAADF-STEM image of an Sb_2Se_3 NW and corresponding Sb Lαand Se Lα X-ray maps (right insets). e) GIXRD pattern of the Sb2Se3 NW film, the calculated lattice constants (top) and stick pattern JCPDS card, No. 72 ‑ 1184 (bottom).

For more accurate evaluation of the nanoscale elemental composition and the spatial uniformities of the Sb and Se elemental distributions, EDXS-FESEM compositional analyses were corroborated with high spatial resolution EDXS and electron energy-loss spectroscopy (EELS). Analyses of randomly selected NWs from the same sample were performed using a 0.2 nm diameter electron probe in scanning transmission electron microscopy (STEM) mode at 300 kV accelerating voltage. Elemental mapping results revealed that Sb and Se were uniformly distributed throughout the analyzed NWs (Figure 6.2 (d)). X-ray spectra acquired during line profiling have been further quantified using a Cliff-Lorimer thin film ratio technique with calculated k-factors for the Sb $K\alpha$ and the Se $K\alpha$ peaks, and absorption (mass-thickness) correction as described elsewhere. Quantification results demonstrate that the Sb/Se atomic ratio in the NWs is close to stoichiometric with excellent agreement between the employed analytical techniques (Table 1). We further confirmed the crystal structure of the Sb2Se3 NW films using grazing incidence X-Ray diffraction (GIXRD), as shown in Figure 2 e. All of the diffraction peaks can be indexed to the orthorhombic phase of Sb2Se3 (JCPDS Card No. 72 – 1184) with a space group of Pbnm (62). All of the major planes were indexed, and no secondary phases were detected. Using retrieval analysis, the lattice constants are calculated as: a = (1.160584 ± 0.0004) nm, b= (1.176583 ± 0.0005) nm, and c = (0.396286 ± 0.0002) nm, very close to the ideal bulk values for Sb2Se3 (a=1.162 nm, b=1.177nm, c= 0.3962 nm), and consistent with previously reported data.

6.3 Optical Properties

In order to determine the transition type and the optical band gap, a transmission spectrum of the Sb_2Se_3 NW thin films was recorded using UV–vis absorption spectroscopy. The band gap was estimated by extrapolating the linear region of the Tauc plots of (α hν) 2 versus hν to hν = 0 (Figure 6.3 (a)), where α is the absorption coefficient and hν is the photon energy. A direct transition type with a value of ≈1.12eV was confirmed, quite close to previously reported values.

We also computed the electronic band structure of bulk Sb2Se3 using density functional theory and found good agreement with the measured band gap of the deposited NWs. The calculated minimum gap of 0.90 eV for Sb_2Se_3 was found to be indirect, and the direct gap was 1.05 eV, a difference of 0.15 eV from the indirect gap, making the direct and indirect transitions almost degenerate, as previously reported (Figure 6.3 (b)). Furthermore, the band structure of Sb2Se3 exhibits several transitions between the valence band and the conduction band with comparable energy to the fundamental indirect-gap energy, suggesting that Sb2Se3 can be considered a direct gap semiconductor for all practical applications. The states at the valence band edge are predominantly associated with Se p-orbitals and those at the conduction band edge are dominated by the Sb p-orbitals. The density of states (DOS) for bulk Sb_2Se_3 shown in Figure 6.3 (c) agrees well with earlier work. The close agreement in the band gap of bulk Sb2Se3 and solution-deposited Sb2Se3 NWs indicates surface and quantum confinement effects play little role in the electronic structure of the NWs. In addition, Raman spectroscopy performed on Sb2Se3 NWs revealed two Raman peaks centered at (190 ± 0.3) and (253 ± 0.3) cm −1 which represent the hetero-polar Sb−Se and nonpolar Sb−Sb vibrations (Figure 6.3 (d)). The additional minor peaks located at ≈160 and ≈212 cm^{-1} can potentially be attributed to the oxidation of the film or Sb_2O_3 .

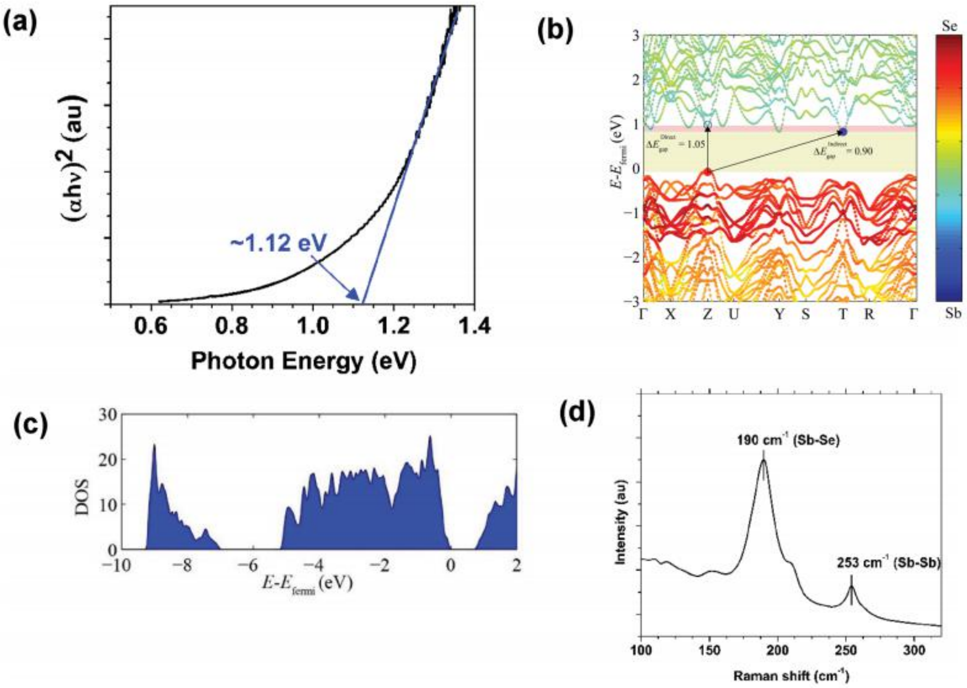

Figure 6.3. Optical properties of Sb_2Se_3 : (a) Tauc plot used to estimate the band gap ($\approx$1.12 eV) from a linear interpolation. (b) Electronic band structure of bulk Sb_2Se_3 computed using DFT simulations. Sb_2Se_3 has an indirect band gap, $\Delta E_{gap}^{Indirect}$ of 0.90 eV and a direct band gap, ΔE_{gap}^{Direct} of 1.05 eV. The valence band maxima and conduction band minima are marked with red and blue circles, respectively. The symbol sizes and colors denote the weights of the Sb or Se contributions to the bands. The valence band maximum is set to zero energy. (c) The calculated DOS versus $E - E_{fermi}$ in eV. (d) Raman spectrum showing the heteropolar Sb−Se and nonpolar Sb−Sb vibrations.

6.4 Performance Evaluation

After establishing the crystal structure and optical properties of the molecular-ink-based Sb_2Se_3 NWs, we fabricated flexible photoconductive PDs by depositing interdigitated Au/Ti/Au electrodes via electron beam evaporation on the NW-polyimide substrates (inset of Figure 4 a). Figure 4 a shows a current–voltage (I–V) characteristic curve for an Sb_2Se_3 NW PD measured in the dark and under 870 nm illumination. At an applied bias ranging from −30 to 30 V with a very low illumination intensity of ≈6.4 μW, the change in slope of the I – V curve indicates a strong photoresponse, and the linear I – V curve evinces the Ohmic nature of the contact between the metal electrodes and NWs.

The temporal response of the PD under pulsed 365 nm illumination (30 mW cm^{-2} , 20 and 90 s pulse widths) and 10V bias is presented in Figure 4 b. Both shorter (20 s pulse width) and longer (90s pulse width) periods of modulation were performed to demonstrate the photocurrent stability. The PD photocurrent is reproducible and stable with two distinct states: a “low” current state in the dark and a “high” current state under illumination with an on/off ratio of ≈22. The characteristic rise time (tr) for the photocurrent to increase from 10% to 90% of its maximum value is (24 ± 2) ms, and the decay time (td) for the photocurrent to decrease from 90% to 10% of the peak value is (9 ± 2) ms (as illustrated in Figure 6.4 (c)). This temporal response is significantly faster than in previous Sb_2Se_3 -based PD demonstrations with both response and recovery times that are two orders of magnitude smaller than previously reported values (24 and 9 ms vs 0.18 and 0.20 s).

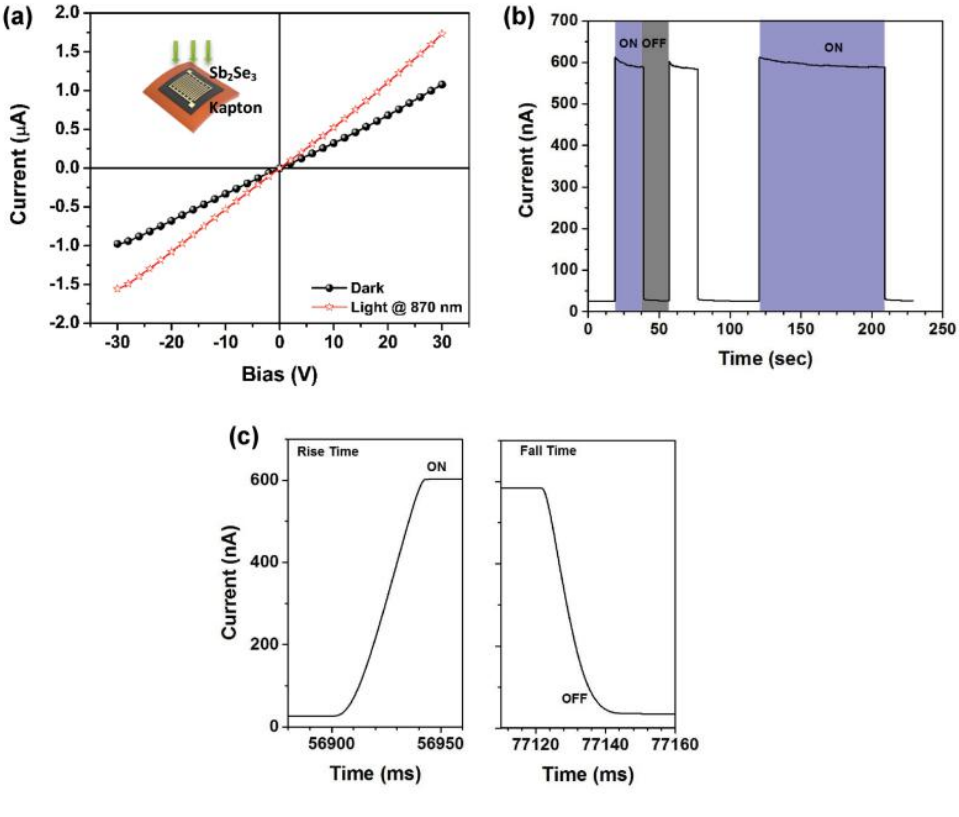

Figure 6.4 Photoconductive device properties: (a) I – V curves measured in the dark and under 870 nm illumination with a light intensity of 6.4 μW. The inset shows a schematic of the fabricated PD with interdigitated electrodes. (b) Temporal photocurrent response under 365 nm pulsed light (≈30 mW cm −2) with periods of 20 and 90 s (to demonstrate stability) at an applied bias of 10 V. (c) Zoomed-in temporal photocurrent response illustrating the rise (24 ± 2 ms) and decay (9 ± 2 ms) times measured in one period of modulation.

Device photoresponse is generally governed by complex processes such as carrier generation, trapping, and recombination. Due to the nanostructured nature of the PD active layer, abundant grain boundaries (or junction barriers) are expected to be present in the NW film. This type of defect is generally associated with the formation of deep traps leading to slow temporal response. Instead, the NW film measured here exhibits fast decay and recovery times. This can potentially be attributed to the high-quality crystalline nature of the materials, which leads to efficient optical absorption and photocarrier generation under illumination. The increased carrier density reduces the junction barrier height between the adjacent NWs, and such light-induced barrier height modulation could lead to the fast response time. Additionally, the large surface-to-volume ratio of the NWs is likely associated with a high density of surface-associated dangling bonds/defects. Thus, when the light is turned off, the carriers can recombine quickly, resulting in short decay times.

We also obtained the spectral response of the PD by scaling the measured photocurrent to that of a calibrated Si PD. Given nominally identical illumination conditions under applied bias, this measurement can be used to extract the external quantum efficiency (EQE) of the device. Figure 6.5 (a) (top) is a contour plot of the device EQE, which increases monotonically with the applied bias. It can be seen that the applied bias influences the on/off ratio of the PDs, which is related to the bias dependence of the exciton dissociation and the background current. The EQE at 30 V reaches a maximum of ≈35% in the NIR (at 1.43 eV) and ≈51% in the UV (at 4.13 eV); however, it remains lower in the visible regime.

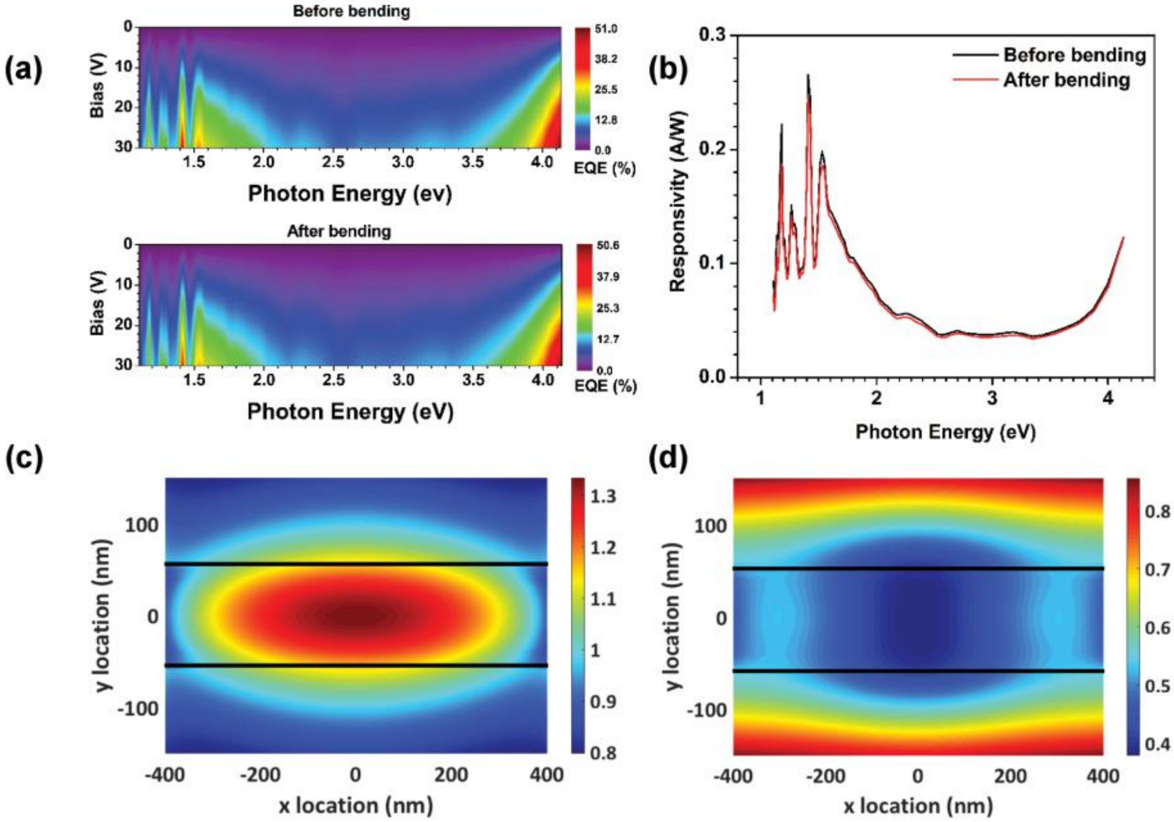

Figure 6.5 Figures of merit of the PDs: (a) EQE data as a function of applied bias: as-made device (before bending: top) and after 40 bending cycles (after bending: bottom) over a radius of curvature of 1 cm. (b) Representative spectral responsivity of the same device at an applied bias of 30 V. The mechanical robustness of the device is evident even after 40 bending cycles. Calculated FDTD normalized electric field intensity for an average-sized single Sb2Se3 nanowire at the plane normal to the incident illumination (s-polarized source) at (c) λ = 1100nm and (d) λ = 650 nm. The presence of a waveguide mode in (c) versus the absence of a confined mode within the NW in (d) demonstrates a possible explanation for the enhanced NIR performance seen in (a) and (b).

In order to investigate the source of the partial visible transparency present in the EQE spectra, we ran a series of finite-difference time-domain (FDTD) optical simulations of single nanowires and nanowire arrays. The nanowires in the arrays were randomly oriented and modeled as cylinders with a uniform distribution of 250 nm in diameter and 900 nm in length, based on the SEM measurements of the as-grown samples. Their refractive indices were determined from ellipsometry measurements, and absorption and reflection spectra as well as spatial electric field data were obtained for nanowire arrays, planar Sb2Se3 control films of comparable total thickness, and single nanowires.

The FDTD single NW absorption results qualitatively reproduce the observed dip in the visible region of the EQE spectra (Figure 6.6 (d)), while the planar device absorption has less of a spectral discrepancy across the same range (Figure 6.6 (a)). The single nanowire results give a potential explanation for this phenomenon: in the visible region, the most common size of nanowire does not support a waveguide mode; however, in the NIR, the nanowire supports a strong mode, leading to enhanced in-coupling and waveguiding in the nanowire array. Nanowire spatial electric field profiles are plotted in Figure 5 (c) and (d) for 1100 and 650 nm illuminations, respectively. The absorption spectra in Figure 6.6 (a) also display resonance peaks in the NIR regime similar to peaks observed in the device EQE and spectral responsivity (Figure 5 (a), (b) respectively). Additionally, Figure 6.6 (e) shows the reflection spectrum of the fabricated Sb_2Se_3 nanowire film without electrodes. The small pitch of the interdigitated electrodes (IDEs; 100 μm) leads to a shadowing effect that results in the loss of a fraction of the incoming light (≈35%). This shadowing could be reduced in future systems by replacing the opaque electrodes with thinner metals or transparent conductive oxides and optimizing their fill fraction.

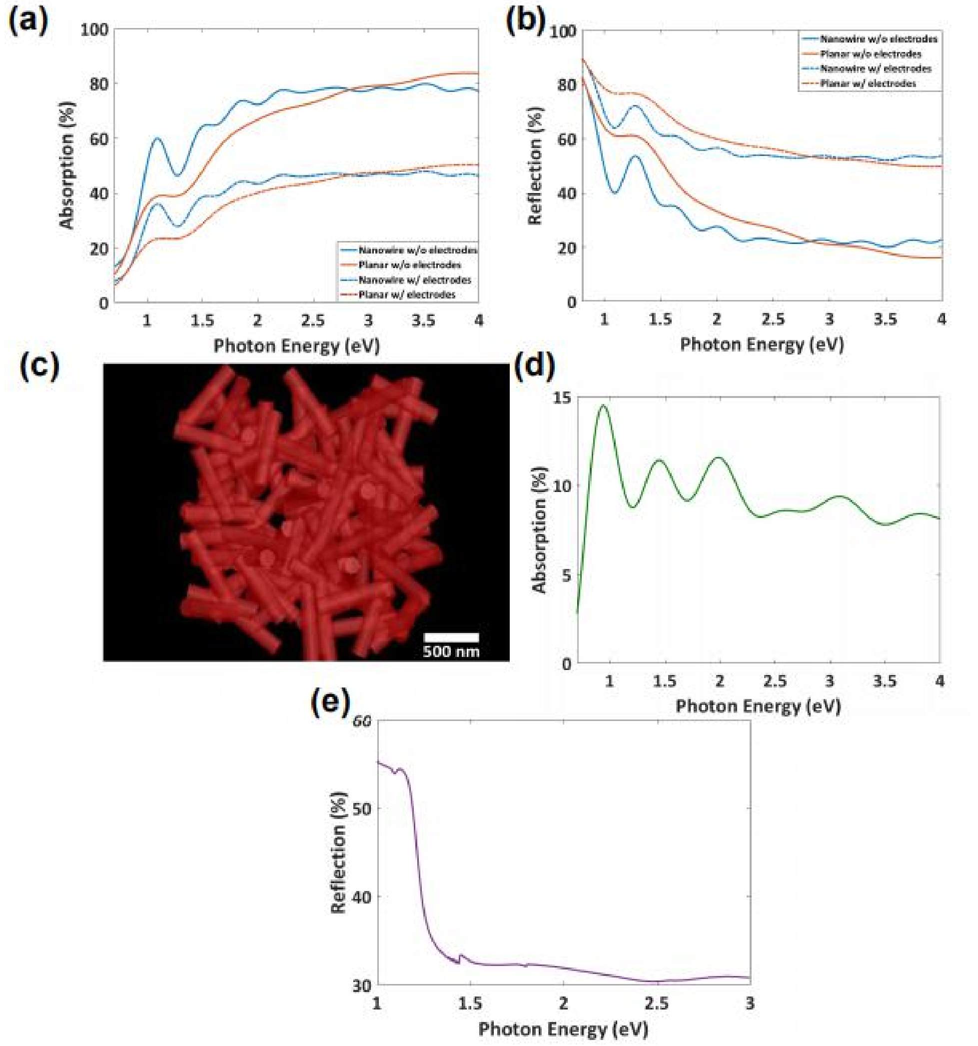

Figure 6.6 (a) FDTD-calculated absorption spectra for both the nanowire and planar devices with and without shading effects due to the interdigitated electrodes. (b) Reflection spectra for both the nanowire and planar devices with and without shading effects due to theinterdigitated electrodes. (c) Top view of the randomly arrayed Sb2Se3 nanowire model used in FDTD simulations. (d) Calculated absorption spectrum for a single Sb2Se3 nanowire. (e) Experimental reflection spectrum for an Sb_2Se_3 nanowire film.

These results imply that the spectral responsivity of the PDs could be tuned by changing the size of the nanowires in the array. The nanowire size is controlled by relative precursor concentration during growth and post-annealing conditions. This tuning knob could be used to enable enhanced broadband performance of the molecular-ink based PDs. Additionally, controlling the nanowire size would allow for the realization of spectrally selective detection by enhancing or suppressing performance in specific spectral bands. Mechanical stability is critical for practical applications of flexible optoelectronics. We measured the device photocurrent after 40 bending cycles over a radius of curvature of ≈10 mm. As shown in Figure 6.7 (a) (bottom), there is no significant change in the EQE after many bending cycles, demonstrating the robustness of these PDs. The responsivity (R_λ) , another critical measure of PD performance, has also been calculated using Equation 6.1.

$$R_\lambda = \frac{I_{light}}{P_0} \tag{6.1}$$

where I_{light} is the device photocurrent under UV illumination, and P_0 is the light intensity. The calculated responsivities of the devices at 30 V bias are shown in Figure 6.7 (b) before and after bending. The maximum responsivity reaches ≈0.27 A W^{-1} at 880 nm and experiences only a slight decrease to ≈0.25 A W^{-1} after 40 bending cycles, comparable with other broadband PD technologies.

The figures of merit for these molecular-ink-based PDs could be further improved by optimizing the processing conditions and tuning the gap between the two IDEs to optimize the metallized area. Optically, tuning the nanowire size could target waveguiding and enhanced performance in the visible regime. One could also employ alternative light trapping and optical enhancement schemes such as integration of nanoscale plasmonic structures to improve in-coupling and benefit from local field enhancements. Exploring these approaches is beyond the scope of this paper.

A facile, scalable, template-free route was developed to grow Sb_2Se_3 nanostructures directly on flexible substrates. Our molecular ink was prepared from elemental antimony and selenium dissolved in amine/thiol solvents and deposited at room temperature, employing a chemical method that should be extendable to other technologies. Compositional analysis and structural characterization of the resulting nanowires depict chemically pure, high-quality single-crystalline nanostructures with near stoichiometric composition. The fabricated PDs exhibit fast response and excellent figures of merit. Manipulating the nanowire size is an additional tuning knob that could be used to enhance the broadband performance and build spectrally selective optoelectronics. The negligible change in photoresponse after multiple bending cycles is evidence of excellent mechanical stability which makes the molecular inks a promising platform for low-cost, flexible and portable broadband photon detection, photoelectronic switches, and other optoelectronic devices.

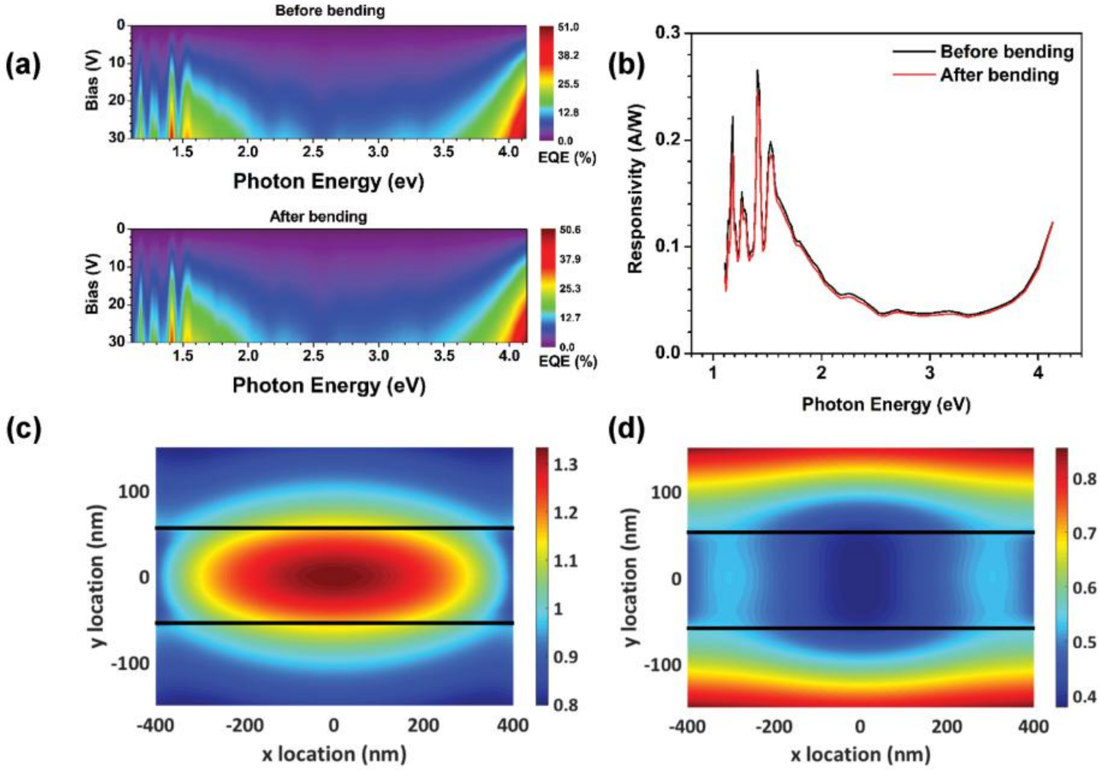

Figure 6.7 Figures of merit of the PDs: (a) EQE data as a function of applied bias: as-made device (before bending: top) and after 40 bending cycles (after bending: bottom) over a radius of curvature of 1 cm. b) Representative spectral responsivity of the same device at an applied bias of 30 V. The mechanical robustness of the device is evident even after 40 bending cycles. Calculated FDTD normalized electric field intensity for an average-sized single Sb_2Se_3 nanowire at the plane normal to the incident illumination (s-polarized source) at (c) $\lambda = 1100$ nm and (d) $\lambda = 650$ nm. The presence of a waveguide mode in (c) versus the absence of a confined mode within the NW in (d) demonstrates a possible explanation for the enhanced NIR performance seen in (a) and (b).

6.5 Conclusion

A facile, scalable, template-free route was developed to grow Sb_2Se_3 nanostructures directly on flexible substrates. Our molecular ink was prepared from elemental antimony and selenium dissolved in amine/thiol solvents and deposited at room temperature, employing a chemical method that should be extendable to other technologies. Compositional analysis and structural characterization of the resulting nanowires depict chemically pure, high-quality single-crystalline nanostructures with near stoichiometric composition. The fabricated PDs exhibit fast response and excellent figures of merit. Manipulating the nanowire size is an additional tuning knob that could be used to enhance the broadband performance and build spectrally selective optoelectronics. The negligible change in photoresponse after multiple bending cycles is evidence of excellent mechanical stability which makes the molecular inks a promising platform for low-cost, flexible and portable broadband photon detection, photoelectronic switches, and other optoelectronic devices.

References

[1] Hasan, Md Rezaul, Ebuka S. Arinze, Arunima K. Singh, Vladimir P. Oleshko, Shiqi Guo, Asha Rani, Yan Cheng et al. "An antimony selenide molecular ink for flexible broadband photodetectors." Advanced electronic materials 2, no. 9 (2016): 1600182.

[2] C. R. Kagan , D. B. Mitzi , C. D. Dimitrakopoulos , "Organic-inorganic hybrid materials as semiconducting channels in thin-film field-effect transistors."Science 1999 , 286 , 945 .

[3] X. Duan , C. Niu , V. Sahi , J. Chen , J. W. Parce , S. Empedocles , J. L. Goldman , "High-performance thin-film transistors using semiconductor nanowires and nanoribbons."Nature 2003 , 425 , 274 .

[4] H. Sirringhaus , T. Kawase , R. H. Friend , T. Shimoda , M. Inbasekaran , W. Wu , E. P. Woo , "High-resolution inkjet printing of all-polymer transistor circuits." Science 2000 , 290 , 2123 .

[5] B. A. Ridley , B. Nivi , J. M. Jacobson ,"All-inorganic field effect transistors fabricated by printing." Science 1999 , 286 , 746 .

[6] D. B. Mitzi , L. L. Kosbar , C. E. Murray , M. Copel , A. Afzali , Mitzi, David B., Laura L. Kosbar, Conal E. Murray, Matthew Copel, and Ali Afzali. "High-mobility ultrathin semiconducting films prepared by spin coating." Nature 428, no. 6980 (2004): 299-303.Nature 2004 , 428 , 299 .

[7] Y. Zhou , M. Leng , Z. Xia , J. Zhong , H. Song , X. Liu , B. Yang , J. Zhang , J. Chen , K. Zhou , J. Han , Y. Cheng , J. Tang , "Solution-processed antimony selenide heterojunction solar cells." Adv. Energy Mater. 2014 , 4 , 1301846 .

[8] H. E. A. Huitema , G. H. Gelinck , J. B. P. H. van der Putten , K. E. Kuijk , C. M. Hart , E. Cantatore , P. T. Herwig , A. J. J. M. van Breemen , D. M. de Leeuw , "Plastic transistors in active-matrix displays." Nature 2001 , 414 , 599 .

[9] G. H. Gelinck , H. E. A. Huitema , E. van Veenendaal , E. Cantatore , L. Schrijnemakers , J. B. P. H. van der Putten , T. C. T. Geuns , M. Beenhakkers , J. B. Giesbers , B.-H. Huisman , E. J. Meijer , E. M. Benito , F. J. Touwslager , A. W. Marsman , B. J. E. van Rens , D. M. de Leeuw , "Flexible active-matrix displays and shift registers based on solution-processed organic transistors." Nat. Mater. 2004 , 3 , 106 .

[10] Y. Sun , G. C. Welch , W. L. Leong , C. J. Takacs , G. C. Bazan , A. J. Heeger , "Solution-processed small-molecule solar cells with 6.7% efficiency." Nat. Mater. 2012 , 11 , 44 .

[11] D. B. Mitzi, "Solution-processed inorganic semiconductors." J. Mater. Chem. 2004 , 14 , 2355 .

[12] J.-S. Lee , M. V. Kovalenko , J. Huang , D. S. Chung , D. V. Talapin , "Band-like transport, high electron mobility and high photoconductivity in all-inorganic nanocrystal arrays." Nat. Nanotechnol. 2011 , 6 , 348 .

[13] A. M. Smith, S. Nie, "Semiconductor nanocrystals: structure, properties, and band gap engineering." Acc. Chem. Res. 2010 , 43 , 190

[14] P. K. Nair , M. T. S. Nair, V. M. Garcı´a, O. L. Arenas , A. C. Peña , I. T. Ayala , O. Gomezdaza , A. Sánchez , J. Campos , H. Hu , R. Suárez , M. E. Rincón , "Semiconductor thin films by chemical bath deposition for solar energy related applications." Sol. Energy Mater. Sol. Cells 1998 , 52 , 313 .

[15] O. Niitsoo , S. K. Sarkar , C. Pejoux , S. Rühle , D. Cahen , G. Hodes , "Chemical bath deposited CdS/CdSe-sensitized porous TiO2 solar cells." J. Photochem. Photobiol., A 2006 , 181 , 306 .

[16] H. Lee , M. Wang , P. Chen , D. R. Gamelin , S. M. Zakeeruddin , M. Grätzel , M. K. Nazeeruddin , "Efficient CdSe quantum dot-sensitized solar cells prepared by an improved successive ionic layer adsorption and reaction process." Nano Lett. 2009 , 9 , 4221 .

[17] H. J. Lee , J. Bang , J. Park , S. Kim , S.-M. Park, "Multilayered semiconductor (CdS/CdSe/ZnS)-sensitized TiO2 mesoporous solar cells: all prepared by successive ionic layer adsorption and reaction processes." Chem. Mater. 2010 , 22 , 5636.

[18] Webber, David H., and Richard L. Brutchey. "Alkahest for V2VI3 chalcogenides: dissolution of nine bulk semiconductors in a diamine-dithiol solvent mixture." Journal of the American Chemical Society 135, no. 42 (2013): 15722-15725.

[19] Todorov, Teodor K., Kathleen B. Reuter, and David B. Mitzi. "High-efficiency solar cell with earth-abundant liquid-processed absorber." Advanced materials 22, no. 20 (2010): E156-E159.

[20] McCarthy, Carrie L., David H. Webber, Emily C. Schueller, and Richard L. Brutchey. "Solution-Phase Conversion of Bulk Metal Oxides to Metal Chalcogenides Using a Simple Thiol–Amine Solvent Mixture." Angewandte Chemie International Edition 54, no. 29 (2015): 8378-8381.

Chapter 7

Conclusion and Outlook

In this dissertation, colloidal aluminum plasmonic nanomaterials have been systematically studied using transient absorption measurements combined with other optical and surface characterizations and finite element analysis. This is the first reported study of the energy relaxation dynamics in solution-processed aluminum nanoparticles. Our work has demonstrated that plasmonic aluminum materials have distinct features when compared to the traditional noble metals gold and silver. Phonon damping in these materials and thermal energy exchange with the surrounding liquid solvent are discussed and modeled, providing fundamental knowledge and expanding our understanding of the underlying physical processes that determine the overall behavior of aluminum nanomaterials. In addition, multicolored and semitransparent solar cells were fabricated based on the development of an efficient optimization algorithm for producing controlled spectral profiles based on multi-layer thin film interference. Finally, a simple and practical synthetic route has been demonstrated for producing high quality Sb_2Se_3 nanowire inks, with important applications in flexible sensing and optoelectronics.

Our work on the electron relaxation dynamics of aluminum-based plasmonic nanostructures provides important information on the feasibility of using aluminum nanomaterials as light sensitizers for plasmonically-enhanced photocatalytic systems. Future directions will be focused on the investigation of hot carrier transfer efficiency from the aluminum sensitizers to photocatalytic titanium dioxide. Spectrally-dependent absorption enhancement in ultrafast transient measurements can be used as an indication of electron transfer. To produce high-performing plasmonic photocatalysts, rational design of the specific architectures of the composite nanostructures to ensure efficient carrier injection is needed. One promising route for fully utilizing the transferred hot carriers is to prepare Al-TiO_2 core-shell structures which requires the development of a new synthetic approach to grow a conformal heterogeneous oxide layer on Al nanoparticle cores.

Our research on multi-colored and semitransparent PbS solar cells can be expanded and applied to other material systems and be utilized in multijunction solar cells for current matching. Improvements in power conversion efficiencies will depend on further deploying new device architectures, electrodes, and quantum dot films with better surface passivation schemes, leading to enhanced efficiencies for practical usage.

Engineering nanomaterials for novel functions is still an important area of active research in the quest for more efficient applications in optoelectronics. Cost is one crucial factor in determining the future direction of this work for the purpose of commercialization and widespread adoption. Critically, reducing the toxicity of optoelectronic nanomaterials to produce “green” technology is equally important in fulfilling the goal of sustainability as we strive to meet the increasing demand for energy and reduce pollutants in our technological infrastructure.

Appendix A

Experimental Details

A.1 Aluminum Nanoparticles Synthesis

All solvents and reagents were purchased from Sigma-Aldrich. Detailed synthetic procedures are described as follows:

1. Inject 6.3ml anhydrous tetrahydrofuran (THF) and 6.3ml anhydrous 1,4-dioxane into the flask connected to an air-free Schlenk line.
2. The mixture solution was stirred and mildly heated up to 40 °C.
3. Inject 3.3 mL precursor solution of dimethylethylaminealane into a flask.
4. Then, 0.4 mL of 3.3 mM titanium (IV) isopropoxide in toluene was injected into the solution, which became light brownish in color instantaneously.
5. 70 µL of oleic acid in 0.25ml dioxane was then injected at different times, ranging from 3 to 30 min to obtain particles of tunable sizes. The reaction was completed after 1-2 hours, and the solution became gray in color.
6. The particles were washed twice using both THF and IPA and finally redispersed in IPA for measurements.

A.2 Acoustic Phonon Simulations

The phonon vibrational modes were calculated using Comsol Multiphysics software. The simulated structure consisted of a single Al/Al2O3 icosahedral NP immersed in IPA. We performed frequency domain analysis for 3D simulations by solving Navier's equation and the Navier−Stokes equation. Continuity conditions for the displacement, stress, and velocity were applied at the particle's boundaries to fully couple the interaction between the particle and the liquid environment. Bulk elastic constants of Al and Al2O3 were used as inputs for mechanical parameters. The soft shell of the oxide layer was modeled by reducing the oxide shell Young's modulus from 269 to 50 GPa. We included the effffect of the oleic-acid surface ligands by adding a thin shell layer on the particle surface with a Young's modulus, Poisson's ratio, and density of 3 GPa, 0.36, and 900 kg/cm^3, respectively. The simulation results are independent of the mesh size to within 0.1%.

A.3 Aluminum/Silver Hybrid Nanoparticles Synthesis

We have synthesized Al/Ag hybrid nanostructures and characterized their optical properties. We chose silver due to its strong LSPR and well-developed solution-processed synthesis methods. Based on our simulation results, alloyed Al/Ag hemispherical NPs are predicted to show an extended resonance wavelength range by tuning the composition ratio (Figure A1(a)).

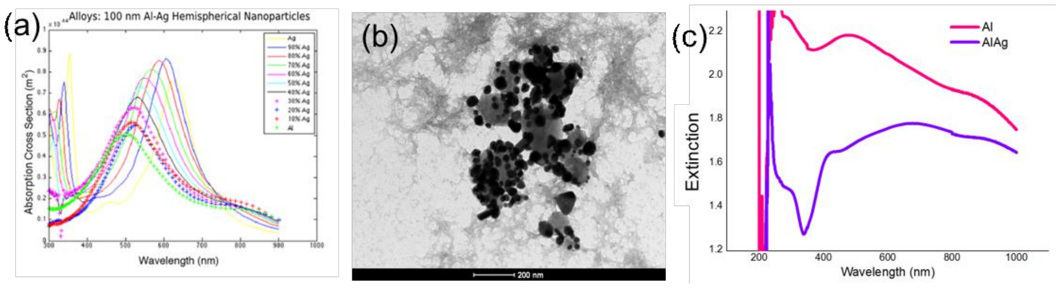

Figure A1 (a) Absorption cross sections calculated for alloyed Al-Ag nanoparticles. TEM images (b) and extinction spectra (c) of hybrid Al/Ag nanoparticles.

In our initial experiments, we attempted to grow hybrid particles by plating silver onto pre-formed Al NPs. Al particles in isopropanol are mixed with silver nitrate (Ag precursor) under mild heating and stirred for 12 hours. The TEM image in Figure A1 (b) shows that instead of forming a conformal layer of Ag on the Al NPs, isolated Ag particles with dimensions of approximately 20 nm are decorated onto the larger Al particle surfaces. The difficulty in forming a continuous Ag layer on the Al is most likely caused by the thin Al native oxide shell which has a large lattice mismatch with Ag, thereby preventing ideal epitaxy conditions. Instead, the Ag nanoparticles appear to nucleate at discrete locations on the Al NPs.

The extinction spectrum of the Ag-decorated Al NPs in Figure A1 (c) shows that the plasmon resonance of bare Al NPs is at 450 nm in wavelength, while the Al/Ag particles show several broad peaks, with the longest at a wavelength of greater than 600 nm.

Future work will include further simulations on the plasmonic properties of the hybrid particles, aiming to systematically study how the Ag concentration (quantity) affects the optical properties of the particles. Based on these results, future work will be focused on tuning our synthesis procedures to gain control over the Ag nucleation and particle concentration and characterizing the composition of the hybrid particles using X-ray photoelectron spectroscopy and energy dispersive X-ray analysis. TAS measurements will be conducted to further analyze the optical properties of the Al/Ag particles and determine how the presence of Ag affects thermal energy transfer in this system. The hybrid Ag-Al particles represent a new plasmonic system with the potential for higher absorption cross-section and finely-tunable properties for applications in photocatalysis and optoelectronics.

A.4 Silicon Conductive Ligands for Enhanced Charge Transport in PbS Quantum Dot Solar Cells

Colloidal quantum dot solar cells are a type of third generation solar cells which is ideal as light absorbing materials. Their bandgaps are tunable by adjusting the size. Capping agents are added for reducing defects which are detrimental for the performance of solar cells. However, charge transport is poor because commonly used ligands are insulating which consisted of carbon atoms, leading to low conductivity in PbS film. There is a compromise between high solar radiation absorption and high conductivity.

We have addressed this issue using conductive silicon-based ligands to replace the original insulting carbon-based ligands. The passivation scheme is shown in Figure A2. Thiol group is designed at one end to bind onto quantum dot surface and whole chain is composed of conductive silicon atoms.

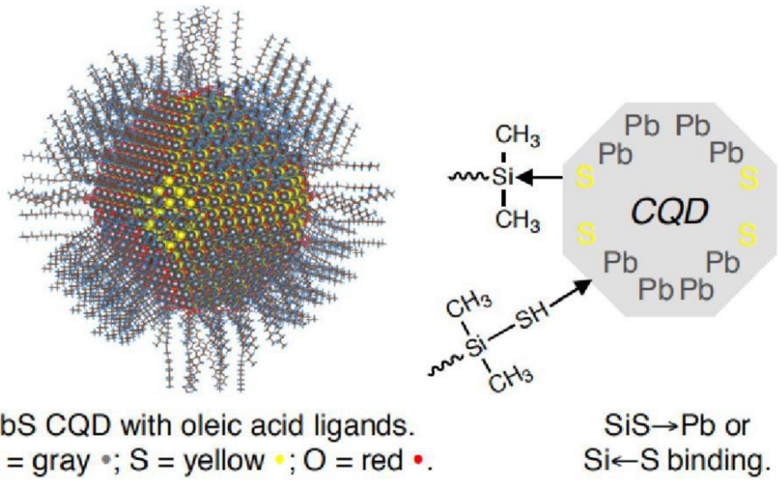

Figure A2 Schematic diagram shows the passivation scheme of PbS quantum dots using silicon ligands.

We used solution-phase ligand exchange process to achieve silicon-based ligands passivation. In Figure A3, quantum dots with oleic acids are originally dispersed in octane and silicon ligand is in DMSO. The exchanges is completed after vortexing for seconds, and the quantum dots are exchanged into DMSO capped with silicon ligands.

Figure A3 Test tubes contains PbS quantum dots before (left) and after (right) silicon ligand exchange.

Top part of the test tube become clear which contains oleic acid in octane. The FTIR spectrum in Figure A4 shows distinct difference of Si-CH_3 and Si-C bands before and after ligand exchange which further confirms successful passivation.

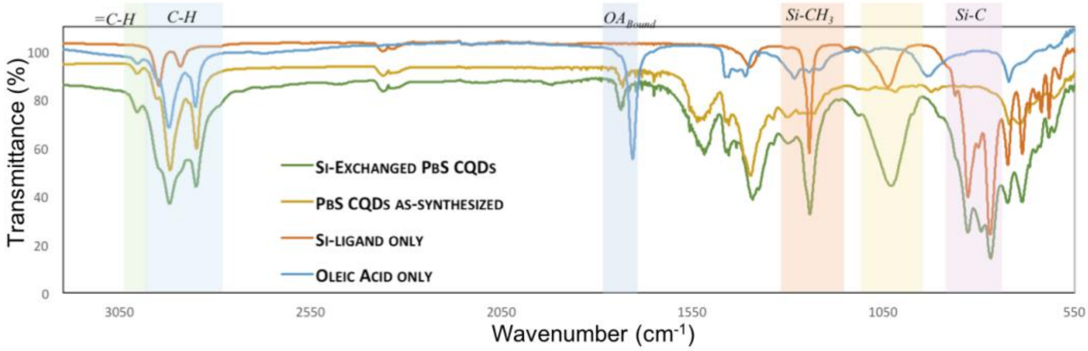

Figure A4 FTIR spectra of PbS quantum dots in solution before and after silicon ligand exchange.

Future work will include fabrication of PbS solar cells using Pbs film with silicon ligands and evaluate the device performance. Ultraviolet photoelectron spectroscopy will be used to study the band structure. Transient absorption measurement will be used to characterize the lifetime of carriers.

Yan Cheng

3400 N Charles St, Baltimore, MD 21218
Phone: 443-600-8955
Email: cyan7@jhu.edu

EDUCATION

Johns Hopkins University Baltimore MD 2020
PhD candidate, Electrical & Computer Engineering

Institute of Semiconductors, Chinese Academy of Sciences Beijng China 2014
MSE, Electronic and Communication Engineering

Nankai University Tianjin, China 2011
B Eng, Electronic Science and Technology

RESEARCH EXPERIENCE

Graduate Research Assistant 2014 - 2020
Department of Electrical and Computer Engineering, Johns Hopkins University

- Synthesis and characterization of colloidal metal nanoparticles and semiconudctor quantum dots with tunable morphologies, composition and optical properties.
- Design and model optical properties of plasmonic nanomaterials usingfinite-difference time-domain method.
- Analyze and perform multiphysics modeling of acoustic phonon oscillations in nano-materials using finite-element method.
- Collaborate across departments to build earth-abundant aluminum-based photocatalyst.
- Fabricate color-tuned and transparent PbS quantum dots solar cells using particle swarm optimization.

Graduate Research Assistant 2014

- Institute of Semiconductors, Chinese Academy of Sciences
- Design and fabricate hybrid tunnel junction (n+-GaN/u-InGaN/p+-GaN) –graphene electrodes for low tunnel resistance in GaN blue LEDs.
- Design and fabricate micro-sized pyramid GaN and graphene electrode for phosphor free white LEDs with two other lab members.
- Fabricate hybrid micro/nano patterned sapphire substrate to improve lightextraction efficiency of GaN-based LEDs.

PUBLICATIONS

[12] **Yan Cheng***, Kenneth J. Smith*, Ebuka S. Arinze, Rachel Dziatko, Tina Gao, Benjamin P. Frank, Susanna M. Thon, and Arthur E. Bragg . "Size and surface-dependent photoresponses of solution-processed aluminum nanoparticles.” (2020). ACS Photonics.

[11] Kenneth J. Smith*, **Yan Cheng***, Ebuka S. Arinze, Nicole E. Kim, Arthur E. Bragg, and Susanna M. Thon. "Dynamics of Energy Transfer in Large Plasmonic Aluminum Nanoparticles." ACS Photonics 5, no. 3 (2017): 805-813.

[10] Zhao, Xingang, Deepa Madan, **Yan Cheng**, Jiawang Zhou, Hui Li, Susanna M. Thon, Arthur E. Bragg, Mallory E. DeCoster, Patrick E. Hopkins, and Howard E. Katz. "High Conductivity and Electron-Transfer Validation in an n-Type Fluoride-Anion-Doped Polymer for Thermoelectrics in Air." Advanced Materials 29, no. 34 (2017): 1606928.

[9] Ebuka S. Arinze, Botong Qiu, Nathan Palmquist, **Yan Cheng**, Yida Lin, Gabrielle Nyirjesy, Gary Qian, and Susanna M. Thon. "Color-tuned and transparent colloidal quantum dot solar cells via optimized multilayer interference." Optics Express 25, no. 4 (2017): A101-A112.

[8] Hasan, Md Rezaul, Ebuka S. Arinze, Arunima K. Singh, Vladimir P. Oleshko, Shiqi Guo, Asha Rani, **Yan Cheng**, Irina Kalish Mona E. Zaghloul, Mulpuri V. Rao, Nhan V. Nguyen, Abhishek

Motayed, Albert V. Davydov, Susanna M. Thon. "An antimony selenide molecular ink for flexible broadband photodetectors." Advanced electronic materials 2, no. 9 (2016): 1600182.

[7] Yan Cheng, Ebuka S. Arinze, Nathan Palmquist, and Susanna M. Thon. "Advancing colloidal quantum dot photovoltaic technology." Nanophotonics 5, no. 1 (2016): 31-54.

[6] Wang, Liancheng*, **Yan Cheng***, Zhiqiang Liu, Xiaoyan Yi, Hongwei Zhu, and Guohong Wang. "Hybrid tunnel junction–graphene transparent conductive electrodes for nitride lateral light emitting diodes." ACS applied materials & interfaces 8, no. 2 (2016): 1176-1183.

[5] Fu, Binglei*, **Yan Cheng***, Zhao Si, Tongbo Wei, Xionghui Zeng, Guodong Yuan, Zhiqiang Liu, Hongxi Lu, Xiaoyan Yi, Jinmin Li and Junxi Wang. "Phosphor-free InGaN micro-pyramid white light emitting diodes with multilayer graphene electrode." RSC Advances 5, no. 122 (2015):100646-100650.

[4] Yan Cheng, Teng Zhan, Jun Ma, Lian Zhang, Zhao Si, Xiaoyan Yi, Guohong Wang, and Jinmin Li. "Improved performance of lateral GaN-based light emitting diodes with novel buried CBL structure in ITO film and reflective electrodes." Materials Science in Semiconductor Processing17 (2014):100-103.

[3] Yiyun Zhang, Haiyang Zheng, Enqing Guo, **Yan Cheng**, Jun Ma, Liancheng Wang, Zhiqiang Liu, Xiaoyan Yi, Guohong Wang, and Jinmin Li. "Effects of light extraction efficiency to the efficiency droop of InGaN-based light-emitting diodes." Journal of Applied Physics 113, no. 1 (2013): 014502.

[2] Wang, Liancheng, Zhiqiang Liu, Haiyang Zheng, Yiyun Zhang, **Yan Cheng**, Haizhong Xie, Liqiang Rao, Tongbo Wei, Hua Yang, Guodong Yuan, Xiaoyan Yi and Guohong Wang. "Mechanisms in thermal stress aided electroless etching of GaN grown on sapphire and approaches to vertical devices." RSC Advances3, no. 27 (2013): 10934-10943.

[1] Yan Cheng, Liancheng Wang, Yiyun Zhang, Haiyang Zheng, Jun Ma, Xiaoyan Yi, Guohong Wang, Jinmin Li. "GaN-Based Light Emitting Diodes with Hybrid Micro-Nano Patterned Sapphire Substrate." ECS Solid State Letters 2, no. 11 (2013): Q93-Q97.

CONFERENCES

[10] Yan Cheng. “Size-Dependent Photoresponse of Plasmonic Aluminum Nanoparticles.” MRS Spring Meeting. 2019. Oral presentation.

[9] Yan Cheng. “Earth-abundant aluminum-based plasmonic nanoparticles for photocatalysis application.” The 53rd Annual Conference on Information Sciences and Systems. 2019. Oral presentation.

[8] Yan Cheng. “Thermal Energy Transfer in Colloidal Plasmonic Aluminum Nanoparticles Aided by Oxidation.” MRS Spring Meeting. 2018. Poster presentation.

[7] Botong Qiu, Ebuka Arinze, Nathan Palmquist, Yan Cheng, Yida Lin, Gabrielle Nyirjesy, Gary Qian, and Susanna Thon. "Optimized Multi-layer Interference for Color-tuned and Transparent Colloidal Quantum Dot Solar Cells." In APS Meeting Abstracts. 2018.

[6] Qiu, Botong, Ebuka S. Arinze, Nathan Palmquist, Yan Cheng, Yida Lin, Gabrielle Nyirjesy, Gary Qian, and Susanna M. Thon. "Optimized multilayer interference for color-tuning in colloidal quantum dot solar cells." In CLEO: Science and Innovations, pp. SM4K-5. Optical Society of America, 2017.

[5] Kenneth Smith, Yan Cheng, Ebuka Arinze, Susanna Thon, and Arthur Bragg. "Ultrafast Photophysics of Plasmonic Aluminum Nanoparticles." In ABSTRACTS OF PAPERS OF THE AMERICAN CHEMICAL SOCIETY, vol. 253. 1155 16TH ST, NW, WASHINGTON, DC 20036 USA: AMER CHEMICAL SOC, 2017.

[4] Yan Cheng. “Earth abundant aluminum nanoparticles for green photocatalysis.” 21st Annual Green Chemistry and Engineering Conference, 2017. Poster presentation.

[3] Ebuka Arinze, Md Rezaul Hasan, Arunima Singh, Vladimir Oleshko, Shiqi Quo, Asha Rani, Irina Kalish, Yan Cheng et al. "Flexible and Broadband Photodetectors via Solution Processed Antimony Selenide." Bulletin of the American Physical Society61 (2016).

[2] Yan Cheng, Kenneth Smith, Ebuka Arinze, Gabrielle Nyirjesy, Arthur Bragg, and Susanna Thon. "Colloidal aluminum nanoparticles with tunable localized surface plasmon resonances for energy applications." In APS Meeting Abstracts. 2016. Oral presentation.

[1] Ebuka S. Arinze, Gabrielle Nyirjesy, Yan Cheng, Nathan Palmquist, and Susanna M. Thon. "Colloidal quantum dot materials for infrared optoelectronics." In Infrared Remote Sensing and Instrumentation XXIII, vol. 9608, p. 960813. International Society for Optics and Photonics, 2015.

TECHNICAL SKILLS

- Electron beam evaporation Chemical vapor deposition Spin coating Nanoparticles Synthesis
- Light microscopy X-ray photoelectron spectroscopy Fourier-transform infrared spectroscopy
- UV-Vis Spectrophotometry Scanning electron microscopy Profilometry
  Transmission electron microscopy Solar cell fabrication and testing
- Finite element analysis Finite-difference time domain

AWARDS

- 2016-2017 Environment, Energy, Sustainability, Health Institute (E^2SHI) Fellow, Johns Hopkins
- Virginia and Edward M. Wysocki, Sr. Memorial Fellowship, Department of Electrical and Computer Engineering, Johns Hopkins University
- Institute Chief Award, Institute of Semiconductors, CAS, China
- Merit Student of Institute of Semiconductors, CAS, China

REVIEW EXPERIENCE

- Applied Nanoscience
- Materials Science in Semiconductor Processing